

ÉCOLE POLYTECHNIQUE FÉDÉRALE DE LAUSANNE

MASTER PROJECT

M.SC. IN COMPUTATIONAL SCIENCE AND ENGINEERING

Isogeometric Analysis of Cardiac Electrophysiology: Application to the Human Atria

Supervisors:

Professor Alfio Quarteroni

Dr. Luca Dedé

Student:

Luca Pegolotti

Sciper N.: 244583

Submitted: January 20, 2017



ÉCOLE POLYTECHNIQUE
FÉDÉRALE DE LAUSANNE

Acknowledgements

I would like to express my gratitude to Professor Alfio Quarteroni, who gave me the possibility to work within the Chair of Modeling and Scientific Computing (CMCS) to my Master Project, and to Luca Dedè, who was very supportive during these months and always available to provide valuable advice and ideas. My thanks go to everyone in the CMCS group, in particular to Andrea and Filippo, with whom I shared the office and most of the moments of my last semester as a student.

I would like to thank my friends in Lausanne, especially Edoardo, Francesco, Giacomo, Nicolo' and Philippe, who helped me during the past two years to make me feel at home even when home was 360 km away, and my friends in Italy, especially Chiara, Dario, Domenico, Francesco, Giovanni, Mauro and Veronica, who make me feel as I had never left.

I would like to thank my family – my parents, my brother and my sister – who have always supported my choices. I dedicate to them this work.

Lastly, I would like to thank Virginia, for always being caring and encouraging.

Contents

1	Introduction	1
2	Mathematical models for Electrophysiology	3
2.1	Principles of heart anatomy and physiology	3
2.1.1	The conduction system of the heart	3
2.1.2	The cardiomyocytes	4
2.1.3	The action potential of cardiac cells	6
2.1.4	Excitation-contraction coupling	7
2.2	The microscopic model	7
2.2.1	The Hodgkin-Huxley model	8
2.2.2	The FitzHug-Nagumo and Roger-McCulloch models	9
2.2.3	The Courtemanche-Rafael-Nattel model	10
2.3	The macroscopic model	12
2.3.1	Derivation of the Bidomain equations	13
2.3.2	Well-posedness of the Bidomain equations	15
2.3.3	The Monodomain model: motivation and equations	17
3	Isogeometric Analysis	19
3.1	B-splines and NURBS	19
3.1.1	Knot vectors and basis functions	19
3.1.2	B-spline geometries	21
3.1.3	NURBS	22
3.1.4	Example: design of a simplified right atrium	23
3.2	Solving PDEs using Isogeometric Analysis	27
3.2.1	Example: the heat equation	27
4	Numerical approximation of the Bidomain equations	33
4.1	Discretization of the Bidomain equations	33
4.1.1	Weak formulation of the problem	33
4.1.2	Space and time discretizations	35
4.2	Numerical simulation on simple domains: some benchmark problems	38
4.2.1	Wavefront propagation on a rectangular slab	38
4.2.2	Dispersion study on a square slab	41
5	Numerical results on the atria	45
5.1	Fibers direction	45
5.2	Electrophysiology on the right atrium	46
5.3	Electrophysiology on both atria	51
5.4	Simulating atrial fibrillation	55
5.4.1	Simulation with modified ionic model	55
5.4.2	Simulation with the burst-pacing protocol	56
6	Conclusions	59
A	The CRN equations	61

Chapter 1

Introduction

The heart is the organ in charge of the distribution of oxygen and nutrients to all the parts of the body, allowing cells to produce energy and, ultimately, to work so that all the basic physiological activities of the body are guaranteed [18]. The study of the mechanisms that regulate the functioning of the heart has always been a crucial area of medical research; this is especially true today, as around 30% of deaths in the world are still due to cardiovascular diseases. Many of these pathological cases are caused by an incorrect contraction of the heart. Hence, in order to explain heart failures, it is important to understand how heart contractions are generated and propagated. During the lifetime of an average human being, the heart beats about 2.5 billion times and pumps in total 200.000 tons of blood into the circulatory system [34]. Each heart beat is characterized by a complex electrical excitation of the cardiac tissue starting from the sinoatrial node and propagating to the other regions of the organ. This process can be accurately described by mathematical equations; their numerical simulation presents difficulties that are due to the complexity of the models, which comes from the intrinsic multi-scale nature of the problem and the characteristic space-time behavior of the solution.

This project focuses on the simulation of the electric processes characterizing the heart by using Isogeometric Analysis for the spatial approximation of PDEs. It is related to [24, 25], where the *Monodomain model* [7, 34] has been applied for generating wavefronts on the left atrium. While in that case the focus had been on the performance of Isogeometric Analysis in terms of accuracy and computational cost, the goal of this thesis is to address realistic simulations involving both atria and complete models for the simulation of the cellular activity and the cardiac tissue. In particular, the *Bidomain model* [5, 6, 7, 8, 15, 32, 35] is used for the description of the macroscopic behavior and we consider its coupling with two ionic models describing the microscopic phenomena: the Roger-McCulloch model [7, 15, 34] and the model by Courtemanche, Ramirez and Nattel [10]. The Roger-McCulloch model is used to study the properties of the Bidomain equations and of Isogeometric Analysis on simple geometries. We focus on the convergence of the velocity of the wavefront with respect to the element size of the mesh and on the dispersion due to the spatial discretization. The more involved model by Courtemanche, Ramirez and Nattel is used to simulate the propagation of the electrical signal in the atria. We first focus on the simulation of the electrocardiology on the right atrium. Then, we perform a simulation involving both atria in which the electrical signal is passed from the right to the left atrium via four connection points. Finally, we discuss an application of the Bidomain model, namely the simulation of atrial fibrillation. This is a type of arrhythmia in which the atrial contraction is disorganized and leads to incorrect pumping of the blood into the ventricles.

The thesis is structured as follows. Chapters 2 and 3 are review chapters. Chapter 2 provides an overview of some concepts of heart physiology, the focus being on cardiac electrophysiology. Then, it describes the mathematical equations modeling the phenomena. Chapter 3 is entirely centered on the Isogeometric Analysis. It provides the reader with the main ideas that form the basis of the method and the theory underlying the design of geometries. We present, as example of geometry generation, the same surface representation of the right atrium that is used in the numerical simulations of Chapter 5. Then, IGA is presented in a non-rigorous fashion by analyzing

a simple case of heat diffusion. In Chapters 4 and 5 simulations using the Bidomain equations are performed. Chapter 4 is about the discretization of the equations presented in Chapter 2 and the solution of test problems on simple geometries. Here, we focus on some aspects of the method itself, such as the convergence of the solution or the numerical dispersion introduced by the discretization. In Chapter 5, the Bidomain equations coupled with the ionic model by Courtemanche, Ramirez and Nattel are solved on surface representations of the atria. We also discuss strategies for simulating the atrial fibrillation by using the Bidomain model. Finally, in Chapter 6 conclusions follow.

Chapter 2

Mathematical models for Electrocardiology

This chapter aims at presenting the mathematical model that will be used in this thesis for the numerical simulation of the electrical activity of the heart – specifically the atria – namely the Bidomain model [5, 6, 7, 8, 15, 32, 35]. Before recalling the derivation and technical details of the equations, we provide the reader with an introduction to the anatomy and physiology of the heart (which is not intended to be exhaustive), with particular attention to the mechanism of action potential formation. We refer primarily to [7, 18, 28] for this part. We will move then to the mathematics of the problem, starting from the equations of the electrical activity at the cellular level (the microscopic model) and then moving to the modeling of the cardiac tissue (the macroscopic model).

2.1 Principles of heart anatomy and physiology

The heart is a double pump whose purpose is to provide the body with oxygenated blood and, at the same time, to remove the waste products of the cellular reactions. It consists of four different spaces, two atria, the left atrium (LA) and the right atrium (RA), and two ventricles, the left and the right ventricle. Atria and ventricles differ in the thickness of the cardiac tissue, which is about three times thicker in the case of ventricles. The atrioventricular septum separates atria from ventricles and let blood flow from the former to the latter through the tricuspid valve in the right part and through the mitral valve in the left part of the heart. Non-oxygenated blood enters the RA through the superior and inferior venae cavae and gets pumped first into the right ventricle, then through the pulmonary valve and into the pulmonary circulation, where it is oxygenated by the lungs. The pulmonary veins let the flow coming from the lungs enter the left part of the heart, from which the blood is pumped again into the aorta and to the systemic circulation of the body. We refer the reader to Fig. 2.1 (left) for a schematic representation of the heart.

2.1.1 The conduction system of the heart

The function of the heart is to pump blood into the circulatory system of the body; this is achieved with the synchronized contraction of atria and ventricles. In the cardiac tissue, the contraction is triggered by an electrical stimulus that originates in the sinoatrial node (SAN), located on the RA close to the superior vena cava. The SAN is often called the *natural pacemaker* of the heart, because its cells are able to excite themselves autonomously. The frequency of the stimulation is influenced by the parasympathetic nervous system and hormonal factors, and in normal health and stress conditions the rate is around 60-80 beats per minute. The signal is then transmitted to the surrounding cells of the RA and reaches the other chambers of the heart thanks to the cardiac conduction system. As explained in [30], it is believed that the interatrial conduction happen at the level of the Bachmann's bundle (primary connection), the anterior septum, the posterior septum and the coronary sinus musculature. These are muscular bundles that electrically connect the two atria; their approximate location is shown in Fig. 2.1 (right). When the excitation front reaches

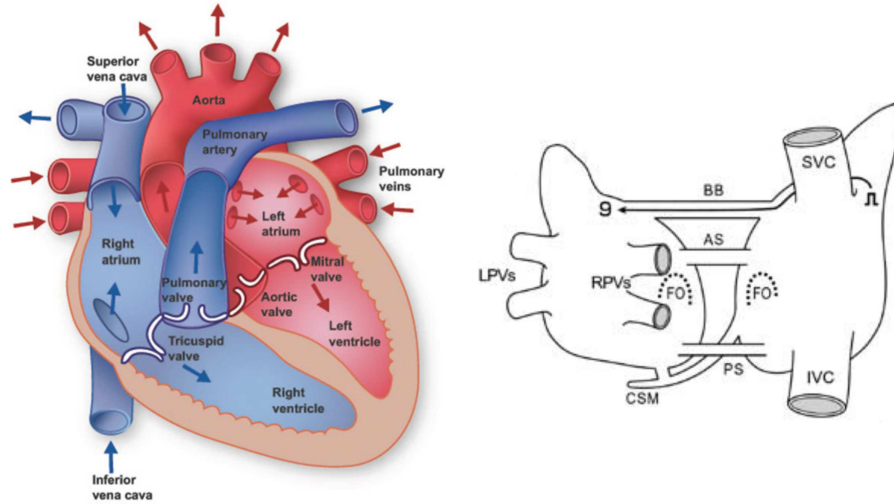


Figure 2.1: Scheme of the heart taken from [7] (on the left). Schematic representation of the interatrial connections taken from [30] (on the right). The electrical stimulus can travel from the RA to the LA via four connections: Bachmann’s bundle (BB), anterior septum (AS), posterior septum (PS) and coronary sinus musculature (CSM). It is shown that, when the electrical stimulus starts from the sinoatrial node – approximately located in correspondence the superior vena cava (SVC) – the principal electrical connection is represented by the BB. The schematic representation on the right shows also the position of the SVC, the inferior vena cava (IVC), the fossa ovalis (FO), the left pulmonary veins (LPVs) and the right pulmonary veins (RPVs).

the atrioventricular node (AVN), at the base of the RA in correspondence of the intersection of the interatrial septum and the interventricular septum, the signal is delayed by the slow conduction velocity characterizing the cells located in this area, to allow the correct synchronization of the contraction between the upper and lower part of the organ. The excitation is then propagated through the bundle of His and the Purkinje network, that spread in a tree-like fashion and innervate the myocardium of the ventricles. The left ventricle (the largest chamber of the heart) is stimulated at the interventricular septum and starts contracting shortly in advance of the right one.

2.1.2 The cardiomyocytes

At the cellular level the heart is composed primarily by cardiomyocytes, i.e. tubular muscular cells with a length of $50 \div 150 \mu\text{m}$ and a diameter of $10 \div 20 \mu\text{m}$; these dimensions vary according to many factors, such as the location of the tissue, development stage and possibly diseases. The sarcolemma is a lipid membrane that encloses cardiomyocytes and separates the external and the internal region; the latter contains liquid (sarcoplasm), organelles (like nuclei and mitochondria), myofibrils, sarcomeres and the sarcoplasmic reticulum.

The outer region and the sarcoplasm contain a variety of ions; the flow of these ions through the sarcolemma happens via some channels, called ionic channels, where only the transit of specific particles is permitted. The sarcolemma presents also invaginations called transverse tubules (T-tubules), which are open to the external region and allow the passage of ions deep inside the internal space. As we will see in the next section, such charged particles make the electric excitation of the cell possible.

The structure of cardiac cells is shown in Fig. 2.2. Cardiomyocytes are composed by bundles of myofibrils containing myofilaments. The basic contractile unit of the muscle cell is the sarcomere, which is enclosed by z-discs, and its length varies between $1.6 \mu\text{m}$ and $2.2 \mu\text{m}$ in human cardiac cells. The sarcomere is formed by thick filaments, composed mainly by myosin, and thin filaments, composed mainly by actin. Moreover, thin filaments contain regulatory proteins called troponin-T, troponin-I, and troponin-C; the latter serves as binding site for the Ca^{2+} during excitation-contraction coupling (discussed in Section 2.1.4). The volume of thin and thick filaments represents about half of the total cell volume.

Cardiomyocytes are electrically connected in units (cardiac syncytia) where the stimulus to

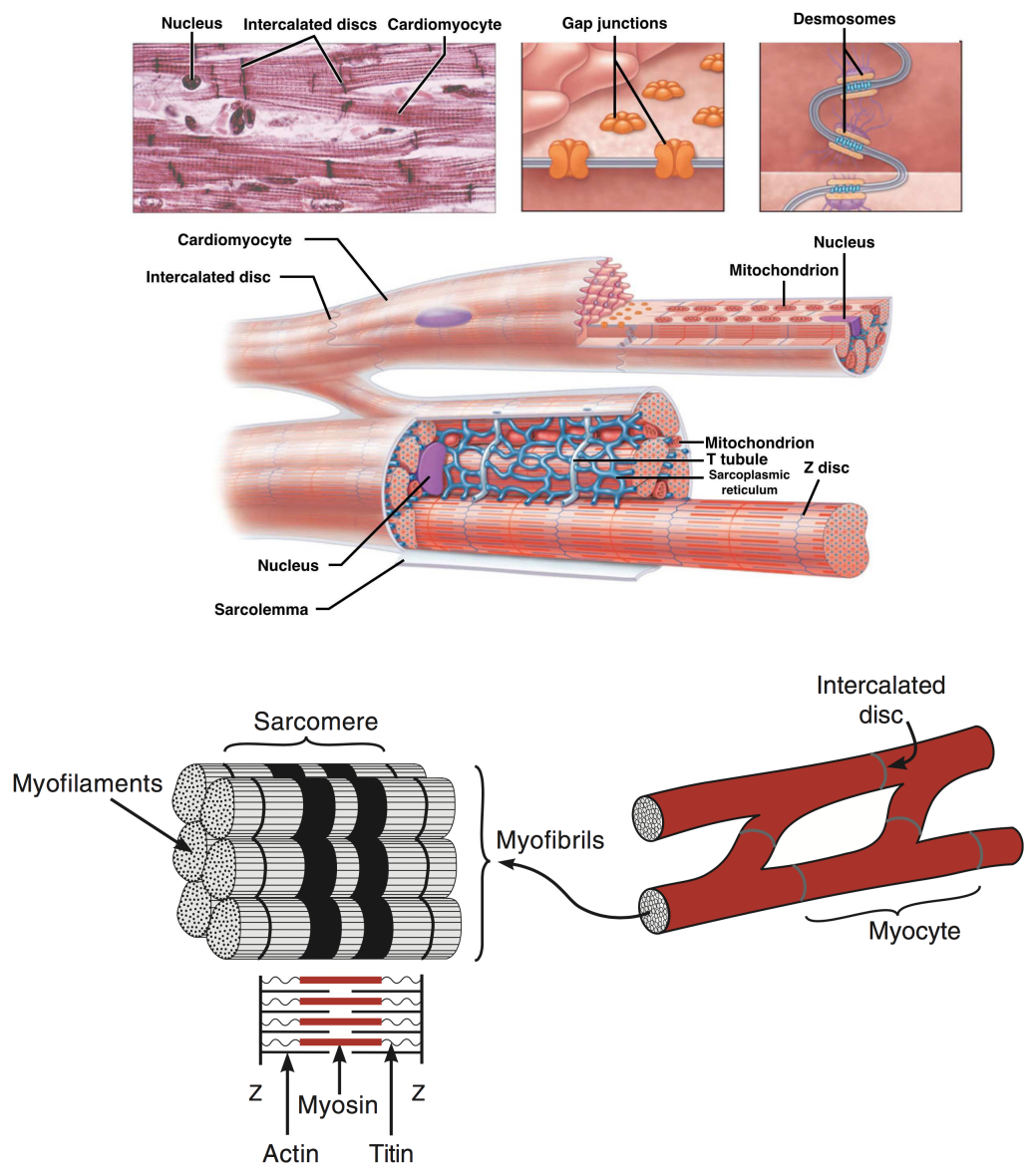


Figure 2.2: Cardiac cell structure (bottom figure: copyright of [18]).

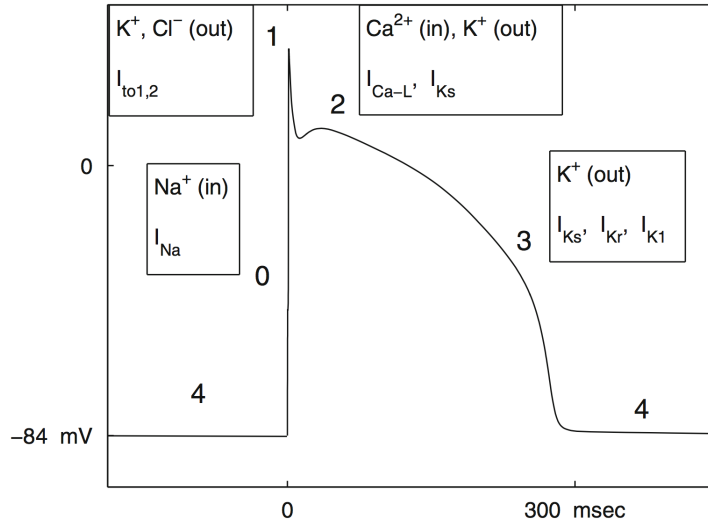


Figure 2.3: Evolution of the transmembrane potential vs time during the AP (taken from [7]). The numbers 0 – 4 correspond to the five phases of the AP.

contract is received and transmitted to adjacent cells. In particular, cardiomyocytes are organized in fibers and linked each other through intercalated discs, structures which include desmosomes and the so called gap junctions. Desmosomes are protein complexes physically joining cells together. Gap junctions are channels of the diameter of about 2 nm and a length of $2 \div 12$ nm that allow the transit of ions to adjacent cells. Gap junctions are mostly located along the longitudinal direction of the fiber, but some of them also transversally. The different densities of gap junctions in the longitudinal and transversal directions make the propagation of the electric stimulation anisotropic.

This peculiar organization of cardiac muscular cells differentiates them from normal myocytes of skeletal or smooth muscle. While in the heart the electric signal is passed to adjacent cells, the other types of muscular cells are singularly innervated, so that the electrical stimulation is directly regulated by the nervous system. This also implies that, while typically the strength of a contraction in a non-cardiac muscle can be varied by increasing or decreasing the number of activated cells, this is not possible in the cardiac tissue.

2.1.3 The action potential of cardiac cells

With action potential (AP) we denote the sudden change of transmembrane potential – defined as the difference between the internal and the external electrical potentials – occurring during the electrical stimulation of cardiomyocytes. Following [7], we identify five phases of the AP (see Fig. 2.3).

During phase 0 (depolarization), Na^+ ionic channels of the sarcolemma open, allowing a free flow of positive ions into the cell. Consequently, the transmembrane potential passes from a negative resting value of -84 mV to positive values. We denote with phase 1 the rapid decrease of potential due to an outward flow of K^+ and Cl^- ions, occurring after the inactivation of the Na^+ channels. Phase 2 is characterized by both an inward current – caused by the transit of Ca^{2+} – and an outward current – caused by the transit of K^+ . This balance maintains the potential almost constant; usually, we refer to this phase with the term “plateau”. The repolarization of the cell – phase 3 – is a consequence of the closing of the Ca^{2+} channels. At this stage, the outward current is still due to the flow of K^+ that causes the potential to return to negative values of $-80/ - 85$ mV. During phase 4 the potential is kept at a constant value of -84 mV. Some of the K^+ ionic channels remain open, in order to guarantee the correct concentrations of ions outside and inside the cell. The cardiomyocyte stays in the resting phase until the next electric stimulation.

Even though the general shape of the AP function does not vary significantly in different tissue regions, we notice that some features, such as total duration, duration of the singular phases and steepness of the depolarization and repolarization are characteristic for each part of the organ.

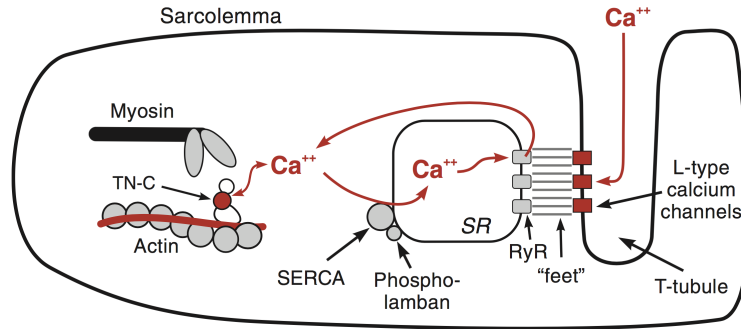


Figure 2.4: Action of Ca^{2+} in the contraction process (image taken from [18]). The calcium ions enter the cell through the L-type channels located on the sarcolemma and on the T-tubules and trigger the ryanodine receptor (RyR) in the sarcoplasmic reticulum to release other Ca^{2+} . The cytoplasmic calcium binds to the troponin-C and causes the sliding of actin and myosin fibers (cell contraction). At the end of the AP, some calcium ions are stored again in the sarcoplasmic reticulum by the sarcoendoplasmic reticulum calcium ATPase (SERCA) and others are expelled via the calcium pumps.

2.1.4 Excitation-contraction coupling

The intracellular calcium concentration is important for various reasons; most notably, it regulates the contractions of the cardiac tissue and influences the pacemaking at the level of the sinoatrial node [5]. We will therefore treat with particular care the evolution of the intracellular calcium concentration in the numerical simulations in Chapter 5. The intracellular calcium concentration increases during the first phases of the AP because of the flux of ions coming from the extracellular space via the specialized long lasting (L-type) channels and because of the subsequent release – *calcium-induced calcium release* – of calcium from the terminal cisternae in the sarcoplasmic reticulum. We remark that the increase in the intracellular calcium concentration is mostly due to the release of ions from the sarcoplasmic reticulum; therefore, the in-flux of Ca^{2+} is sometimes called *trigger calcium* [18]. The contraction of cardiomyocytes, which is called *crossbridge mechanism*, is initiated by this change of the intracellular calcium concentration, see [28]. When such concentration increases, Ca^{2+} ions bind to troponin-C in the thin filaments, which leads to the detachment of the troponin regulatory complex to the binding site in actin and to the binding of the head of myosin to actin. Consequently, thin and thick filaments of the sarcomeres start sliding past each other, the individual sarcomeres shorten, and the whole cell contracts.

As long as the cytosolic calcium concentration remains high enough, the contraction of the cell continues. The Ca^{2+} intracellular concentration starts decreasing towards the last stages of the action potential because of the ions leak through the calcium pump and the Na-Ca exchanger and binding to cytosolic proteins (Ca^{2+} buffers) inside the sarcolemma. In this phase, some of the free ions are also trapped by the so called *sarcoendoplasmic reticulum calcium ATPase* (SERCA), which is an ATP-dependent calcium pump. At this point, calcium starts to dissociate from the binding sites and the troponin complexes bind again to the actin fibers. The sarcomere returns then to the initial length and the cell relaxes.

2.2 The microscopic model

We start the mathematical modeling of the electrocardiology by introducing some of the most commonly used models for simulating the individual ionic currents. As discussed in [34], these models may be divided into three categories: phenomenological models, first generation models, and second generation models. Phenomenological models describe the AP from the perspective of an external observer, without accounting for the underlying physiology. On the contrary, first and second generation models attempt to include a description of the mechanisms of the cell; while the former are based on simplified formulations to approximate the electrical behavior, the latter use instead sophisticated techniques allowing to represent sub-cellular processes.

In the following, we will only focus on phenomenological and second generations models. We take as examples of the first class the FitzHug-Nagumo and the Roger-McCulloch models [7, 15, 34] and, as example of the second class, a complex model proposed by Courtemanche, Rafael and Nattel [10].

2.2.1 The Hodgkin-Huxley model

The Hodgkin-Huxley model [7, 16] was first proposed in 1953 by Alan Lloyd Hodgkin and Andrew Fielding Huxley – who received a Nobel Prize in Physiology ten years later for their work – to simulate the propagation of action potentials in neurons of giant squids. Therefore, this model is not immediately applicable to the simulation of cardiac electrical activity, but it is a good introductory example to the modeling of action potentials.

As discussed in the previous section, the action potential characterizing the electrical activity of cells is caused by the flow of ions through some specific channels. By modeling the sarcolemma as a simple electrical system composed by a capacitor of capacitance C_m in parallel with a resistance, we have

$$C_m \frac{dv}{dt} + I_{ion}(v, \mathbf{w}) = I_{app}, \quad (2.1)$$

where $v = u_i - u_e$ is the transmembrane potential (u_i and u_e being the electric potential inside and outside the cell respectively), \mathbf{w} is a vector of variables modeling the behavior of the ionic channels, I_{ion} is the current that passes through the resistance, and I_{app} is some applied current. This relation is motivated by empirical measurements carried out by Hodgkin and Huxley and it is the simplest one able to model the behavior of the membrane [16]. Eq. (2.1) alone cannot be used to describe the electrical action of the membrane, because it still depends on the unknown ionic current I_{ion} . To complete model (2.1), we need to take into account the ionic channels. For simplicity, we start by considering the case of only one ionic species. Let us introduce $\phi(v)$, namely the current-voltage relation of an open channel, and $g(v, t)$, the proportion of open channels per unit area; we assume these quantities to depend on the transmembrane potential. The function $\phi(v)$ can be modeled by considering the limit case of an infinite tubular cell; see e.g [7]. If we denote with g_c the channel conductance and with v_r some reference potential (resting potential), the current-voltage relation can be expressed with sufficient accuracy as

$$\phi(v) = g_c(v - v_r).$$

The proportion of open channels per unit area can be conveniently rewritten as

$$g(v, t) = \frac{N(v, t)}{N_{tot}} \frac{N_{tot}}{S} = w(v, t) \frac{N_{tot}}{S},$$

where S is the surface of the membrane, N_{tot} is the total number of channels, and N is the number of open channels. The ratio $w = N/N_{tot} \in [0, 1]$ is commonly referred to as *gating variable*. In the following, for simplicity we omit the explicit dependence of w on v and t . By denoting with $\bar{G}_c = N_{tot}g_c/S$ the maximal channel conductance per unit area, we finally write

$$g(v, t)\phi(v) = w\bar{G}_c(v - v_r) = I_{ion}(v, w). \quad (2.2)$$

We notice that the first equality in Eq. (2.2) is valid only under the assumption of long tubular cells.

In order to go further, let us consider in addition to w the percentage of closed channels at time t , say $s(t)$ (simply s in the following). We assume that the transitions from s to w and from w to s happen with rates α and β respectively. In general, α and β may depend on the transmembrane potential. We have then:

$$\begin{cases} \frac{dw}{dt} = \alpha s - \beta w, \\ s + w = 1. \end{cases}$$

Hence,

$$\frac{dw}{dt} = \alpha(1 - w) - \beta w = \frac{w_\infty - w}{\tau_w},$$

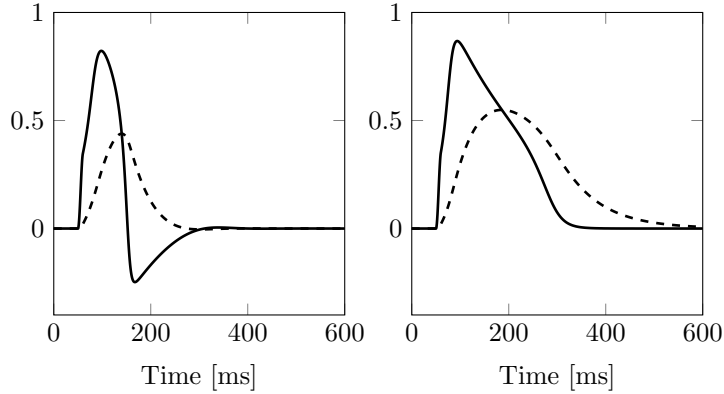


Figure 2.5: Transmembrane potential v (solid line) and recovery variable w (dashed line) computed using the FHN model (left) and the Roger-McCulloch model (right). The external current $I_{app}(t) = \sin((t-t_1)/(t_2-t_1))$ has been applied from $t_1 = 50$ ms to $t_2 = 60$ ms. The values of the coefficients, which were chosen following [34], are: $a = 0.13$, $b = 0.013$, $c_1 = 0.26$, $c_2 = 0.1$ and $c_3 = 1.0$.

where we have introduced the equilibrium potential $w_\infty = \alpha/(\alpha + \beta)$ – we observe that when $w = w_\infty$ the time derivative is zero – and the time constant $\tau_w = 1/(\alpha + \beta)$. By generalizing these equations to the case of three ionic species, we finally get the *Hodgkin-Huxley system*:

$$\begin{cases} C_m \frac{dv}{dt} + I_{ion}(v, m, n, h) = I_{app}, \\ \frac{dm}{dt} = \frac{m_\infty - m}{\tau_m}, \\ \frac{dn}{dt} = \frac{n_\infty - n}{\tau_n}, \\ \frac{dh}{dt} = \frac{h_\infty - h}{\tau_h}. \end{cases}$$

A further generalization of the expression of ionic current can be obtained by considering the general case of N ionic channels and by introducing the concentrations of the species involved:

$$I_{ion}(v, \mathbf{w}, \mathbf{c}) = \sum_{k=1}^N G_k(v, \mathbf{c}) \prod_{j=1}^M w_j^{p_{jk}} (v - v_k(\mathbf{c})) + I_n(v, \mathbf{w}, \mathbf{c}),$$

where $\mathbf{w} = [w_1, w_2, \dots, w_N]^T$ is the vector of gating variables, $\mathbf{c} = [c_1, c_2, \dots, c_N]^T$ is the vector of ionic concentrations, G_k and v_k are conductance and reversal potential for the k^{th} species, p_{jk} are integers and I_n is an additional current modeling time independent ionic fluxes.

2.2.2 The FitzHug-Nagumo and Roger-McCulloch models

To introduce the phenomenological models, we consider the general form of a reduced ionic model [7]:

$$\begin{cases} \frac{dv}{dt} = f(v, w), \\ \frac{dw}{dt} = g(v, w). \end{cases}$$

Different definitions of $f(\cdot, \cdot)$ and $g(\cdot, \cdot)$ give rise to models with different properties. For example, the FitzHug-Nagumo model (FHN) [7, 15, 34] uses the following evolution laws for the potential and the recovery variable:

$$\begin{aligned} f(v, w) &= c_1 v(v - a)(v - 1) - c_2 w, \\ g(v, w) &= v(v - c_3 w). \end{aligned}$$

Fig. 2.5 (left) shows the evolution in time of the transmembrane potential and the recovery variable. We remark that the values are not physical, because during the action potential the potential goes from values of about -85 mV to about 30 mV. Hence, it is necessary to scale v so that it fits the proper range of values.

Even though the evolution of the membrane is similar to a real AP – if we consider that we are only taking into account a simple model with one recovery variable – the main problem of the FHN is that the repolarization of the cell overshoots the initial threshold of 0 V (-84 mV, if v is rescaled), and then settle to the correct resting value.

The Roger-McCulloch model [7, 15, 34], which uses the relations:

$$\begin{aligned} f(v, w) &= c_1 v(v - a)(v - 1) - c_2 v w, \\ g(v, w) &= v(v - c_3 w), \end{aligned}$$

is a (slight) modification of the FHN model that manages to overcome the above mentioned issue. Fig. 2.5 (right) shows that, under the same electrical stimulation, the potential remains indeed positive and the shape of the AP is more realistic. However, it appears that some of the features of the AP depicted in Fig. 2.3 (such as the sharp peak or the long plateau) are still not captured.

2.2.3 The Courtemanche-Rafael-Nattel model

In order to achieve a better approximation of the AP we need to increase the number of variables of the ionic model by introducing quantities representing the transit of different species throughout the membrane and the associated currents. The literature on this topic is vast. Commonly used models for the simulation of ventricular APs are the two Luo-Rudy models [20, 21] and the Bueno-Orovio-Cherry-Fenton model [4]. In this thesis we focus on the mathematical description proposed by Courtemanche, Rafael and Nattel [10] in 1998. This choice is driven by the fact that the Courtemanche-Rafael-Nattel model – which we will call CRN model in the following – is specifically built to recreate the electrical activity of human atrial cells, and will be therefore used in Chapter 5 for the numerical simulation on the atria. The accurate description of the cellular electrical behavior comes at the cost of an increase of the complexity of the equations and the number of variables involved, which consist of transmembrane potential, concentrations of 5 ionic species, and 15 recovery variables. Simitev and Biktashev [33] attempted to reduce the number of variables via an asymptotic approach and managed to obtain a model with only 3 variables, taking into account uniquely the sodium current.

The overall ionic current in the CRN model is given by the composition of 12 currents modeling different phenomena. We have

$$I_{ion} = I_{Na} + I_{K1} + I_{to} + I_{Kur} + I_{Kr} + I_{Ks} + I_{Ca,L} + I_{p,Ca} + I_{NaK} + I_{NaCa} + I_{b,Na} + I_{b,Ca},$$

where: I_{Na} is the fast depolarizing Na^+ current, I_{K1} is the time independent K^+ current, I_{to} is the transient outward K^+ current, I_{Kur} is the ultrarapid delayed rectifier K^+ current, I_{Kr} is the rapid delayed outward rectifier K^+ current, I_{Ks} is the slow delayed outward rectifier K^+ current, $I_{Ca,L}$ is the L-Type Ca^{2+} current, $I_{p,Ca}$ is the Ca^{2+} pump current, I_{NaK} is the Na^+ - K^+ pump current, I_{NaCa} is the Na^+ - Ca^{2+} exchanger current, and $I_{b,Na}$ and $I_{b,Ca}$ are background currents. We refer the interested reader to Appendix A for the equations of the original paper [10], a detailed description of each of the variables and currents involved and the values of the parameters.

Fig. 2.6 shows the evolution in time of the model subject to an external current of 1 ms in terms of transmembrane potential v and the 5 concentrations taken into account by the model, namely $[Na^+]_i, [K^+]_i, [Ca^{2+}]_i, [Ca^{2+}]_{rel}$ and $[Ca^{2+}]_{up}$, where the subscripts *i*, *up* and *rel* refer respectively to the intracellular space, release compartment and uptake compartment. $[Ca^{2+}]_{rel}$ and $[Ca^{2+}]_{up}$ model the variation of calcium concentrations in the sarcoplasmic reticulum. It is evident that the approximation of the AP is extremely accurate: the model manages to capture all the 5 phases of the AP – see Fig. 2.3 – with detail. In particular, the sharp peak and the plateau are more realistic if compared to the results of the FHN and Roger-McCulloch models shown in Fig. 2.5. Along with the information concerning v , the model provides the evolution of the ionic concentrations of some of the most important species to the activity of the myocytes. As explained in Section 2.1.4, the intracellular Ca^{2+} concentration is strictly related to the mechanical reaction of the tissue to the electrical stimulation.

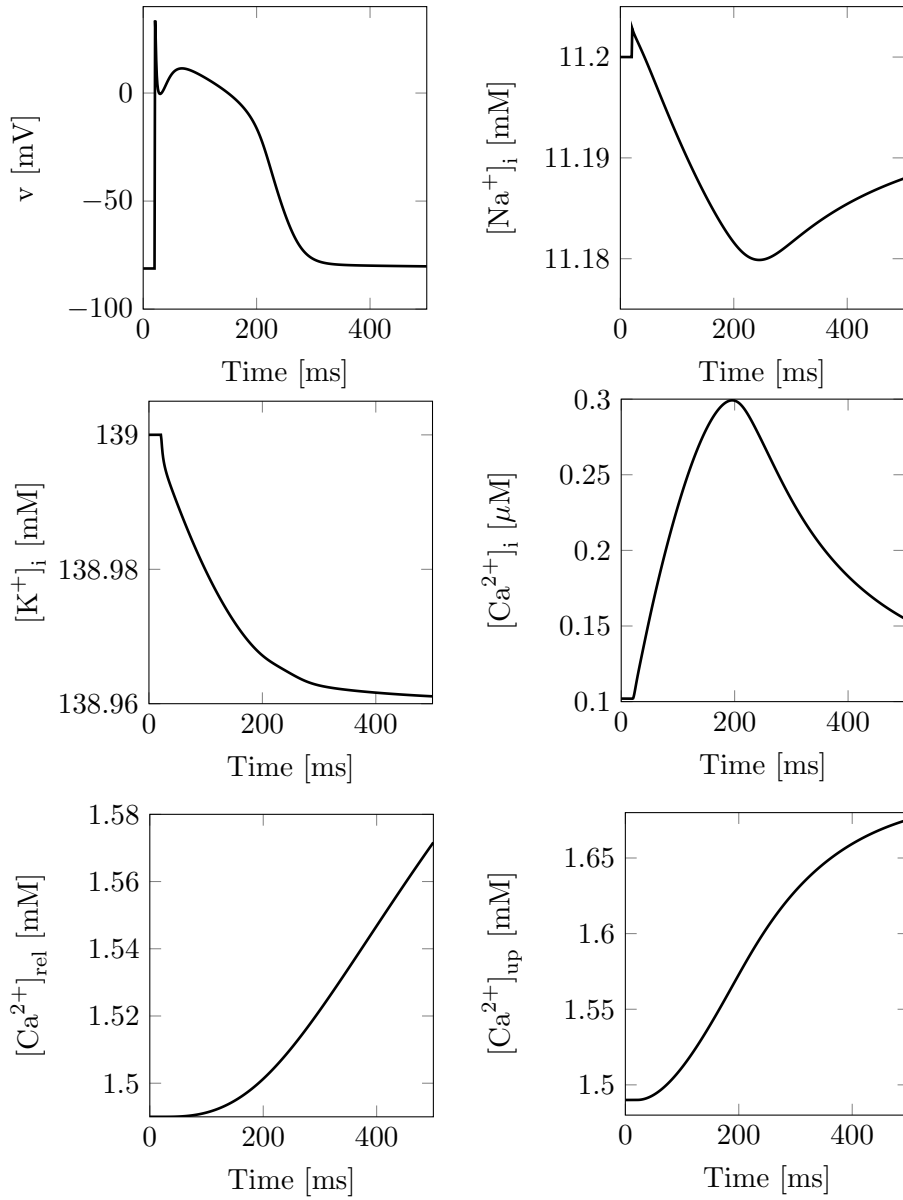


Figure 2.6: Transmembrane potential and concentrations for the CRN model. The system is stimulated from $t = 20$ ms to $t = 21$ ms with a constant external current of 80 mA.

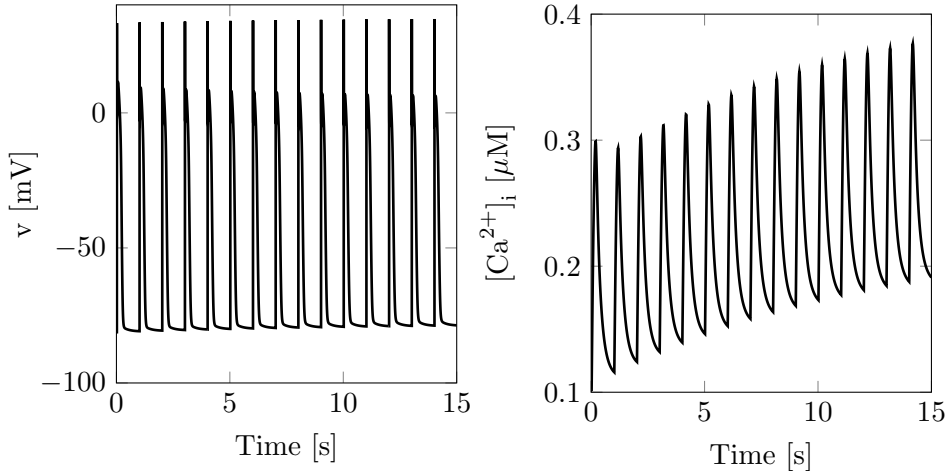


Figure 2.7: Evolution of v and $[\text{Ca}^{2+}]_i$ in a system modeled using the CRN equations and paced with frequency 1 Hz for 15 heartbeats.

The response to multiple stimulations – in terms of transmembrane potential and intracellular calcium concentration – of a cellular system described using the CRN model is depicted in Fig. 2.7. In this example, the cell is paced with constant currents of 80 mA at 1 Hz for 15 s. It appears that, while the maximum and minimum value of v remain almost constant for the whole duration of the simulation, the resting value of $[\text{Ca}^{2+}]_i$ shows a tendency to slightly increase from a starting value of $0.1 \mu\text{M}$ before settling to a value of around $0.2 \mu\text{M}$.

The results in Fig. 2.6 and Fig. 2.7 have been obtained with a timestep of $\Delta t = 5 \times 10^{-3}$ ms by solving the system with the backward Euler method. Such small timesteps are necessary to obtain sufficiently accurate approximations of the system state and to ensure the stability of the method because of the spike in the transmembrane potential. This means that, when combined to the macroscopic description of the heart tissue (namely the Bidomain model), the CRN will require particularly small timesteps to ensure a good quality of the solution and avoid instabilities.

2.3 The macroscopic model

In the previous sections we have seen how the electrical behaviour of the heart is originated by events happening at the cellular scale. Even though understanding these dynamics is important for a complete description of the heart, modeling macroscopic effects by taking into account every cell of the tissue would be an unreasonable task. Hence, the domain Ω (the heart tissue) is considered as a continuum media. In order to integrate into the model the cellular phenomena, Ω is considered composed by two interpenetrating domains Ω_i and Ω_e representing the intracellular and extracellular space respectively. We associate to each point $\mathbf{x} \in \mathbb{R}^d$ two different values of intracellular and extracellular potential u_i and u_e . These quantities have to be intended as average quantities over a sufficiently small set of adjacent cells. See e.g. [35] for a detailed discussion of these assumptions.

Since the heart tissue is essentially electrically anisotropic – as it is formed by tubular cells with different longitudinal and transversal properties – the local tissue conductivity in the intra- and extracellular space can be described by the two tensors $D_i(\mathbf{x})$ and $D_e(\mathbf{x})$. For each point $\mathbf{x} \in \mathbb{R}^d$, we define an orthonormal basis $\mathbf{a}_l(\mathbf{x})$, $\mathbf{a}_t(\mathbf{x})$ and $\mathbf{a}_n(\mathbf{x})$, where $\mathbf{a}_l(\mathbf{x})$ is parallel to the fibers direction, $\mathbf{a}_t(\mathbf{x})$ is perpendicular to $\mathbf{a}_l(\mathbf{x})$ but laying on the tangent plane to the muscular layer and $\mathbf{a}_n(\mathbf{x})$ is normal to the tangent plane. Following [7], $D_i(\mathbf{x})$ and $D_e(\mathbf{x})$ can be defined as

$$D_{i,e}(\mathbf{x}) = \sigma_l^{i,e}(\mathbf{x})\mathbf{a}_l(\mathbf{x})\mathbf{a}_l^T(\mathbf{x}) + \sigma_t^{i,e}(\mathbf{x})\mathbf{a}_t(\mathbf{x})\mathbf{a}_t^T(\mathbf{x}) + \sigma_n^{i,e}(\mathbf{x})\mathbf{a}_n(\mathbf{x})\mathbf{a}_n^T(\mathbf{x}), \quad (2.3)$$

where $\sigma_l^{i,e}(\mathbf{x})$, $\sigma_t^{i,e}(\mathbf{x})$ and $\sigma_n^{i,e}(\mathbf{x})$ represent the local intra- and extracellular conductivities corresponding to each of the vectors of the local basis. Moreover, similarly to what was done for the Hodgkin-Huxley model, we introduce k recovery or gating variables $\mathbf{w} = \{w_1, w_2, \dots, w_k\}$, modeling the behavior of ionic channels, and m ionic concentrations variables $\mathbf{z} = \{z_1, z_2, \dots, z_m\}$. With

this notation, we finally introduce the the parabolic-parabolic formulation (PP) of the Bidomain equations:

$$\left\{ \begin{array}{ll} c_m \frac{\partial v}{\partial t} - \nabla \cdot (D_i \nabla u_i) + \chi I_{ion}(v, \mathbf{w}, \mathbf{z}) = I_i^s & \text{in } \Omega \times (0, T), \\ -c_m \frac{\partial v}{\partial t} - \nabla \cdot (D_e \nabla u_e) - \chi I_{ion}(v, \mathbf{w}, \mathbf{v}) = I_e^s & \text{in } \Omega \times (0, T), \\ \frac{\partial \mathbf{w}}{\partial t} - \mathbf{F}(v, \mathbf{w}) = \mathbf{0} & \text{in } \Omega \times (0, T), \\ \frac{\partial \mathbf{z}}{\partial t} - \mathbf{G}(v, \mathbf{w}, \mathbf{z}) = \mathbf{0} & \text{in } \Omega \times (0, T), \\ \mathbf{n}^T D_{i,e} \nabla u_{i,e} = 0 & \text{in } \partial\Omega \times (0, T), \\ v = v_0, & \text{in } \Omega \times \{0\}, \\ \mathbf{w} = \mathbf{w}_0, & \text{in } \Omega \times \{0\}, \\ \mathbf{z} = \mathbf{z}_0, & \text{in } \Omega \times \{0\}, \end{array} \right. \quad (2.4)$$

where $v = u_i - u_e$ is the transmembrane potential and $c_m = \chi C_m$, χ being the area of cell membrane per tissue volume and C_m being the capacitance of the membrane, and v_0 , \mathbf{w}_0 and \mathbf{z}_0 are initial conditions on v , \mathbf{w} and \mathbf{z} respectively. The homogeneous Neumann boundary conditions are motivated by the assumption of electrically isolated domain.

Eq. (2.4) consists of two of parabolic equations coupled with a number of ODEs depending on the number of considered ionic species and gating variables. By summing the two PDEs, however, the system can equivalently be rewritten in parabolic-elliptic formulation (PE) as

$$\left\{ \begin{array}{ll} c_m \frac{\partial v}{\partial t} - \nabla \cdot (D_i \nabla v) - \nabla \cdot (D_i \nabla u_e) + \chi I_{ion}(v, \mathbf{w}, \mathbf{z}) = I_i^s & \text{in } \Omega \times (0, T), \\ -\nabla \cdot (D_i \nabla v) - \nabla \cdot ((D_i + D_e) \nabla u_e) = I_e^s + I_i^s & \text{in } \Omega \times (0, T), \\ \frac{\partial \mathbf{w}}{\partial t} - \mathbf{F}(v, \mathbf{w}) = \mathbf{0} & \text{in } \Omega \times (0, T), \\ \frac{\partial \mathbf{z}}{\partial t} - \mathbf{G}(v, \mathbf{w}, \mathbf{z}) = \mathbf{0} & \text{in } \Omega \times (0, T), \\ \mathbf{n}^T D_i \nabla (v + u_e) = 0 & \text{in } \partial\Omega \times (0, T), \\ \mathbf{n}^T (D_i + D_e) \nabla u_e + \mathbf{n}^T D_i \nabla v = 0 & \text{in } \partial\Omega \times (0, T), \\ v = v_0, & \text{in } \Omega \times \{0\}, \\ \mathbf{w} = \mathbf{w}_0, & \text{in } \Omega \times \{0\}, \\ \mathbf{z} = \mathbf{z}_0, & \text{in } \Omega \times \{0\}, \end{array} \right. \quad (2.5)$$

where the first two equations are parabolic and elliptic respectively.

2.3.1 Derivation of the Bidomain equations

In this section, we follow [34] to derive the Bidomain equations under the assumption of no external current.

Let us start by recalling some notions of electromagnetism. We consider a generic medium in a region of space of dimensionality d where we define an electrical field $\mathbf{E} \in \mathbb{R}^d$ and a magnetic field $\mathbf{B} \in \mathbb{R}^d$. The relationship between the two is given by the Maxwell-Faraday equation

$$\nabla \times \mathbf{E} + \frac{\partial \mathbf{B}}{\partial t} = \mathbf{0}. \quad (2.6)$$

We introduce the notion of potential $u \in \mathbb{R}$

$$u = \int_{\Gamma} \mathbf{E} \cdot d\mathbf{l}, \quad (2.7)$$

where Γ is a line connecting the point corresponding to zero potential \mathbf{x}_0 to the point of interest \mathbf{x} . If we assume the magnetic field to be static, Eq. (2.6) implies that \mathbf{E} is a conservative vector field. In this case, (2.7) becomes independent of the path and \mathbf{E} can be expressed as the inverse of the gradient of the potential, i.e

$$\mathbf{E} = -\nabla u.$$

Lastly, we define the current density $\mathbf{J} \in \mathbb{R}^d$ as the electric current per area passing through a transversal cross section, and we state that

$$\mathbf{J} = \sigma \mathbf{E} = -\sigma \nabla u, \quad (2.8)$$

if the medium is isotropic with constant conductivity σ .

Even though the electrical processes in the heart are “fast”, the time variations in the electrical and magnetic fields may be considered negligible for values of physiological conductivities (quasi-static assumption). Hence, Eq. (2.8) holds for the currents in the heart tissue. Moreover, as mentioned in Section 2.3, when dealing with a continuous representation of the heart tissue we assume that at each point of the domain two different values of potential u_i and u_e coexist. Therefore, there exist two current densities \mathbf{J}_i and \mathbf{J}_e

$$\mathbf{J}_{i,e} = -D_{i,e} \nabla u_{i,e},$$

where D_i and D_e are the internal and external conductivity tensors defined in (2.3). Let us consider a volume V enclosing a portion of the cardiac tissue. Because of the conservation of charges, we have

$$\begin{aligned} \frac{\partial}{\partial t} \int_V q_{i,e} ds &= \int_V \frac{\partial q_{i,e}}{\partial t} ds = \\ &= - \int_{\partial V} \mathbf{J}_{i,e} \cdot \mathbf{n} dl + \int_V \phi_{i,e} ds = - \int_V \nabla \cdot \mathbf{J}_{i,e} ds + \int_V \phi_{i,e} ds. \end{aligned} \quad (2.9)$$

Here, \mathbf{n} is the outward directed unit vector normal to ∂V , q_i and q_e represent the charge densities and ϕ_i and ϕ_e take into account the transit of charges from the intra- to the extracellular space and vice versa. Conservation of charges implies also that $\phi_i = -\phi_e$. We remark that first equality in (2.9) is valid under assumptions over the regularity of q_i and q_e (continuity) and the last equality follows from the divergence theorem. Since the control volume V is general, the terms under the integrals in Eq. (2.9) must be equal point-wise in V . Hence, we have

$$\frac{\partial q_{i,e}}{\partial t} = -\nabla \cdot \mathbf{J}_{i,e} + \phi_{i,e}. \quad (2.10)$$

The quantities ϕ_i and ϕ_e are strictly related to the ionic membrane currents I_{ion} . In particular, we assume that $\phi_i = -\chi I_{ion}$ and $\phi_e = \chi I_{ion}$. The multiplication by the geometric term χ is needed because I_{ion} is defined as the current per unit area of the membrane. Hence, in order to find the value of the current per unit volume, I_{ion} must be multiplied by the ratio of membrane surface per unit volume. The signs of the ionic currents come from the fact that we consider as positive the currents going from the intra- to the extracellular space.

We now observe that, since the membrane is thin, accumulated charges from one side end up attracting charges from the other side. In other words, in any point of the cardiac tissue the charges in the extracellular and intracellular spaces must balance, i.e. $q_i + q_e = 0$. This implies that

$$\frac{\partial}{\partial t} (q_i + q_e) = 0.$$

Therefore, by using Eq. (2.10), we find that

$$\frac{\partial q_i}{\partial t} + \frac{\partial q_e}{\partial t} = -\nabla \cdot \mathbf{J}_i - \nabla \cdot \mathbf{J}_e = 0.$$

This is equivalent to

$$\nabla \cdot (D_i \nabla u_i) + \nabla \cdot (D_e \nabla u_e) = \nabla \cdot (D_i \nabla v) + \nabla \cdot ((D_e + D_i) \nabla u_e) = 0,$$

which we identify as the second equation in (2.5). We relate the quantity of charge separated by the membrane to its capacitance c_m using the equation

$$v = \frac{1}{2c_m} (q_i - q_e).$$

By deriving on both sides and by using the fact that $\partial q_i/\partial t = -\partial q_e/\partial t$, we find

$$c_m \frac{\partial v}{\partial t} = \frac{\partial q_i}{\partial t}.$$

By inserting this relation into Eq. (2.10) referred to the intracellular space we finally find

$$\begin{aligned} c_m \frac{\partial v}{\partial t} + \nabla \cdot \mathbf{J}_i + \chi I_{ion} &= c_m \frac{\partial v}{\partial t} - \nabla \cdot (D_i u_i) + \chi I_{ion} = \\ &= c_m \frac{\partial v}{\partial t} - \nabla \cdot (D_i v) - \nabla \cdot (D_i u_e) + \chi I_{ion} = 0, \end{aligned}$$

which we identify with the first equation in (2.5).

Concerning the boundary conditions, we assume that the domain is electrically isolated, meaning that $\mathbf{n}^T \mathbf{J}_i = \mathbf{n}^T \mathbf{J}_e = 0$. Hence

$$\begin{aligned} 0 &= \mathbf{n}^T (D_i \nabla u_i) = \mathbf{n}^T D_i (\nabla v + \nabla u_e) \\ 0 &= \mathbf{n}^T (D_e \nabla u_e) = \mathbf{n}^T D_e \nabla u_e + \mathbf{n}^T D_i \nabla u_i = \mathbf{n}^T (D_i + D_e) \nabla u_e + \mathbf{n}^T D_i \nabla v. \end{aligned}$$

The ionic current I_{ion} is assumed to be dependent on the recovery variables \mathbf{w} and concentration variables \mathbf{c} , introduced in the previous section. The actual expression of the ionic current and of the evolution laws \mathbf{F} and \mathbf{G} in (2.4) and (2.5) varies according to the membrane model that is chosen to complement the PDEs.

For the sake of clarity, we summarize here the assumptions that allow the derivation of the Bidomain equations:

- *Quasi-static assumption:* the rate of change of electric and magnetic fields in the heart are negligible. Hence, the electric field and (consequently) the current density are simply proportional to the gradient of a potential.
- *Charge conservation:* the rate of change of charge of the two spaces in a control volume enclosing no sources is only determined by the current entering the volume in the same space and the ionic current passing from one space to the other.
- *No charge accumulation:* charge accumulation in one space attracts opposite charges from the other side of the membrane.
- *Ionic currents:* the ionic currents are functions of recovery variables, ions concentrations and the transmembrane potential. A membrane description must be used to complete the bidomain model.
- *Isolated heart tissue:* we consider the region of heart tissue electrically isolated, meaning that no currents exit the domain.

2.3.2 Well-posedness of the Bidomain equations

In this section, we recall some results about the uniqueness and existence of the solution of the Bidomain equations as in [7]. We refer the interested reader to [3] for a complete discussion of these topics. These results hold in the case of a single gating variable and without concentration variables. In other words, the formulation of the Bidomain equations that we consider is simplified as

$$\begin{cases} c_m \frac{\partial v}{\partial t} - \nabla \cdot (D_i \nabla v) - \nabla \cdot (D_i \nabla u_e) + \chi I_{ion}(v, w) = I_i^s & \text{in } \Omega \times (0, T), \\ -\nabla \cdot (D_i \nabla v) - \nabla \cdot ((D_i + D_e) \nabla u_e) = I_e^s + I_i^s & \text{in } \Omega \times (0, T), \\ \frac{\partial w}{\partial t} - F(v, w) = 0 & \text{in } \Omega \times (0, T), \\ \mathbf{n}^T D_i \nabla (v + u_e) = 0 & \text{in } \partial\Omega \times (0, T), \\ \mathbf{n}^T (D_i + D_e) \nabla u_e + \mathbf{n}^T D_i \nabla v = 0 & \text{in } \partial\Omega \times (0, T), \\ v = v_0, & \text{in } \Omega \times \{0\}, \\ w = w_0, & \text{in } \Omega \times \{0\}. \end{cases} \quad (2.11)$$

We start by defining the necessary functional spaces. Let $L^p(\Omega)$ be the set of p -integrable functions and $H^p(\Omega)$ the Sobolev space of order p , i.e

$$\begin{aligned} L^p(\Omega) &= \{v : \Omega \rightarrow \mathbb{R} : \|v\|_{L^p(\Omega)} < \infty\}, \\ H^p(\Omega) &= \{v \in L^2(\Omega) : D^\alpha v \in L^2(\Omega) \quad \forall \alpha : |\alpha| < p\}, \end{aligned}$$

where

$$\|v\|_{L^p(\Omega)} = \left(\int_{\Omega} |v(\mathbf{s})|^p ds \right)^{1/p},$$

$\alpha = (\alpha_1, \alpha_2, \dots, \alpha_n)$ is a multi-index (composed by non-negative integers), $|\alpha| = \alpha_1 + \alpha_2 + \dots + \alpha_n$ and

$$D^\alpha v(\mathbf{x}) = \frac{\partial^{|\alpha|} v(\mathbf{x})}{\partial x_1^{\alpha_1} \partial x_2^{\alpha_2} \dots \partial x_n^{\alpha_n}}.$$

We take $V = H^1(\Omega)$, $H = L^2(\Omega)$, U as the space of functions in V with null integral on the domain, which we denote with $U = V/\mathbb{R}$. Namely, we have that, if $v \in V$, then $v - \int_{\Omega} v \in U$. Moreover, let $D(0, T)$ be the set of C^∞ functions on \mathbb{R} with compact support on $(0, T)$.

Let us consider the following hypotheses:

(H₁) Ω has a Lipschitz boundary $\partial\Omega$;

(H₂) $D_{i,e} \in L^\infty(\Omega)$ and the two tensors are continuous elliptic, meaning that there exist $m \in \mathbb{R}$ and $M \in \mathbb{R}$ such that

$$m|\xi|^2 \leq \xi^T D_{i,e} \xi \leq M|\xi|^2 \quad \forall \xi \in \mathbb{R}^d;$$

(H₃) $I_{i,e}^s : [0, +\infty) \rightarrow V'$ and $\int_{\Omega} [I_i^s(\mathbf{s}, t) + I_e^s(\mathbf{s}, t)] ds = 0$ for almost every $t > 0$ (*compatibility condition*);

(H₄) There exist some $p \geq 2$ (if $d = 2$) or $p \in [2, 6]$ (if $d = 3$) such that the Sobolev embedding $V = H^1(\Omega) \subset L^p(\Omega)$ holds;

(H₅) I_{ion} and F are affine with respect to w , meaning that

$$I_{ion}(v, w) = I_{ion}^1(v) + I_{ion}^2(v)w, \quad F(v, w) = F^1(v) + F^2w,$$

where $I_{ion}^1, I_{ion}^2, F^1 : \mathbb{R} \rightarrow \mathbb{R}$ are continuous functions and $F^2 \in \mathbb{R}$;

(H₆) There exist constants $c_i \geq 0$ ($i = 1, \dots, 6$) such that, for any $v \in \mathbb{R}$

$$\begin{aligned} |I_{ion}^1(v)| &\leq c_1 + c_2|v|^{p-1}, \\ |I_{ion}^2(v)| &\leq c_3 + c_4|v|^{p/2-1}, \\ |F^1(v)| &\leq c_5 + c_6|v|^{p/2}; \end{aligned}$$

(H₇) There exist constants $a, \lambda > 0, b, c \geq 0$ such that for any $v, w \in \mathbb{R}$

$$\lambda v I_{ion}(v, w) + w F(v, w) \geq a|v|^p - b(\lambda|v|^2 + |w|^2) - c.$$

We are now ready to give the definition of weak solution of the Bidomain equations.

Definition 1 ([3, Definition 26]) (*Weak solution*) Consider $\tau > 0$ and the three functions $v : t \in [0, \tau) \rightarrow v(t) \in H$, $u_e : t \in [0, \tau) \rightarrow u_e(t) \in H$, $w : t \in [0, \tau) \rightarrow w(t) \in H$. Given $(v_0, w_0) \in H \times H$, then (v, u_e, w) is a weak solution to the Bidomain problem if and only if, for any $T \in (0, \tau)$,

1. $v : [0, T] \rightarrow H$ and $w : [0, T] \rightarrow H$ are continuous, with $v(0) = v_0$ and $w(0) = w_0$ in H ;
2. we have for a.e. $t \in (0, \tau)$ $v(t) \in V$, $u_e(t) \in V/\mathbb{R}$, and $v \in L^2(0, T; V) \cap L^p(Q_T)$, where $Q_T = (0, T) \times \Omega$, and (v, u_e, w) verifies in $D'(0, T)$:

$$\begin{aligned} c_m \frac{d}{dt}(v(t), \tilde{v}) + \int_{\Omega} D_i \nabla(v(t) + u_e(t)) \cdot \nabla \tilde{v} ds + \chi \int_{\Omega} I_{ion}(v(t), w(t)) \tilde{v} ds &= \langle I_i^s(t), \tilde{v} \rangle, \\ \frac{d}{dt}(w(t), \tilde{w}) + \int_{\Omega} F(u(t), w(t)) \tilde{w} ds &= 0, \end{aligned}$$

respectively for all $\tilde{v} \in V$ and for all $\tilde{w} \in H$, and

$$\int_{\Omega} D_i \nabla v(t) \cdot \nabla \tilde{u}_e ds + \int_{\Omega} (D_i + D_e) \nabla u_e(t) \cdot \nabla \tilde{u}_e ds = \langle I_i^s(t) + I_e^s(t), \tilde{u}_e \rangle, \quad \forall \tilde{u}_e \in V/\mathbb{R}.$$

Theorem 1 ([3, Theorem 30]) (*Global existence of a weak solution*) Suppose that Ω and $D_{i,e}$ satisfy hypotheses H_1 and H_2 and I_{ion} and F satisfy hypotheses H_4 - H_7 for some value of $p \geq 2$. Let be given $v_0, w_0 \in H$ and let $I_{i,e}^s \in L^2(\mathbb{R}^+; V')$ satisfy hypothesis H_3 . Then the system (2.11) has a weak solution (u, u_e, w) in the sense of Definition 1 with $\tau = +\infty$.

The next theorem ensures the uniqueness of the solution under the same hypotheses of Theorem 1 and an additional assumption over I_{ion} and F . For every $v, w \in \mathbb{R}$, we define the function $G : \mathbb{R}^2 \rightarrow \mathbb{R}^2$ as

$$G(v, w) = \begin{bmatrix} \mu I_{ion}(v, w) \\ F(v, w) \end{bmatrix}, \quad \text{for some } \mu > 0.$$

Let $\mathbf{z} = (v, w) \in \mathbb{R}^2$, $Q(\mathbf{z}) = [\nabla G(\mathbf{z})^T + \nabla G(\mathbf{z})]/2$ be the symmetric part of ∇G . Let $\lambda_1(\mathbf{z})$ and $\lambda_2(\mathbf{z})$ be its eigenvalues, with $\lambda_1(\mathbf{z}) \leq \lambda_2(\mathbf{z})$.

Theorem 2 ([3, Theorem 32]) *If there exists $c \in \mathbb{R}$ such that, for all $\mathbf{z} = (v, w) \in \mathbb{R}^2$,*

$$\lambda_2(\mathbf{z}) \geq \lambda_1(\mathbf{z}) \geq C,$$

then the solution obtained in Theorem 1 is unique.

These theorems were used in [3] to show the well-posedness of the Bidomain equations coupled with simple ionic models accounting for only one gating variable. Among them, we find the already cited FHN and Roger-McCulloch models.

2.3.3 The Monodomain model: motivation and equations

Even though the Bidomain model provides an accurate description of the electrical activity of the cardiac myocardium, there are a few practical problems that make large-scale numerical simulations difficult. First of all, the sharpness of the transmembrane potential upstroke imposes constraints on the maximum timestep that can be used. According to [7], a restriction on the timestep is $\Delta t \leq 0.1$ ms, while the phenomena we are interested in (such as the action potential) have time scales of the order of hundreds of milliseconds. Moreover, mainly because of the homogeneous Neumann conditions on the boundaries, the conditioning of the linear system arising from the discretization of the equations tends to deteriorate the convergence of the numerical methods in 3D problems if no special preconditioner is used. Some work in this direction has been done in [5] for simulations of the Bidomain equations using the Isogeometric Analysis.

The Monodomain model derives from the Bidomain one after assuming that the intra- and extracellular media have the same anisotropy ratio ($\lambda = \sigma_l^e/\sigma_l^i = \sigma_t^e/\sigma_t^i = \sigma_n^e/\sigma_n^i$). The Monodomain equations read

$$\begin{cases} c_m \frac{dv}{dt} - \nabla \cdot (D \nabla v) + \chi I_{ion}(v, \mathbf{w}, \mathbf{c}) = I_{app} & \text{in } \Omega \times (0, T) \\ \frac{d\mathbf{w}}{dt} = \mathbf{R}(v, \mathbf{w}) & \text{in } \Omega \times (0, T), \\ \frac{d\mathbf{c}}{dt} = \mathbf{S}(v, \mathbf{w}, \mathbf{c}) & \text{in } \Omega \times (0, T), \\ \mathbf{n}^T D \nabla v = 0 & \text{in } \partial\Omega \times (0, T), \\ v = v_0, & \text{in } \partial \times \{0\}, \\ \mathbf{w} = \mathbf{w}_0, & \text{in } \Omega \times \{0\}, \\ \mathbf{z} = \mathbf{z}_0, & \text{in } \Omega \times \{0\}. \end{cases}$$

These equations were used in [24, 25] to simulate the action potential on the same LA geometry that will be used in the numerical simulation involving both atria in Chapter 5. In that case, the Monodomain model was coupled to the Aliev-Panfilov [1] and the Mitchell-Schaeffer [23] reduced models. The assumption of equal anisotropy ratio is unfortunately too restrictive to make the

Monodomain model suitable in many applications [34]. Even with the support of empirical data it is in fact difficult to specify the value λ such that the conductivities used in the simulations better approximate the physical ones. Moreover, most physiological phenomena can not be simulated when the anisotropy ratio is assumed to be constant across all directions. Therefore, even though the Monodomain model is convenient both for numerical computations and analysis, the Bidomain model is still the method of reference for realistic simulations in many occasions.

Chapter 3

Isogeometric Analysis

In the Finite Element Method (FEM) differential problems are solved on polygonal or polyhedral meshes. There are many examples of practical applications, however, in which the domain of interest cannot be exactly represented by means of polygons or polyhedra. In such cases the *mesh generation* is the typical intermediate step linking the geometry design to a suitable solution of the Partial Differential Equation (PDE) defined on such geometry, i.e. the computational domain.

Mesh generation usually constitutes the most critical aspect of the workflow for two reasons. As noted in [9], the first and most important problem is that meshing the geometry often introduces a level of approximation. This is a particularly delicate matter when the geometry presents specific features (e.g. curved surfaces) that are hardly preserved by the discretization. Secondly, the accuracy of the approximate solution heavily depends on the quality of the mesh. For this reason, the mesh creation often ends up taking the large majority (on average around 80%, according to some estimates [9]) of the total time of the problem solution. *Isogeometric Analysis* – often abbreviated IGA – offers a valid alternative to the methods requiring mesh generation. The main idea of the approach is to exploit the same basis functions for the geometry design and the construction of the functional space of the solution. This allows to completely preserve the original geometry.

This chapter focuses on the main concepts of IGA and follows the order used in [9]. We start by presenting the most commonly used basis functions, namely B-splines and NURBS. Then, we analyze the method itself. As it will be clear, it is closely related to FEM.

3.1 B-splines and NURBS

3.1.1 Knot vectors and basis functions

Let us start by defining the fundamental terminology that will be used throughout this thesis.

We define *knot vector* $\Xi = \{\xi_1, \xi_2, \dots, \xi_N\}$ a set of N non necessarily distinct *knots* $\xi_i \in \mathbb{R}$. We always assume that the individual knots are listed in increasing order, i.e. $\xi_1 \leq \xi_2 \leq \dots \leq \xi_N$. A *knot span* or *element* is defined as the interval $[\xi_i, \xi_{i+1}]$, where ξ_i and ξ_{i+1} are consecutive and possibly coincident knots. Therefore, the interval $[\xi_1, \xi_N]$ is divided into multiple knot spans. Our goal is to define a set of basis functions over the interval $[\xi_1, \xi_N]$ that will depend on the definition of the knot vector. In order to do this, we introduce the quantities n and p , which represent respectively the number of basis functions and the order of the piecewise polynomials that will constitute them. We use the notation $N_{i,p}$ to denote the i^{th} basis function of order p . The number of knots N must satisfy the relation

$$N = n + p + 1.$$

With these definitions, we introduce the basis functions of order zero as

$$N_{i,0}(s) = \mathcal{I}_{[\xi_i, \xi_{i+1})}(s) \quad 1 \leq i \leq n, \quad (3.1)$$

where $\mathcal{I}_{[a,b)}$ is the indicator function of the interval $[a, b)$ (we use round brackets when the corresponding extrema is not included in the interval). Higher order basis functions are obtained from

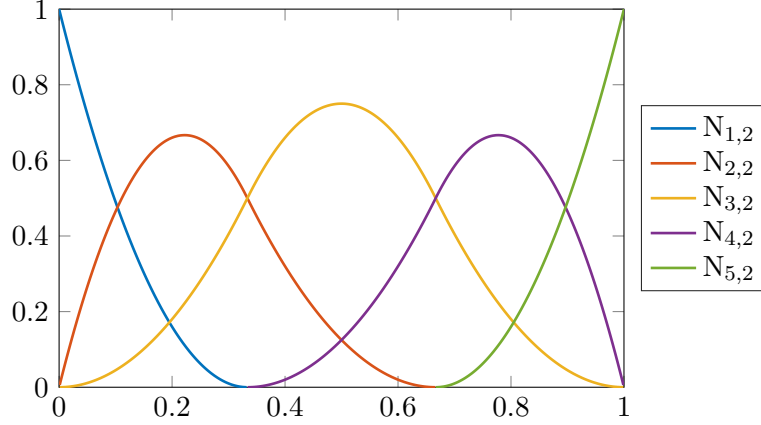


Figure 3.1: Basis functions corresponding to the knot vector $\Xi = \{0, 0, 0, 1/3, 2/3, 1, 1, 1\}$. We have $p = 2$, because the first and last knots are repeated three times, and $n = p + N_{el} = 5$.

(3.1) using the following Cox-de Boor recursion formula [11]:

$$N_{i,p}(s) = \frac{\xi - \xi_i}{\xi_{i+p} - \xi_i} N_{i,p-1}(s) + \frac{\xi_{i+p+1} - \xi}{\xi_{i+p+1} - \xi_{i+1}} N_{i+1,p-1}(s) \quad 1 \leq i \leq n. \quad (3.2)$$

Since we do not impose the constraint of unique knots, it is important to notice that (3.2) may lose sense when two knots are coincident. In such cases, we assume $0/0 := 0$.

Before analyzing the properties of these basis functions we have to introduce some characterization for the knot vectors. We define the knot vector $\Xi = \{\xi_1, \xi_2, \dots, \xi_N\}$ as *uniform* if the individual knots are equally spaced, even if they are repeated, and as *open* if the first and the last knots are repeated $p + 1$ times, namely $\xi_1 = \xi_2 = \dots = \xi_{p+1}$ and $\xi_{N-p} = \xi_{N-p-1} = \dots = \xi_N$. From now on we will always consider open knot vectors. We observe that, in this case, we have $N = 2(p + 1) + N_{in}$, where N_{in} is the number of internal knots, and $N_{in} = N_{el} - 1$, where N_{el} is the number of elements with positive or even zero length. Hence

$$N = 2p + N_{el} + 1 = n + p + 1,$$

which implies $n = p + N_{el}$. We have then that, given any open vector, p and n are determined by the relations above; see Fig. 3.1. Let us now consider the properties of the basis functions.

- **Support and regularity.** Since Eq. (3.2) defines the generic function of order p as combination of polynomials of order $p - 1$ on the elements multiplied by polynomials of first order, it follows that $N_{i,p}$ is polynomial of order p on the elements. Moreover, the support of $N_{i,p}$ is the union of the supports of $N_{i,p-1}$ and $N_{i+1,p-1}$ and corresponds to $p + 1$ contiguous elements. The basis functions inherit the regularity of polynomials inside the elements, i.e. $N_{i,p} \in C^\infty(\cup_{i=1}^{N-1}(\xi_i, \xi_{i+1}))$. In correspondence of the individual knot, the regularity of the basis functions is subject to the multiplicity of the knot itself. In particular, the number of continuous derivatives in ξ_i is $p - m_i$, m_i being the multiplicity of the knot (see Fig. 3.2).
- **Partition of unity.** The basis functions evaluated at the same point $\bar{\xi}$ constitute a partition of the unity for a fixed value of p , i.e.

$$\sum_{i=1}^n N_{i,p}(\bar{s}) = 1, \quad N_{i,p}(\bar{s}) \in [0, 1].$$

Basis functions of dimension $d > 1$ are simply obtained as tensor product of d univariate basis functions, non necessarily generated using the same knot vector. For example, if $d = 2$ and $\{N_{i,p}\}_{i=1}^n$ and $\{M_{i,q}\}_{i=1}^m$ are the two sets of basis functions, then

$$H(s, t) = \sum_{i=1}^n \sum_{j=1}^m N_{i,p}(s) M_{j,q}(t). \quad (3.3)$$

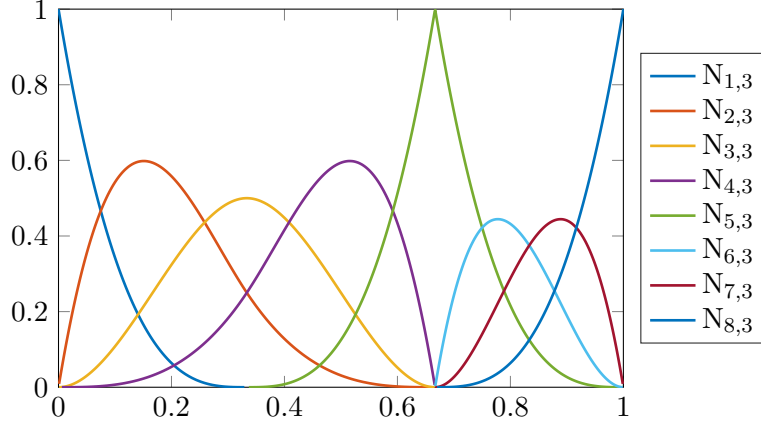


Figure 3.2: Basis functions generated by $\Xi = \{0, 0, 0, 0, 1/3, 2/3, 2/3, 2/3, 1, 1, 1, 1\}$, with $p = 3$ and $n = 8$. The basis is C^0 -continuous in correspondence of $\xi = 2/3$, because the multiplicity of the point equals the order of the polynomials. We remark that the basis is interpolatory at the same point.

The multi-dimensional basis functions share the basic properties of the univariate ones. We never consider bases of dimensionality higher than three and we use the letters $\mathbf{s} = [s, t, w]^T$ for denoting the variables in the three parametric directions.

3.1.2 B-spline geometries

The basis functions we defined in the previous subsection can be used for creating geometrical objects. A *B-spline* curve, for example, is a one-dimensional manifold which is defined as linear combination of univariate basis functions and some two/three dimensional coefficients called *control points*. More precisely, if $\{N_{i,p}\}_{i=1}^n$ is the set of basis functions generated by $\Xi = \{\xi_1, \xi_2, \dots, \xi_N\}$, $\{\mathbf{B}_i\}_{i=1}^n \in \mathbb{R}^d$ with $d = 1, 2$ or 3 is the set of control points, then the curve $\mathbf{C} : [\xi_1, \xi_N] \rightarrow \mathbb{R}^d$ with $d = 1, 2$ or 3 is defined as

$$\mathbf{C}(s) = \sum_{i=1}^n N_{i,p}(s) \mathbf{B}_i.$$

We similarly define a B-spline surface $\mathbf{S} : [\xi_1, \xi_N] \times [\eta_1, \eta_M] \rightarrow \mathbb{R}^d$ with $d = 2$ or 3 by considering the linear combination of two-dimensional basis functions computed as in (3.3) and control points, thus finding

$$\mathbf{S}(s, t) = \sum_{i=1}^n \sum_{j=1}^m N_{i,p}(s) M_{j,q}(t) \mathbf{B}_{i,j}.$$

Finally, we define a B-spline solid $\mathbf{S} : [\xi_1, \xi_N] \times [\eta_1, \eta_M] \times [\zeta_1, \zeta_L] \rightarrow \mathbb{R}^3$ as a linear combination of three dimensional basis functions, obtained as tensor product of three sets of univariate basis functions, and the control points:

$$\mathbf{S}(s, t, w) = \sum_{i=1}^n \sum_{j=1}^m \sum_{k=1}^l N_{i,p}(s) M_{j,q}(t) P_{k,r}(w) \mathbf{B}_{i,j,k}.$$

Curves, surfaces and solids inherit the properties of the basis that generated them. For example, consider the case of Fig. 3.3 (left), where a curve has been created using the basis functions depicted in Fig. 3.2. Such basis is interpolatory and C^0 -continuous at the parametric point $s = 2/3$. As a consequence, the corresponding curve passes through the control point $(1, 0.75)$, which also represents a point of discontinuity for the tangent.

A crucial aspect of FEM simulations is the possibility of tuning the element size of the mesh according to the requirements of the solution. The trade-off is between the accuracy of the solution and the computation time. In the case of B-spline objects, the refinement procedure aims at increasing the variety and quality of the basis without changing the parametrization. This is done

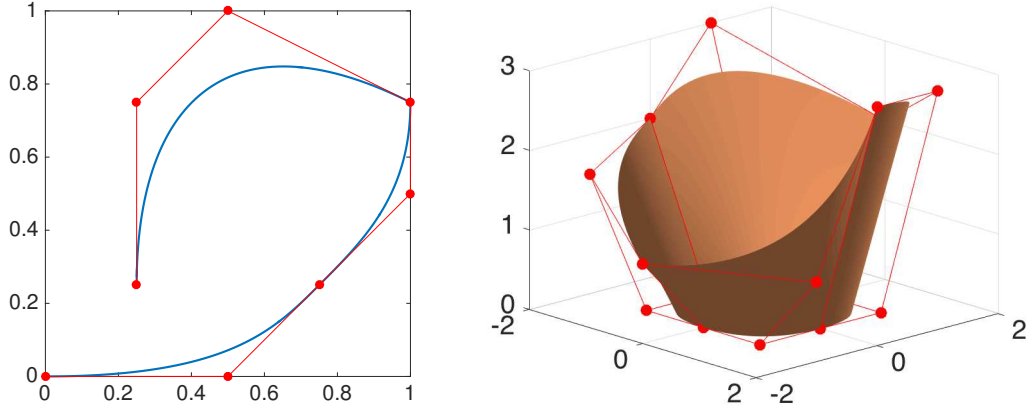


Figure 3.3: Examples of a B-spline curve (left) and a B-spline surface (right). Control points are marked with red dots.

by increasing the number of basis functions (*h-refinement*), increasing the order of the polynomials (*p-refinement*) or both (*k-refinement*) [26]:

- *h-refinement* consists in adding new knots to the knot vector. More specifically, if $\Xi = \{\xi_1, \xi_2, \dots, \xi_N\}$ is the original knot vector, we create an extended knot vector Φ by adding m internal knots to Ξ ; we have then that $\Phi = \{\phi_1 = \xi_1, \phi_2, \dots, \phi_{N+m} = \xi_N\}$. In order to maintain the parametrization of entities, the control points $\mathcal{B} = \{\mathbf{B}_1, \mathbf{B}_2, \dots, \mathbf{B}_n\}$ must be transformed into $\bar{\mathcal{B}} = \{\bar{\mathbf{B}}_1, \bar{\mathbf{B}}_2, \dots, \bar{\mathbf{B}}_{n+m}\}$ following the rule

$$\bar{\mathcal{B}} = T^p \mathcal{B},$$

where

$$T_{ij}^0 = I_{[\xi_j, \xi_{j+1})}(\phi_i)$$

and

$$T_{ij}^{q+1} = \frac{\phi_{i+q} - \xi_j}{\xi_{j+q} - \xi_i} T_{ij}^q + \frac{\xi_{j+q+1} - \phi_{i+q}}{\xi_{j+q+1} - \xi_{j+1}} T_{i(j+1)}^q \quad q = 0, 1, \dots, p-1.$$

- *p-refinement* consists in elevating the order p of the polynomials forming the basis. For this reason, the procedure is sometimes called *order elevation*. In order to keep unchanged the number of continuous derivatives across the knots, which, as we already mentioned, is equal to $p - m_i$, the multiplicity of each of the knots must be also increased.
- *k-refinement* is a combination of *p-refinement* and *h-refinement*. During *k-refinement* first the order of the basis is elevated and then a new knot is inserted. We remark that *h-refinement* and *p-refinement* are not commutative. Indeed, if we start with *h-refinement* and add a new knot ξ_i with multiplicity $m_i = 1$, and then elevate the order of the basis from p to $p + 1$, the regularity of the basis in ξ_i is \mathcal{C}^{p-1} . However, by inverting the order of the refinements, the resulting basis would be \mathcal{C}^p across ξ_i , because the multiplicity of the new knot would not be incremented by the *p-refinement*. Therefore, in order to correctly apply *k-refinement* to a knot vector, *h-refinement* must be executed after *p-refinement*.

3.1.3 NURBS

Even though the B-spline basis defined by (3.2) allows to create a large variety of geometries, many very commonly used objects can not be designed using it. Most notably, circles and solids

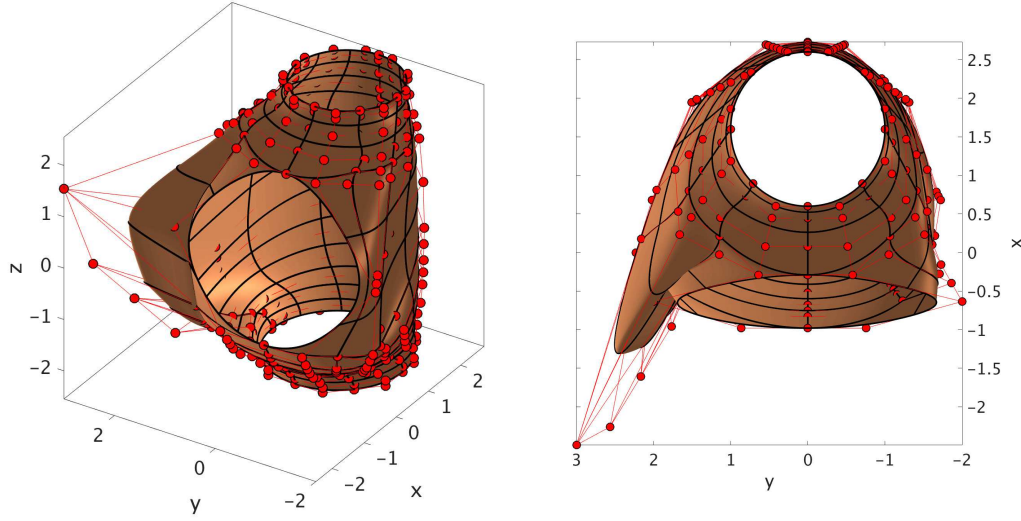


Figure 3.4: Views of the right atrium surface generated as a single patch using NURBS. Control points are marked with red dots.

built using circular shapes are not exactly represented by polynomial bases. In order to include also these cases we have to introduce the concept of *Non-Uniform Rational B-Splines* (NURBS). NURBS entities are obtained through projection in \mathbb{R}^d of B-spline objects living in \mathbb{R}^{d+1} . From the algebraic point of view, this means that we have to introduce a new basis for NURBS as

$$R_i^p(s) = \frac{N_{i,p}(s)\omega_i}{W(s)},$$

where

$$W(s) = \sum_i^n N_{i,p}(s)\omega_i$$

is called *weighting function* and $\{\omega_i\}_{i=1}^n$ are called *weights*. The NURBS curve can be then defined as

$$\mathbf{C}(s) = \sum_i^n R_i^p(s)\mathbf{B}_i.$$

It is now natural to extend this definition of basis also to manifolds of higher dimensions, thus finding

$$R_{i,j}^{p,q}(s,t) = \frac{N_{i,p}(s)M_{j,q}(t)\omega_{i,j}}{\sum_{a=1}^n \sum_{b=1}^m N_{a,p}(s)M_{b,q}(t)\omega_{a,b}},$$

$$R_{i,j,k}^{p,q,r}(s,t,w) = \frac{N_{i,p}(s)M_{j,q}(t)L_{k,r}(w)\omega_{i,j,k}}{\sum_{a=1}^n \sum_{b=1}^m \sum_{c=1}^l N_{a,p}(s)M_{b,q}(t)L_{c,r}(w)\omega_{a,b,c}}.$$

3.1.4 Example: design of a simplified right atrium

In order to illustrate how the geometric concepts introduced in the previous sections can be used to generate geometries, we provide as example the creation of the surface of an idealized right atrium (RA) using quadratic NURBS, namely NURBS derived from a quadratic B-spline basis. The same geometry, which is shown in Fig. 3.4, will be used in the Chapter 5 for solving the Bidomain equations. We refer the reader to [24] for an example of geometry generation (in the specific case, the left atrium) using the same approach. The geometry is created using a MATLAB package called GeopDEs [12].

The basic strategy for generating the surface is to start with a simplified geometry, which can be parametrized using a very small number of knots in the two parametric dimensions and to

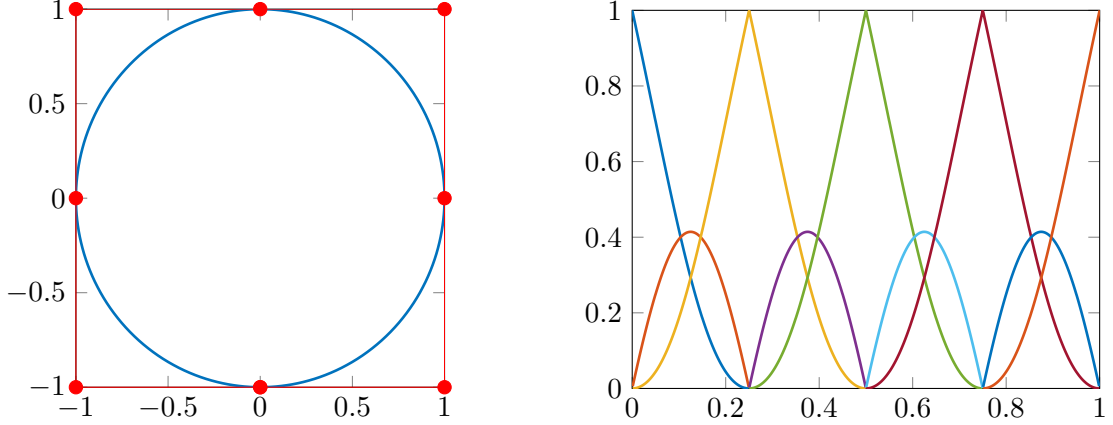


Figure 3.5: On the left, unit circle created using NURBS generated by the knot vector $\Xi = [0, 0, 0, 1/4, 1/4, 1/2, 1/2, 3/4, 3/4, 1, 1, 1]$, with weights equal to $2^{-1/2}$ for knots corresponding to corners and 1 elsewhere. The corresponding basis is shown on the right.

gradually add the more high level features. This is achieved by enriching our basis through knot insertion, that gives us more freedom to modify the surface with precision without changing its parametrization. Even though we would like to obtain a result as smooth as possible, sometimes we are obliged to introduce double knots (e.g. for generating the tricuspid valve). The choice of starting with a simple geometry comes from the fact that when the basis is poor and does not have many repeated knots it is relatively easy to limit the lines with discontinuous derivatives (remember that, as we consider bases with $p = 2$ in both parametric directions and the geometry inherits the regularity properties of the basis, repeated knots in one parametric direction reflect in discontinuous first derivatives along the parametric line corresponding to those knots). Therefore, after reducing the continuity of the basis for a new feature, we have to take care of the critical points and to try to restore the smoothness of the surface, before considering to increase its complexity.

The RA is endowed with three openings for the blood flow: two inflow veins (superior and inferior venae cavae) and the tricuspid valve, which separates the RA from the right ventricle. The two veins are approximately coaxial. Moreover, the atrium has an auricle located at its right when viewed from the posterior.

We aim at creating a simple geometry with two coaxial pipes (representing the veins) and a central bulge. At this moment, we do not account for neither the valve nor the auricle. We start with the two knot vectors

$$\begin{aligned}\Xi_1 &= [0, 0, 0, 1/4, 1/4, 1/2, 1/2, 3/4, 3/4, 1, 1, 1], \\ \Xi_2 &= [0, 0, 0, 1/4, 1/2, 3/4, 1, 1, 1],\end{aligned}$$

which correspond to the two parametric directions s and t . Our choice of knot vectors automatically defines the number of control points that we have to place. In particular, we have $n_1 = 9$ and $n_2 = 6$, hence $n = 54$. The first knot vector, Ξ_1 , can be used to create circles; Fig. 3.5 shows the location of the control points and weights necessary to do so. Therefore, we identify the first parametric direction as the radial direction and the second parametric direction as the longitudinal direction (parallel to the axis of the pipes and the z axis). We place the control points $\mathbf{B}_{i,j}$ so that, for each fixed value of $j = 1, \dots, 6$, the points are arranged as shown in Fig. 3.5 in planes perpendicular to z at increasing heights. The radius of the circles are smaller for $j = 1, 2$ and $j = 5, 6$, because these values correspond to the two venae. The result of this first step is shown in Fig. 3.6(a). We remark that, at this point, the geometry potentially presents C^0 lines in the t direction, which are smooth because of the special disposition of the control points. To see why this is the case, consider the circle, which is smooth even though its basis is C^0 -continuous across the internal knots because each of the critical control points – i.e. where the curve passes through the control point – is aligned with other two.

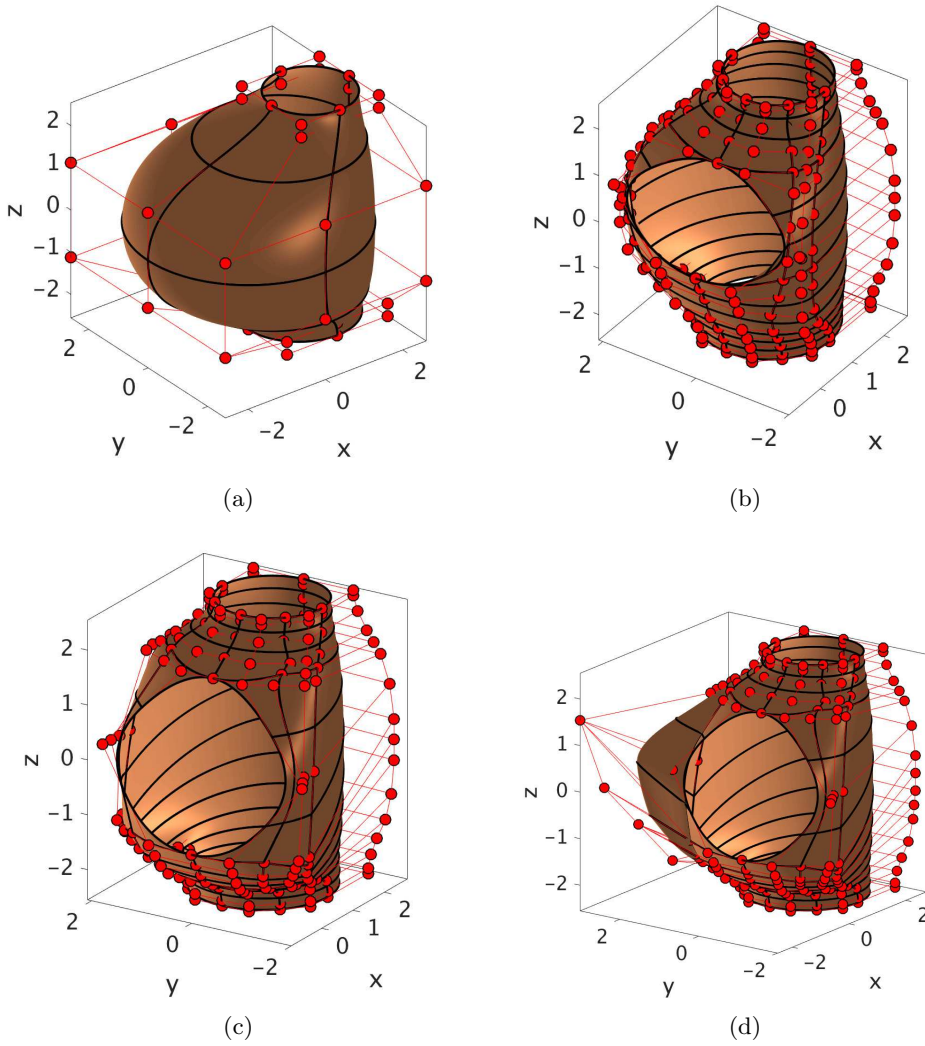


Figure 3.6: RA geometry creation at different steps. Control points are marked with red dots.

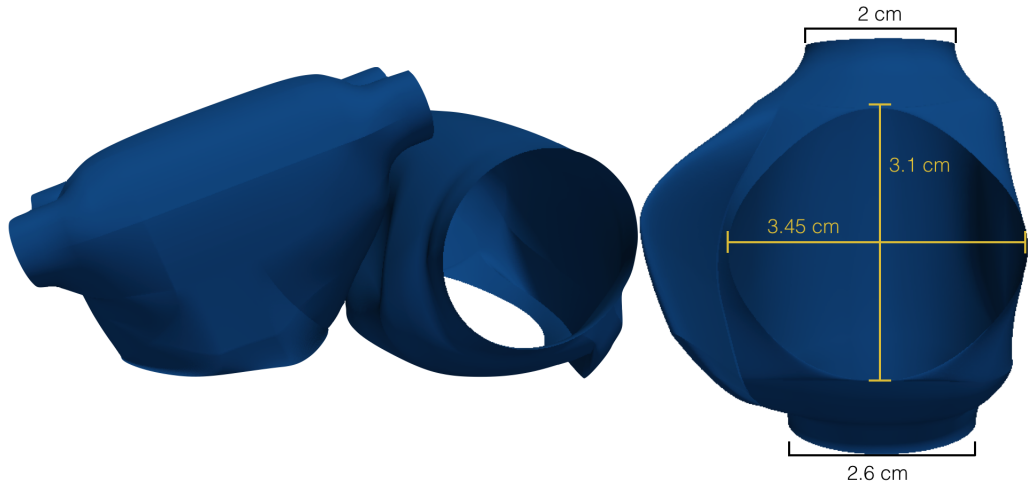


Figure 3.7: Views of the rendered atria (on the left). The LA geometry has been used in [24, 25]. We referred to other 3D models of the heart (as in [8, 32]) for the positioning of the two atria. Radius of the two venae (superior at the top, inferior at the bottom) and dimensions of the tricuspid valve (on the right).

Now we want to open the tricuspid valve in the bulge. Before doing that, we adjust the shape of the atrium and reduce the roundness of the central part by moving the control points without altering the smoothness of the surface. The valve can be created only in the location where the first and last point of each circle overlap, because moving the other control points would cause a deformation without opening holes in the surface. In order to obtain a quasi-circular shape of the valve, it is necessary to introduce two double knots and other single knots in the second parametric direction. We also add two double knots $1/8$ and $7/8$ to the first parametric direction to have a better control over the behavior of the geometry in the longitudinal direction. Fig. 3.6(b) shows the result obtained after moving apart the central points of the joint.

Next, we need to increase the size of the valve so that it matches physiological values. Our valve has approximately the right width but its height is too small. This problem can be solved by moving the points at the right, left and bottom of the valve – we refer to Fig. 3.6(b) for the positions of such points – towards the negative direction of the z axis. However, because of the C^0 lines that we introduced, this operation causes discontinuities in the result. The critical points must be treated individually by trying to align the control points surrounding them; after doing so, we get the result shown in Fig. 3.6(c).

As a final step, we want to attach the auricle to the RA. This is simply attained by moving a line of control points to the left of the valve (from the frontal view) away from the body of the atrium. We remark that such points must not correspond to a C^0 line: in fact, since the surface passes exactly through the control points defining C^0 lines, moving those points would result in a sharp auricle. Fig. 3.6(d) shows the the result we get after fixing all the regularity problems caused by the auricle generation.

The geometry shown in Fig. 3.4 is obtained from 3.6(d) after minimal changes. For example, the side of the atrium opposite to the valve has been modified so that the RA could be placed near the left atrium geometry used in [24, 25] without intersecting; see Fig. 3.7 (left).

3.2 Solving PDEs using Isogeometric Analysis

The method that will be used for solving the Bidomain equations is the Galerkin's method. Rather than searching the solution in the classic FEM functional spaces, however, we will use the basis functions used for the geometry creation for the search space. In order to define a functional space on the geometry, we formalize the notation used in the previous sections. We introduce the map

$$\boldsymbol{\varphi}(\mathbf{s}) = \sum_{i=1}^n \hat{N}_i(\mathbf{s}) \mathbf{B}_i : \hat{\Omega} \rightarrow \Omega \quad (3.4)$$

from the parameter domain $\hat{\Omega} \subset \mathbb{R}^{d_1}$ to the geometry of interest $\Omega \subset \mathbb{R}^{d_2}$. We adopted the hat notation to denote entities living in the parameter space. In the application of the Bidomain equations to the atria, we have $d_1 = 2$ and $d_2 = 3$. Inspired by (3.4), we define a function $\hat{u} : \hat{\Omega} \rightarrow \mathbb{R}$ as linear combinations of the basis functions, i.e

$$\hat{u}(\mathbf{s}) = \sum_{i=1}^n \hat{N}_i(\mathbf{s}) u_i,$$

where $u_i \in \mathbb{R}$ are called control variables. We now transport the function \hat{u} on Ω through

$$u = \hat{u} \circ \boldsymbol{\varphi}^{-1}, \quad (3.5)$$

which is legit because we assume the geometrical mapping to be invertible a.e. in $\hat{\Omega}$. Eq. (3.5) could be also interpreted as

$$u(\mathbf{x}) = \hat{u}(\boldsymbol{\varphi}^{-1}(\mathbf{x})) = \sum_{i=1}^n \hat{N}_i(\boldsymbol{\varphi}^{-1}(\mathbf{x})) u_i = \sum_{i=1}^n N_i(\mathbf{x}) u_i, \quad (3.6)$$

where $\{N_i\}_{i=1}^n$ are the images through $\boldsymbol{\varphi}$ of the basis on the parametric space. We remark that (3.6) is equivalent to $u \in \text{span}\{N_i\}_{i=1}^n$.

We choose to present the process of solution of PDEs in a non-rigorous fashion through a simple parabolic example with known exact solution. See e.g. [27] for more details about the mathematical treatment of this kind of equations.

3.2.1 Example: the heat equation

We consider the linear heat equation

$$\begin{cases} \frac{\partial u}{\partial t}(\mathbf{x}, t) - D \Delta u(\mathbf{x}, t) = f(\mathbf{x}, t) & \text{in } \Omega \times (0, T), \\ u(\mathbf{x}, t) = \mu(\mathbf{x}, t) & \text{on } \Gamma_D \times (0, T), \\ D \nabla u(\mathbf{x}, t) \cdot \mathbf{n}(\mathbf{x}) = \gamma(\mathbf{x}, t) & \text{on } \Gamma_N \times (0, T), \\ u(\mathbf{x}, 0) = u_0(\mathbf{x}) & \text{on } \Omega, \end{cases} \quad (3.7)$$

where $\Omega \subset \mathbb{R}^d$, $\bar{\Gamma}_N \cup \bar{\Gamma}_D = \partial\Omega$ and $\Gamma_N \cap \Gamma_D = \emptyset$, $D \in \mathbb{R}$, $T \in \mathbb{R}^+$, $u, f, \mu, \gamma : \Omega \times (0, T) \rightarrow \mathbb{R}$, $u_0 : \Omega \rightarrow \mathbb{R}$ and $\mathbf{n}(\mathbf{x})$ is the outward directed unit vector normal to $\partial\Omega$.

Weak formulation of the problem

Let us consider the set of test functions $V = H_{\Gamma_D}^1(\Omega) = \{v \in H^1(\Omega) : v(\mathbf{x}) = 0 \quad \forall \mathbf{x} \in \Gamma_D\}$.

For the sake of clarity, in the following we omit the explicit dependence of functions on space.

By multiplying the first equation in (3.7) by some $v \in V$ and integrating on the whole domain, we get

$$\frac{d}{dt} \int_{\Omega} u(t) v d\mathbf{s} - D \int_{\Omega} \Delta u(t) v(t) d\mathbf{s} = \int_{\Omega} f(t) v d\mathbf{s} \quad \forall t \in (0, T). \quad (3.8)$$

We are allowed to take the time derivative out of the integral under the assumption of continuity of $\partial u/\partial t$. By using Green's formula for the treatment of the diffusion term, we can write

$$\begin{aligned} \int_{\Omega} \Delta u(t) v ds &= - \int_{\Omega} \nabla u(t) \nabla v ds + \underbrace{\int_{\Gamma_D} \nabla u(t) \cdot \mathbf{n} v d\mathbf{l}}_{=0} + \int_{\Gamma_N} \nabla u(t) \cdot \mathbf{n} v d\mathbf{l} \\ &= - \int_{\Omega} \nabla u(t) \nabla v ds + \int_{\Gamma_N} \gamma(t) v d\mathbf{l} \quad \forall t \in (0, T). \end{aligned} \quad (3.9)$$

We observe that the boundary term corresponding to Γ_D in the last equation is zero because $v \in H_{\Gamma_D}^1(\Omega)$. From (3.8) and (3.9) we then get

$$\frac{d}{dt} \int_{\Omega} u(t) v ds + D \int_{\Omega} \nabla u(t) \nabla v ds - D \int_{\Gamma_N} \gamma(t) v d\mathbf{l} = \int_{\Omega} f(t) v ds \quad \forall t \in (0, T).$$

It is important to notice that all the integrals in the last equation exist only if $u(t) \in H^1(\Omega)$ and $\gamma(t) \in L^2(\Gamma_N)$. In order to ensure the existence and uniqueness of the solution, however, we are going to restrict the trial space to $V = H_{\Gamma_D}^1(\Omega) \subset H^1(\Omega)$. We do so by writing $u(t) = \tilde{u}(t) + g(t)$, where $g \in H^1(\Omega)$ is called lifting function and is such that $g|_{\Gamma_D} = \mu(\mathbf{x}, t)$. Moreover, we introduce $\tilde{u}_0 = u_0 - g(0)$. We are now ready to express problem (3.7) in *weak formulation*.

Find, $\forall t \in (0, T)$, $\tilde{u}(t) \in V$ such that:

$$\frac{d}{dt} (\tilde{u}(t), v) + a(\tilde{u}(t), v) = F^t(v) \quad \forall v \in V, \quad (3.10)$$

where

$$\begin{aligned} (\tilde{u}(t), v) &= \int_{\Omega} \tilde{u}(t) v ds, \\ a(\tilde{u}(t), v) &= D \int_{\Omega} \nabla \tilde{u}(t) \cdot \nabla v ds, \\ F^t(v) &= \int_{\Omega} \left[(f(t) - \frac{\partial g(t)}{\partial t}) v - D \nabla g(t) \cdot \nabla v \right] ds + D \int_{\Gamma_N} \gamma(t) v d\mathbf{l}, \end{aligned}$$

and $\tilde{u}(0) = \tilde{u}_0$.

Numerical solution by Isogeometric Analysis

With the purpose of numerically solving problem (3.10), we want to lower the dimensionality of the trial space V . In other words, we want to approximate V with $V_h \subset V$, where V_h can be described using a finite number of basis functions. Now, the standard way to proceed would be to approximate the geometry Ω via a computational mesh and use the lagrangian finite element basis functions to characterize V_h . Instead, we choose to adopt the isogeometric concept. Let us suppose that we have a geometrical mapping of the form (3.4). We therefore define a finite dimensional functional space on Ω using (3.6). However, we can not simply identify V_h with $\text{span}\{N_i\}_{i=1}^n$ because of the requirement $u|_{\Gamma_D} = 0$ if $u \in V_h$. This problem is easily solved by considering only the basis functions satisfying the Dirichlet boundary condition. Let us reorder without loss of generality $\{N_i\}_{i=1}^n$ such that $N_i|_{\Gamma_D} = 0$ if $i \leq n_D$, for some $n_D < n$. We have then $V_h = \text{span}\{N_i\}_{i=1}^{n_D}$.

The semi-discrete formulation of problem (3.10) then reads:

Find, $\forall t \in (0, T)$, $\tilde{u}_h(t) \in V_h$ such that:

$$\frac{d}{dt}(\tilde{u}_h(t), v_h) + a(\tilde{u}_h(t), v_h) = F^t(v_h) \quad \forall v_h \in V_h, \quad (3.11)$$

and $\tilde{u}_h(0) = \tilde{u}_{h,0} \in V_h$, where $\tilde{u}_{h,0}$ is some suitable projection of the initial condition \tilde{u}_0 onto V_h .

We remark that we need to build a suitable $g_h(t)$ such that $u_h(t) = \tilde{u}_h + g_h(t)$ – which is the approximate solution to the original problem – in order to compute $F^t(v_h)$. To do this, we notice that the lifting can be built considering only the basis functions that have non zero value on the Dirichlet boundary, namely

$$g_h(t) = \sum_{i=n_D}^n N_i g_i(t).$$

This way we ensure that $g_h(t) \in \text{span} = \{N_i\}_{i=n_D}^n$ and that it can approximately satisfy the boundary condition for some choice of $g_i(t)$ $i = n_D, \dots, n$. We now notice that, as long as the knot vectors forming the basis are open, in each of the boundary nodes the basis is interpolatory (i.e. $N_i(\mathbf{x}) = 1$, for each node \mathbf{x}). Here, we define as *nodes* the image of the points of the cartesian product of the knots in the parameter space. By defining the nodes as \mathbf{x}_i $i = 1, \dots, n$ we then write

$$g_h(t) = \sum_{i=n_D}^n N_i \mu(\mathbf{x}_i, t),$$

where \mathbf{x}_i $i = n_D, \dots, n$ are the nodes laying on the Dirichlet boundary.

From the bilinearity of (\cdot, \cdot) and $a(\cdot, \cdot)$ and the linearity of $F^t(\cdot)$ it follows that \tilde{u}_h satisfies Eq. (3.11) if and only if

$$\frac{d}{dt}(\tilde{u}_h(t), N_i) + a(\tilde{u}_h(t), N_i) = F^t(N_i) \quad \forall i = 1, \dots, n_D. \quad (3.12)$$

Moreover, we rewrite the left hand-side by expanding \tilde{u}_h on the basis, thus finding

$$\frac{d}{dt} \left(\sum_{j=1}^{n_D} N_j \tilde{u}_j(t), N_i \right) + a \left(\sum_{j=1}^{n_D} N_j \tilde{u}_j(t), N_i \right) = \sum_{j=1}^{n_D} M_{ij} \frac{d\tilde{u}_j}{dt}(t) + \sum_{j=1}^{n_D} K_{ij} \tilde{u}_j(t),$$

where $M_{ij} = (N_j, N_i)$ and $K_{ij} = a(N_j, N_i)$. Hence, the set of n_D equations (3.12) is equivalent to the linear system

$$M \frac{d\tilde{\mathbf{u}}}{dt}(t) + K \tilde{\mathbf{u}}(t) = \mathbf{F}^t \quad \text{with } \tilde{\mathbf{u}}(0) = \tilde{\mathbf{u}}_0, \quad (3.13)$$

where $M \in \mathbb{R}^{n_D \times n_D}$ and $K \in \mathbb{R}^{n_D \times n_D}$ are called respectively *mass* and *stiffness* matrices and are such that $(M)_{ij} = M_{ij}$ and $(K)_{ij} = K_{ij}$, $\tilde{\mathbf{u}}(t) = [\tilde{u}_1(t) \tilde{u}_2(t) \dots \tilde{u}_{n_D}(t)]^T$ is the vector of time-dependent coefficients and $\mathbf{F}^t = [F^t(N_1) F^t(N_2) \dots F^t(N_{n_D})]^T$.

Eq. (3.13) can be turned into fully discrete form by using a numerical scheme for the solution of ODEs. For example, we choose the Backward Euler method, yielding

$$M \frac{\tilde{\mathbf{u}}^{k+1} - \tilde{\mathbf{u}}^k}{\Delta t} = -K \tilde{\mathbf{u}}^{k+1} + \mathbf{F}^{k+1} \quad k \geq 0,$$

or equivalently

$$\tilde{\mathbf{u}}^{k+1} = (M + \Delta t K)^{-1} (M \tilde{\mathbf{u}}^k + \mathbf{F}^{k+1}) \quad k \geq 0, \quad (3.14)$$

with $\tilde{u}_h(0) = \tilde{u}_{h,0}$. By solving (3.14), we can reconstruct the solution $\tilde{u}_h(t)$ as

$$\tilde{u}_h(t) = \sum_{i=1}^{n_D} N_i \tilde{u}_i(t).$$

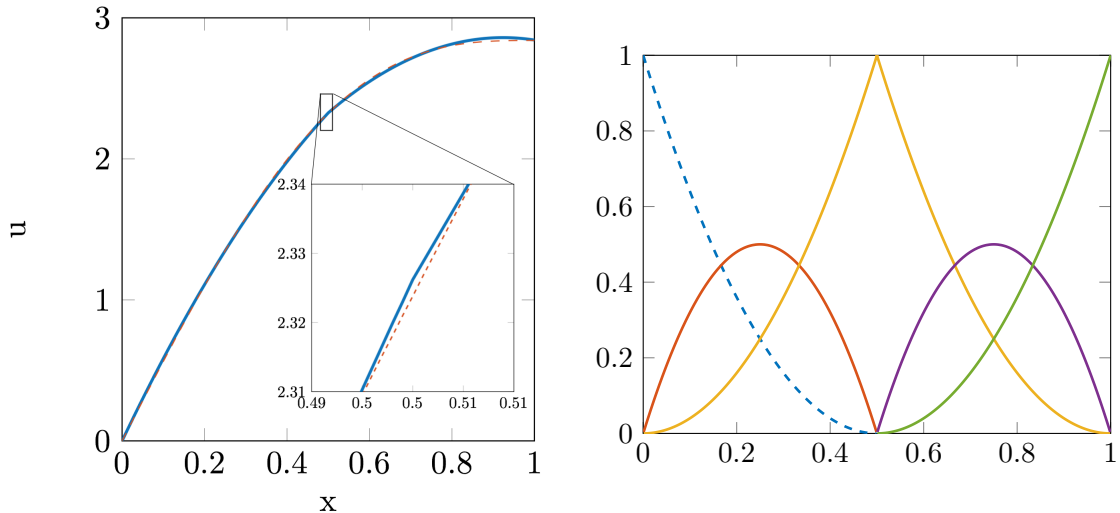


Figure 3.8: On the left, solution of the heat equation at time $t = 1$ (blue solid line) compared to its exact solution (red dashed line). We used the basis generated by $\Xi = [0, 0, 0, 1/2, 1/2, 1, 1, 1]$ (shown on the right). The non-dashed basis functions form a basis for V_h in the case of the considered problem.

To see how the method behaves in practice, we consider the simple case $d = 1$ and $\varphi(s) = s$, hence the case in which $\hat{\Omega} = \Omega = (\xi_1, \xi_N) = (0, 1)$. We choose the following data: $D = 1$, $T = 1$, $\Gamma_D = \xi_1$, $\Gamma_N = \xi_N$, $\mu(\xi_1, t) = \gamma(\xi_N, t) = 0$,

$$\begin{aligned} f(x, t) &= [\pi^2 \sin(\pi x) - \alpha \sin(\pi x) + \pi x]e^{-\alpha t}, \\ u_0(x) &= \sin(\pi x) + \pi x, \end{aligned}$$

with $\alpha = 0.1$. The exact solution of this problem reads

$$u_{ex}(x, t) = [\sin(\pi x) + \pi x]e^{-\alpha t}.$$

As a first goal, we show that the solution inherits the regularity properties of the basis. Let us consider

$$\Xi = [0, 0, 0, 1/2, 1/2, 1, 1, 1].$$

The corresponding basis, which is shown in Fig. 3.8 (right), is composed by piecewise quadratic functions which are C^1 -continuous everywhere except in correspondence of the repeated knot $1/2$. Since our trial space V_h includes functions belonging to the span of the basis and satisfying the Dirichlet boundary condition on the left boundary, we make use of only the non-dashed basis functions in Fig. 3.8 (right).

Fig. 3.8 (left) shows the result obtained at the final time $T = 1$ using a timestep of $\Delta t = 0.01$. We identify two main features of the solution. First, the solution appears qualitatively and quantitatively accurate even with only two elements. In particular, for the relative $L^2(\Omega)$ error we find

$$e_{L^2}^{rel}(T) = \frac{\|u_h(T) - u_{ex}(T)\|_{L^2(\Omega)}}{\|u_{ex}(T)\|_{L^2(\Omega)}} = 2.8 \times 10^{-3}.$$

Secondly, the solution presents a discontinuity of the first derivative in $x = 0.5$, which derives from the choice of the basis. This explains the need of limiting the number of knots with lower continuity that we stressed out in Section 3.1.4 in the example of domain design: not only such points reflect in a non smooth geometry which may appear unnatural and artificial, but they have also consequences on the regularity of the solution to the problem that we are considering.

Finally, we want to compute the convergence of the error with respect to the element size h . Since we are interested in the spatial convergence rather than the time convergence, we set $T = \Delta t = 10^{-12}$, so that we compute only one step of the solution and the error in time is

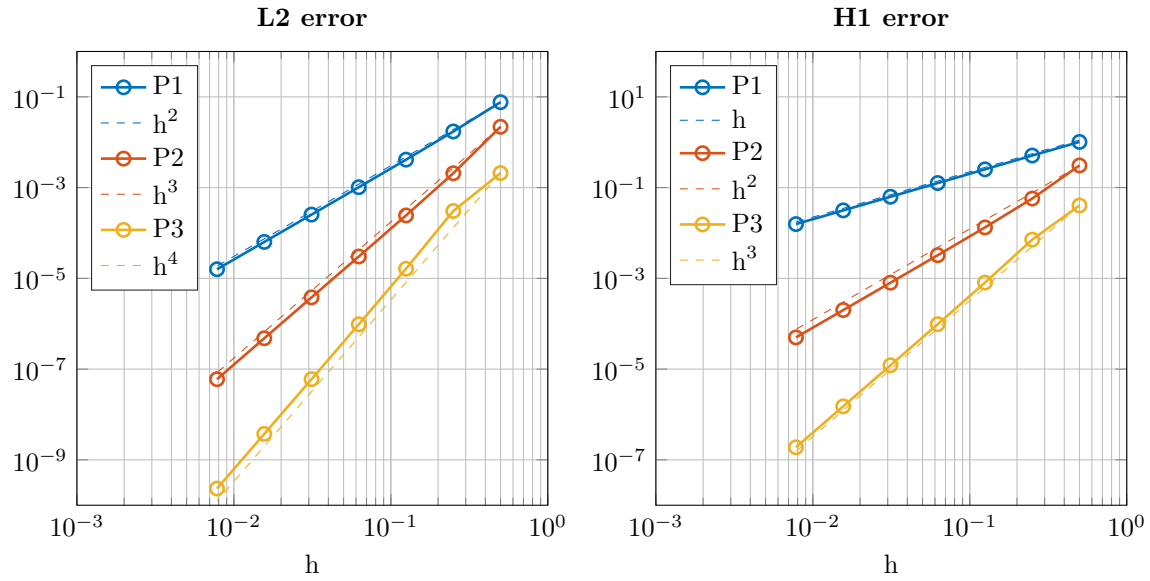


Figure 3.9: Convergence of the $L^2(\Omega)$ and $H^1(\Omega)$ error for the 1D heat equation with respect to the element size h .

negligible if compared to the error in space. Fig. 3.9 shows the convergence of the error in $L^2(\Omega)$ and $H^1(\Omega)$ norms. We find the following orders

$$e_{L^2}(T) = \|u_h(T) - u_{ex}(T)\|_{L^2(\Omega)} \leq Ch^{p+1},$$

$$e_{H^1}(T) = \|u_h(T) - u_{ex}(T)\|_{H^1(\Omega)} \leq Ch^p,$$

which are in agreement with the expected ones from the theory [2].

Chapter 4

Numerical approximation of the Bidomain equations

This chapter deals with the solution of the Bidomain equations, presented in Chapter 2, using IGA as discussed in Chapter 3. We start by deriving the weak formulation of the equations and discretizing the problem, similarly to what has been done for the heat equation in Chapter 3. We move then to some simple test problems to analyze the behavior and properties of the equations in terms of the IGA approximation. In particular, our goal is to evaluate the effects of the isogeometric discretization in terms of velocity and dispersion of the electric signal.

All the simulations presented in this chapter and in Chapter 5 were performed using a C++ library that is developed and maintained within the *Chair of Modeling and Scientific Computing* (CMCS) at EPFL called *isoglib*. This is an efficient tool specifically designed for IGA simulations with support to parallel computations on distributed memory systems. The geometries are generated using the freeware *GeoPDEs* [12] and *MATLAB*.

4.1 Discretization of the Bidomain equations

4.1.1 Weak formulation of the problem

In the following, we are going to use the letter \mathbf{w} to refer to the vector containing all the gating and concentration variables of the ionic model; we assume that the total number of components of \mathbf{w} is N_w . The evolution law for this variable can be written in the form of ODE as for the quantities it represents, i.e.

$$\frac{\partial \mathbf{w}}{\partial t} - \mathbf{F}(v, \mathbf{w}) = \mathbf{0}. \quad (4.1)$$

In order to write the variational formulation of the equations, we use the same functional spaces introduced in Section 2.3.2, i.e. $V = H^1(\Omega)$, $H = L^2(\Omega)$ and $U = V/\mathbb{R}$.

We start by considering the first equation of problem (2.5). By multiplying both sides by a function $\tilde{v} \in V$ and integrating over Ω , we find, for all $t \in (0, T)$,

$$c_m \left(\frac{\partial v}{\partial t}, \tilde{v} \right) - \int_{\Omega} \nabla \cdot [D_i \nabla (u_e + v)] \tilde{v} ds + \chi(I_{ion}(v, \mathbf{w}, \mathbf{c}), \tilde{v}) = (I_i^s, \tilde{v}), \quad (4.2)$$

where we used the notation (\cdot, \cdot) for the usual scalar product in $L^2(\Omega)$. In order to ensure the existence of all the forms in (4.2), we require that $v \in V$, $\partial v / \partial t \in H$ and $u_e \in U$; actually, it would be sufficient to impose $u \in V$, but the more restrictive condition $u \in U$ is needed to ensure the uniqueness of the extracellular potential. By applying the Green's identity to the diffusion term, we find

$$\int_{\Omega} \nabla \cdot [D_i \nabla (u_e + v)] \tilde{v} ds = - \int_{\Omega} [D_i \nabla (u_e + v)] \cdot \nabla \tilde{v} s + \underbrace{\int_{\partial \Omega} \mathbf{n}^T [D_i \nabla (u_e + v)] \nabla \tilde{v} dl}_{=0}$$

where the last term is equal to zero because of the homogeneous Neumann conditions. We introduce the bilinear form $a_i : V \times V \rightarrow \mathbb{R}$ as

$$a_i(\phi, \psi) := \int_{\Omega} (D_i \nabla \phi) \cdot \nabla \psi \, ds,$$

for all $\phi, \psi \in V$. Thus, we write (4.2) as

$$c_m \left(\frac{\partial v}{\partial t}, \tilde{v} \right) + a_i(v, \tilde{v}) + a_i(u_e, \tilde{v}) + \chi(I_{ion}(v, \mathbf{w}), \tilde{v}) = (I_i^s, \tilde{v}).$$

Let us consider the second equation of problem (2.5). We multiply both sides by $\tilde{u}_e \in U$, and then integrate over the domain. After treating the diffusion terms as above, we find

$$\int_{\Omega} (D_i \nabla v + (D_i + D_e) \nabla u_e) \cdot \nabla \tilde{u}_e \, ds - \underbrace{\int_{\partial \Omega} \mathbf{n}^T [D_i \nabla v + (D_i + D_e) \nabla u_e] \tilde{u}_e \, dl}_{=0} = (I_i^s + I_e^s, \tilde{u}_e). \quad (4.3)$$

The last integral is, again, zero because of the homogeneous Neumann boundary conditions. By introducing the bilinear form $a : V \times V \rightarrow \mathbb{R}$ defined as

$$a(\phi, \psi) := \int_{\Omega} [(D_i + D_e) \nabla \phi] \cdot \nabla \psi \, ds,$$

for all $\phi, \psi \in V$, Eq. (4.3) may be rewritten as

$$a_i(v, \tilde{u}_e) + a(u_e, \tilde{u}_e) = (I_i^s + I_e^s, \tilde{u}_e).$$

Eq. (4.1) can be treated by simply multiplying component-wise (Hadamard product) both sides by $\tilde{\mathbf{w}} \in [H]^{N_w}$, and integrating on the domain Ω , thus finding, for all $t \in (0, T)$,

$$\left(\frac{\partial \mathbf{w}}{\partial t}, \tilde{\mathbf{w}} \right) = (\mathbf{F}(v, \mathbf{w}), \tilde{\mathbf{w}}), \quad (4.4)$$

where we used the usual notation (\cdot, \cdot) for the scalar product in $[H]^{N_w}$. By requiring $\mathbf{w} \in [H]^{N_w}$ and $\partial \mathbf{w} / \partial t \in [H]^{N_w}$ we ensure the existence of all the integrals in Eq. (4.4).

We recall that, as explained in 2.3.2, a necessary condition to the well-posedness of the Bidomain equations is the compatibility condition:

$$\int_{\Omega} (I_i^s + I_e^s) \, ds = 0. \quad (4.5)$$

We finally express the weak formulation of the Bidomain equations:

Given $v_0 \in H$, $\mathbf{w}_0 \in [H]^{N_w}$, $I_{i,e}^s \in L^2(\Omega \times (0, T))$ (satisfying the compatibility condition (4.5)), $\mathbf{F} \in [L^2(V, [H]^{N_w})]^{N_w}$, find $v \in L^2(0, T; V)$, $u_e \in L^2(0, T; U)$ and $\mathbf{w} \in [L^2(0, T; [H]^{N_w})]^{N_w}$ such that $\partial v / \partial t \in L^2(0, T; V)$ and $\partial \mathbf{w} / \partial t \in [L^2(0, T; [H]^{N_w})]^{N_w}$, $v(0) = v_0$ and $\mathbf{w}(0) = \mathbf{w}_0$, and $\forall t \in (0, T)$

$$\begin{aligned} c_m \frac{d}{dt} (v, \tilde{v}) + a_i(v, \tilde{v}) + a_i(u_e, \tilde{v}) + \chi(I_{ion}(v, \mathbf{w}), \tilde{v}) &= (I_i^s, \tilde{v}), \\ a_i(v, \tilde{u}_e) + a(u_e, \tilde{u}_e) &= (I_i^s + I_e^s, \tilde{u}_e), \\ \frac{d}{dt} (\mathbf{w}, \tilde{\mathbf{w}}) &= (\mathbf{F}(v, \mathbf{w}), \tilde{\mathbf{w}}), \end{aligned} \quad (4.6)$$

for all $\tilde{v} \in V$, $\tilde{u}_e \in U$, and $\tilde{\mathbf{w}} \in [H]^{N_w}$.

4.1.2 Space and time discretizations

Space discretization

The first problem that we have to solve in the variational formulation derived in the previous section is the infinite dimensionality of the spaces we are using for the search of the solution. Let us consider only the first two variational equations,

$$\begin{aligned} c_m \frac{d}{dt} (v, \tilde{v}) + a_i(v, \tilde{v}) + a_i(u_e, \tilde{v}) + \chi(I_{ion}(v, \mathbf{w}), \tilde{v}) &= (I_i^s, \tilde{v}), \\ a_i(v, \tilde{u}_e) + a(u_e, \tilde{u}_e) &= (I_i^s + I_e^s, \tilde{u}_e). \end{aligned} \quad (4.7)$$

As discussed in Chapter 2, a possible approach for building a finite dimensional space of the solution is to consider the space spanned by the basis functions used for the geometry generation. Let us denote with $V_h \subset V$ the finite dimensional approximation of V built using the basis functions forming the geometry. Hence, we have that, for every $g^h \in V_h$,

$$g^h = \sum_i^N N_i g_i,$$

where $\{N_i\}_{i=1}^N$ are the basis functions and g_i are the corresponding degrees of freedom. We introduce for every $t \in (0, T)$ the approximations of $v(t)$ and $u_e(t)$ in the space V_h , namely

$$\begin{aligned} v^h(t) &= \sum_i^N N_i v_i(t), \\ u_e^h(t) &= \sum_i^N N_i u_i(t), \end{aligned} \quad (4.8)$$

the vectors $\mathbf{v}(t) = [v_1(t) \ \cdots \ v_N(t)]^T$, $\mathbf{u}(t) = [u_1(t) \ \cdots \ u_N(t)]^T$ and

$$\mathbf{z}(t) = \begin{bmatrix} \mathbf{v}(t) \\ \mathbf{u}(t) \end{bmatrix}$$

and the following matrices:

$$\begin{aligned} (M)_{lm} &= (N_m, N_l), \\ (K_i)_{lm} &= a_i(N_m, N_l), \\ (K)_{lm} &= a(N_m, N_l). \end{aligned}$$

We will omit the explicit dependence of time for v^h , u_e^h , \mathbf{v} , \mathbf{u} and \mathbf{z} in the following.

Let us now substitute v and u_e in Eq. (4.7) with their approximation v^h and u_e^h and expand on the basis following Eqs. (4.8). We observe that, if we choose $v_h \in V_h$ and $u_e^h \in V_h$, (4.7) holds for every $\tilde{v}_h \in V_h$ and $\tilde{u}_{e,h} \in V_h$ if and only if it holds for every N_i with $i = 1, \dots, N_w$. Hence, for the first equation in Eq. (4.7) we get

$$c_m \sum_{j=1}^N (N_j, N_k) \frac{d}{dt} v_j + \sum_{j=1}^N a_i(N_j, N_k) v_j + \sum_{j=1}^N a_i(N_j, N_k) u_j + \chi(I_{ion}(v, \mathbf{w}), N_k) = (I_i^s, N_k),$$

which must hold for all $k = 1, \dots, N$. With the notation introduced above, we write, for each $t \in (0, T)$,

$$c_m M \frac{d}{dt} \mathbf{v} + K_i \mathbf{v} + K \mathbf{u} + \chi \mathbf{I}_{ion}^h = \mathbf{I}_i^s, \quad (4.9)$$

with $\mathbf{v}(0) = \mathbf{v}_0$, where $(\mathbf{I}_{ion}^h)_j = (I_{ion}(v^h, \mathbf{w}), N_j)$, $(\mathbf{I}_i^s)_j = (I_i^s, N_j)$ and $\mathbf{v}_0 = [v_{1,0} \ \cdots \ v_{N,0}]^T$ is chosen so that $\sum_{i=1}^N N_i v_{i,0}$ is a good approximation of the initial condition (for example, \mathbf{v}_0 could be chosen to minimize the norm $\|v_0 - \sum_{i=1}^N N_i v_{i,0}\|_{L^2(\Omega)}$). For the time being, we just assume that \mathbf{I}_{ion}^h is given; we will focus on its actual computation later on in this section. Following the same steps of the first equation in (4.7), the second equation becomes, for each $t \in (0, T)$,

$$K_i \mathbf{v} + K \mathbf{u} = \mathbf{I}_i^s + \mathbf{I}_e^s, \quad (4.10)$$

where $(\mathbf{I}_e^s)_j = (I_e^s, N_j)$. Eqs. (4.9) and (4.10) may compactly and conveniently be rewritten as

$$c_m \underbrace{\begin{bmatrix} M & 0 \\ 0 & 0 \end{bmatrix}}_{\mathcal{M}} \frac{d}{dt} \mathbf{z} + \underbrace{\begin{bmatrix} K_i & K_i \\ K_i & K \end{bmatrix}}_{\mathcal{K}} \mathbf{z} = \underbrace{\begin{bmatrix} \mathbf{I}_i^s - \chi \mathbf{I}_{ion}^h \\ \mathbf{I}_i^s + \mathbf{I}_e^s \end{bmatrix}}_{\mathcal{I}}, \quad (4.11)$$

where the entries 0 stand for matrices composed only by zeros and with suitable dimensions. Eq. (4.11) is the semi-discrete formulation of the Bidomain model. It may also be rewritten in form of ODE as

$$\begin{cases} c_m \mathcal{M} \frac{d}{dt} \mathbf{z} = \mathcal{I} - \mathcal{K} \mathbf{z} = G(\mathbf{z}) & t \in (0, T), \\ \mathbf{z}(0) = \mathbf{z}_0, \end{cases} \quad (4.12)$$

where $\mathbf{z}_0 = [\mathbf{v}_0^T \ \mathbf{0}^T]^T$.

Let us now address the discretization of the recovery and concentrations variables \mathbf{w} . A possible approach called *nodal interpolation* [25] would consist in making use of the same basis functions $\{N_i\}_{i=1}^N$ to construct a suitable approximation of $[H]^{N_w}$ and to approximate the third equation in Eq. (4.6) by following the steps of the first two. We choose to follow another path called *gaussian integration* [25]. Let us remark that the variable \mathbf{w} contributes to (4.12) uniquely for the ionic current term \mathbf{I}_{ion}^h . This is computed as

$$(\mathbf{I}_{ion}^h)_j = \int_{\Omega} I_{ion}(v_h, \mathbf{w}) N_j ds. \quad (4.13)$$

The standard strategy in finite element and IGA solvers to compute this kind of integrals is to exploit the special structure of basis functions, which have compact and highly localized support and are piecewise polynomial, and utilize a gaussian quadrature rule on each mesh element. This approach is convenient because, due to the locality of the basis functions, only a very small number of elements contributes to the value of the integrals. Let N_e be the number of elements forming the geometry Ω , K_j be the j^{th} element such that $\bigcup_{j=1}^{N_e} K_j = \Omega$, $\{\mathbf{x}_i^j\}_{i=1}^s$ be the quadrature points on the j^{th} element and $\{\omega_i^j\}_{i=1}^s$ be the associated weights. In the case quadrature rules are used, integral (4.13) can be approximated as

$$\int_{\Omega} I_{ion}(v_h, \mathbf{w}) N_j ds = \sum_{j=1}^{N_e} \int_{K_j} I_{ion}(v_h, \mathbf{w}) N_j ds \approx \sum_{j=1}^{N_e} \sum_{i=1}^s I_{ion}(v_h(\mathbf{x}_i^j), \mathbf{w}(\mathbf{x}_i^j)) N_j(\mathbf{x}_i^j) \omega_i.$$

Therefore, we are not necessarily interested in projecting \mathbf{w} onto a space based on the isogeometric basis. What we actually need is the value of the recovery and concentration variables at the gaussian quadrature points. We consider then the set of $s \times N_e$ vectors $\mathbf{w}_i^j = \mathbf{w}(\mathbf{x}_i^j)$ for $i = 1, \dots, s$ and $j = 1, \dots, N_e$, representing the values of recovery and concentration variables at each quadrature point. The evolution of \mathbf{w}_i^j can be computed through the ODE

$$\begin{cases} \frac{d}{dt} \mathbf{w}_i^j = \mathbf{F}(v_{h,i}^j, \mathbf{w}_i^j) & t \in (0, T), \\ \mathbf{w}_i^j(0) = \mathbf{w}_0(\mathbf{x}_i^j), \end{cases} \quad (4.14)$$

for $i = 1, \dots, s$ and $j = 1, \dots, N_e$, where $v_{h,i}^j = v_h(\mathbf{x}_i^j)$ is the interpolation of the approximate solution v_h in the Gauss point \mathbf{x}_i^j .

We emphasize that this technique for dealing with the recovery, concentration variables and computation of the ionic current is not the only possible; we refer the reader to [25] for other equally valid choices.

Time discretization

In order to derive the fully discrete form of the Bidomain equations we consider a decoupled semi implicit scheme; see e.g. [6,7,15] for other examples of applications of this approach to the Bidomain equations.

We use backward differentiation formulae (BDFs) for the time integration [22]. Let us recall that, given the initial value problem:

$$\begin{cases} \frac{d\mathbf{y}}{dt} = \mathbf{f}(t, \mathbf{y}) & \text{for } t \in (t_0, T), \\ \mathbf{y}(t_0) = \mathbf{y}_0, \end{cases}$$

with $y \in \mathbb{R}^n$, $y_0 \in \mathbb{R}^n$ and $\mathbf{f}: \mathbb{R} \times \mathbb{R}^n \rightarrow \mathbb{R}^n$, a timestep Δt such that $t^k = t_0 + k\Delta t$, the approximate solution at the $(k+1)^{\text{th}}$ timestep \mathbf{y}^{k+1} computed using a BDF scheme of order q satisfies

$$\sum_{i=0}^q \alpha_i \mathbf{y}^{k+1-i} = \Delta t \beta \mathbf{f}(t, \mathbf{y}^{k+1}) \quad \text{for } k \geq q-1, \quad (4.15)$$

where $\mathbf{y}^0 = \mathbf{y}_0$ and $\alpha_i \in \mathbb{R}$ for $i = 0, \dots, q$ and $\beta \in \mathbb{R}$ (with $\alpha_0 \neq 0$ and $\beta \neq 0$) are coefficients depending on the order of the method. We remark that equation (4.15) can always be expressed in the form

$$\alpha \frac{\mathbf{y}^{k+1} - \mathbf{y}_{\text{BDF}}^{k+1}}{\Delta t} = \mathbf{f}(t, \mathbf{y}^{k+1}) \approx \frac{d}{dt} \mathbf{y}(t^{k+1}), \quad (4.16)$$

where $\alpha = \alpha_0/\beta$ and

$$\mathbf{y}_{\text{BDF}}^{k+1} = - \sum_{i=1}^q \frac{\alpha_i}{\alpha} \mathbf{y}^{k+1-i}.$$

The method obtained by applying (4.16) is implicit and requires the solution of a potentially non linear equation at each timestep. In order to decrease the computational cost, we may introduce $\mathbf{y}_{\text{ext}}^{k+1}$: this is an approximation of \mathbf{y}^{k+1} obtained as extrapolation using the values \mathbf{y}^j , with $j = k, \dots, k - (q-1)$. We have then

$$\alpha \frac{\mathbf{y}^{k+1} - \mathbf{y}_{\text{BDF}}^{k+1}}{\Delta t} = \mathbf{f}(t, \mathbf{y}_{\text{ext}}^{k+1}),$$

which is an explicit method of order q .

Let Δt be the timestep of the time discretization and $t^k = k\Delta t$ be the k^{th} timestep. We denote with \mathbf{v}^k and \mathbf{u}^k the values of \mathbf{v} and \mathbf{u} respectively at the k^{th} timestep, and with $\mathbf{w}_i^{j,k}$ the values of \mathbf{w} at the time instance t^k in correspondence of the Gauss quadrature point \mathbf{x}_i^j . The computation of the solution at time $k+1$ through the decoupled scheme, which is a first order splitting scheme, follows these two steps:

1. Suppose to have $\mathbf{v}_{\text{ext}}^{k+1}$ and $\mathbf{w}_{\text{ext},i}^{j,k+1}$, namely the extrapolated values of \mathbf{v} and \mathbf{w}_i^j at the time instance $k+1$. Then, the numerical solution of (4.14) can be computed with

$$\alpha \frac{\mathbf{w}_i^{j,k+1} - \mathbf{w}_{\text{BDF},i}^{j,k+1}}{\Delta t} = \mathbf{F}(v_{h,i}^{j,k+1}, \mathbf{w}_{\text{ext},i}^{j,k+1}),$$

for all $i = 1, \dots, s$ and $j = 1, \dots, Ne$, where s is the number of quadrature nodes for element, Ne is the number of elements, and $v_{h,i}^{j,k+1}$ is computed from $\mathbf{v}_{\text{ext}}^{k+1}$ by evaluating the extrapolated solution in the Gauss points. Hence

$$\mathbf{w}_i^{j,k+1} = \mathbf{w}_{\text{BDF},i}^{j,k+1} + \frac{\Delta t}{\alpha} \mathbf{F}(v_{h,i}^{j,k+1}, \mathbf{w}_{\text{ext},i}^{j,k+1}),$$

for all $i = 1, \dots, s$ and $j = 1, \dots, Ne$.

2. Given $\mathbf{w}_i^{j,k+1}$ for $i = 1, \dots, s$ and $j = 1, \dots, Ne$, the values \mathbf{v}^{k+1} and \mathbf{u}^{k+1} are computed by solving

$$\begin{aligned} c_m M \alpha \frac{\mathbf{v}^{k+1} - \mathbf{v}_{\text{BDF}}^{k+1}}{\Delta t} + K_i (\mathbf{v}^{k+1} + \mathbf{u}^{k+1}) &= \mathbf{I}_i^{s,k+1} - \chi \mathbf{I}_{ion}^{k+1} \\ K_i \mathbf{v}^{k+1} + K \mathbf{u}^{k+1} &= \mathbf{I}_i^{s,k+1} + \mathbf{I}_e^{s,k+1}, \end{aligned}$$

where \mathbf{I}_{ion}^{k+1} is computed using $\mathbf{v}_{\text{ext}}^{k+1}$ and $\mathbf{w}_i^{j,k+1}$. We remark that, by using the extrapolated transmembrane potential for the computation of the ionic current, we are linearizing the problem.

Material properties	$\sigma_l^i = 0.0023 \Omega^{-1}\text{cm}^{-1}$ $\sigma_l^e = 0.0015 \Omega^{-1}\text{cm}^{-1}$ $c_m = 1 \text{ mF cm}^{-3}$	$\sigma_t^i = 0.00024 \Omega^{-1}\text{cm}^{-1}$ $\sigma_t^e = 0.001 \Omega^{-1}\text{cm}^{-1}$
Roger-McCulloch parameters	$v_{\text{th}} = 13 \text{ mV}$ $v_p = 100 \text{ mV}$ $G = 1.5 \text{ ms}^{-1}$	$\eta_1 = 4.4 \text{ ms}^{-1}$ $\eta_2 = 0.012$ $\eta_3 = 1$

Table 4.1: Numerical values of the coefficients for the experiment on the rectangular slab, taken from [15].

4.2 Numerical simulation on simple domains: some benchmark problems

We hereby present experiments on simple geometries with the purpose of analyzing the behavior of the solution of the Bidomain equations and the properties of IGA. For the numerical integration of the two potentials and the recovery variables we considered BDF schemes of order $q = 2$ with $\Delta t = 0.05$ ms.

We remark that we use the notation P_a/C_b to denote piecewise polynomial bases of degree a with C^b -continuity across the knots. For example, P1/C0 is the basis formed by piecewise linear polynomials with C^0 -continuity across the knots, P2/C1 is the basis formed by piecewise quadratic polynomials with C^1 -continuity across the knots, and so on.

4.2.1 Wavefront propagation on a rectangular slab

As a first experiment, we follow the lines of the preliminary study that was done in [25] for the Monodomain equations. We apply a current to a rectangular domain $\Omega = (0, 16) \text{ cm} \times (0, 1) \text{ cm}$ with the purpose of generating a wavefront. We impose a current $I_i^s = 100 \text{ mA}$ for 1 ms to the stripe $(0, 0.2) \text{ cm} \times (0, 1) \text{ cm}$, and we consider $I_e^s = -I_i^s$ so that the compatibility condition $\int_{\Omega} I_i^s + I_e^s = 0$ is satisfied. As ionic membrane model we adopt the Roger-McCulloch method, presented in Section 2.2.2. We use the following definitions of $f(v, w)$ and $g(v, w)$ [15]:

$$f(v, w) = Gv \left(1 - \frac{v}{v_{\text{th}}}\right) \left(1 - \frac{v}{v_p}\right) + \eta_1 vw,$$

$$g(v, w) = \eta_2 \left(\frac{v}{v_p} - \eta_3 w\right).$$

The numerical values of the coefficients and of the tissue properties are presented in Table 4.1. We assume that the fiber direction is parallel to the x axis. The simulations were performed from $t = 0$ ms to $t = 175$ ms.

Fig. 4.2 shows the evolution of the wavefronts of v , u_i and u_e using P2/C1 basis functions. For this simulation we used 65536 square mesh elements. It appears that after around 100 ms the wavefront is fully developed; it keeps then moving with constant velocity from left to right with little variations in shape. We observe that, because of the peak value $v_p = 100 \text{ mV}$ in the Roger-McCulloch membrane model, the transmembrane potential takes values in the interval $[0, 100] \text{ mV}$, which does not correspond to the physiological range.

The wavefront velocity appears to be highly dependent on the mesh. We assume that the “true” wavefront velocity V can be computed with sufficient accuracy using P3/C2 basis functions with a mesh of 65536 elements. Using this basis, we have $V = 5.30191 \cdot 10^{-2} \text{ cm/ms}$. This value is close to e.g. the value of $5 \cdot 10^{-2} \text{ cm/ms}$ reported in [18] as typical wavefront velocity in the atria and ventricles. Fig. 4.3 shows that when the element size h is large the velocity is overestimated. For all the different bases that we considered the convergence appears to be monotone with respect to the element size. Interestingly enough, high order polynomials behave poorly when h is high and lead to worse approximations of the velocity than linear polynomials. However, under a certain threshold value of h , high order polynomials start to give better estimates than linear polynomials. Fig. 4.3 (left) could misleadingly be interpreted in the sense that the better approximation for the velocity be given by cubic polynomials with discontinuous derivatives at the interfaces (P3/C0).

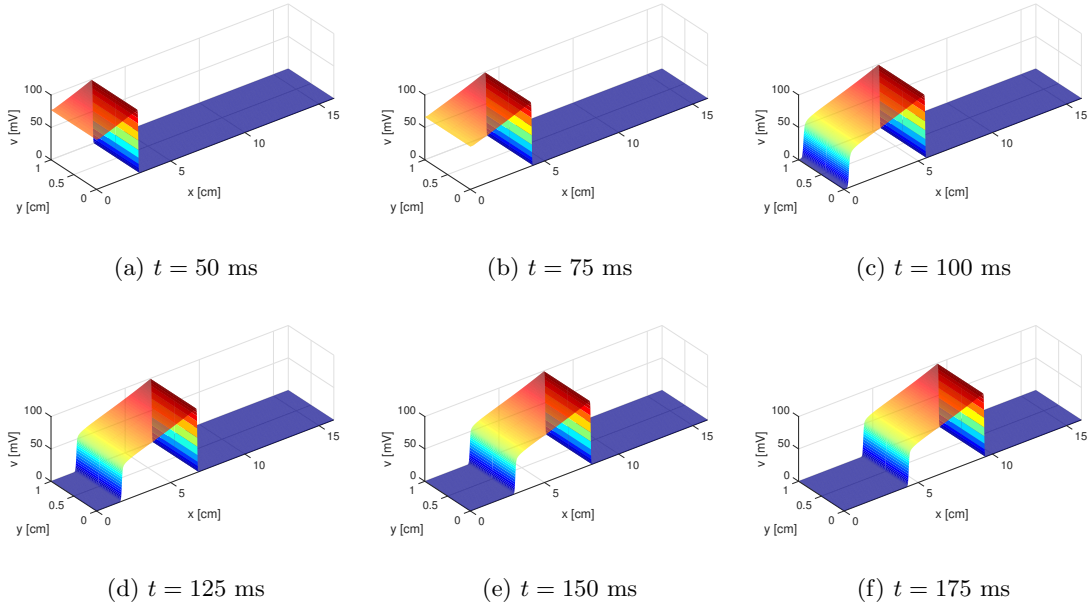


Figure 4.1: 3D representation of the traveling wavefront for the transmembrane potential v , computed using using P2/C1 basis functions and $1024 \times 64 = 65536$ elements.

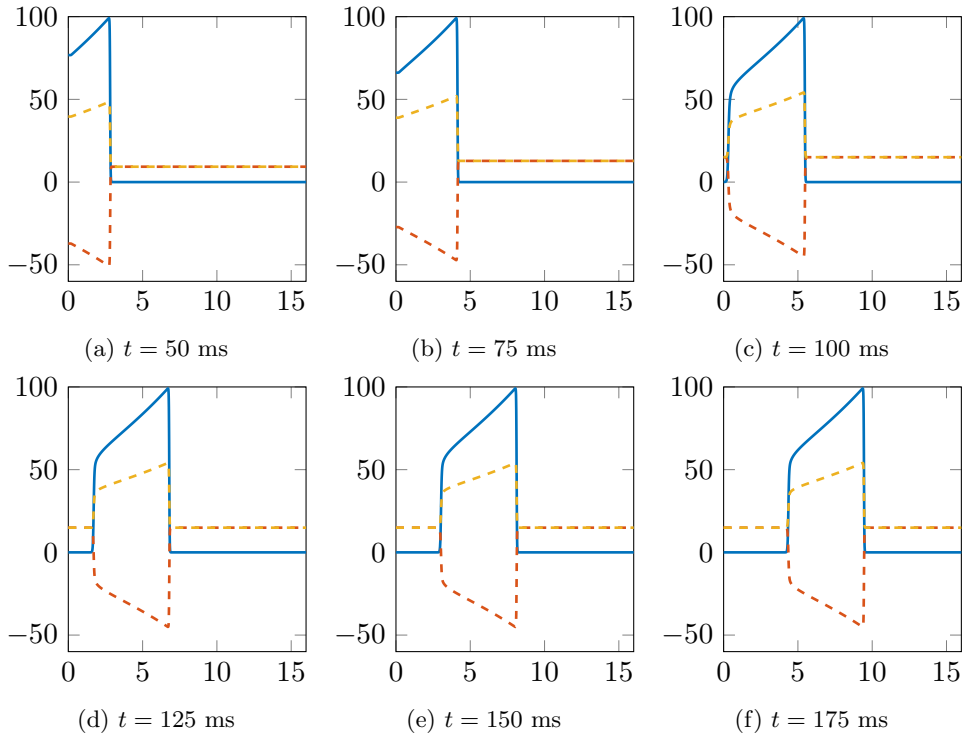


Figure 4.2: Wavefront propagation of the transmembrane potential v (blue solid line), internal potential u_i (yellow dashed line) and external potential u_e (dashed red line) in mV at different time instances, using P2/C1 basis functions and $1024 \times 64 = 65536$ elements. Lengths are expressed in cm.

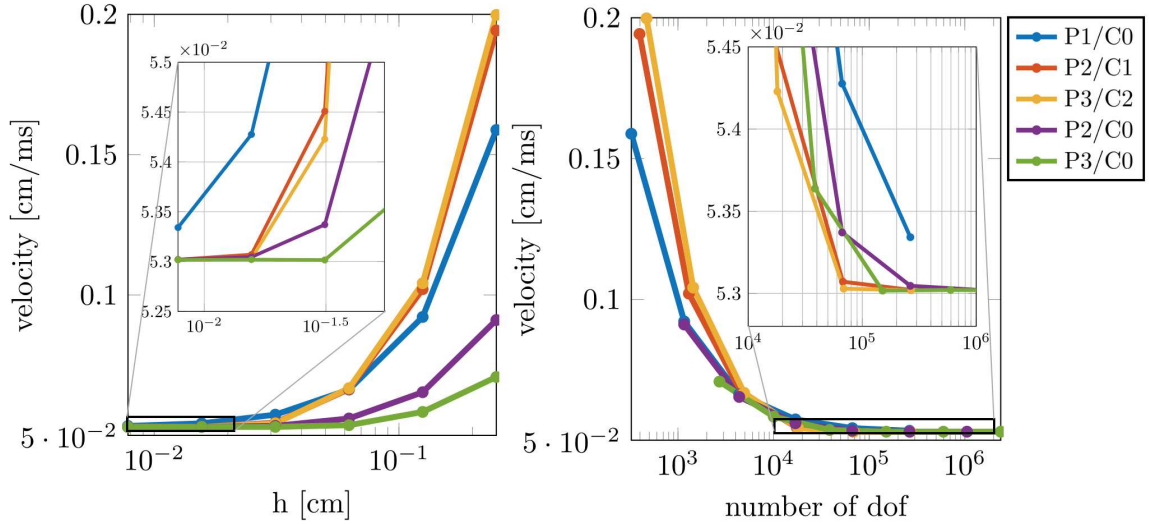


Figure 4.3: Convergence of wave velocity with respect to element size h (left) and number of degrees of freedom (right).

However, we recall that the number of degrees of freedom in NURBS-based IGA follows the rule $N_{\text{dofs}} = N_{\text{el}} + p$, where N_{el} is the number of internal elements (taking into account elements with zero length) and p is the polynomial degree. In order to generate discontinuities by keeping the number of elements the same, the multiplicity of internal nodes must be increased along each parametric direction, leading to larger numbers of degrees of freedom.

As depicted in Fig. 4.4, the number of elements also influences the width of the wave front – or in other words, the duration of the AP – which is much higher when h is large. Coarse meshes lead to faster and larger wavefronts. We observe that, when the mesh is too coarse, the solution presents oscillations in correspondence of the most critical parts of the AP, i.e. at the base and the peak of the upstroke and at the end of the repolarization. This behavior is completely due to the spatial approximation; in fact, the solutions computed with finer meshes do not present the same problematics.

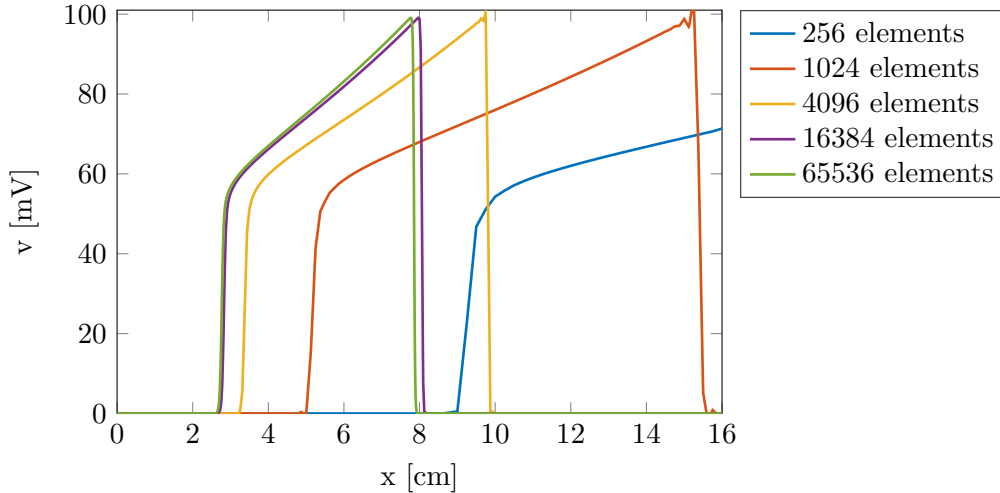


Figure 4.4: Wavefront convergence with respect to the number of mesh elements, with P2/C1 B-splines basis functions.

4.2.2 Dispersion study on a square slab

We now address the problem of wavefront propagation under the aspect of the shape of the wave. In other words, we want to study how the isogeometric approximation of the Bidomain equations affects the dispersion of the solution, similarly to what was done in [13] for the elastic wave. In order to do this, we set up a simple problem on a square $\Omega = (-4, 4) \text{ cm} \times (-4, 4) \text{ cm}$. We apply an electrical stimulus $I_i^s = 100 \text{ mA}$ on a circle of radius $r = \sqrt{2}$ centered on the origin. Since the stimulus is circular, we expect the exact solution to be circular as well. Moreover, as we expect the solution to be axis symmetric, we perform the simulation only on the upper-right quarter $(0, 4) \text{ cm} \times (0, 4) \text{ cm}$. The numerical values of the physical parameters and of the coefficients of the Roger-McCulloch model are the same as in the rectangular experiment in Section 4.2.1 except for the conductivities. In fact, since we want to understand how IGA introduces additional anisotropy to the equations, we eliminate the anisotropy given by the conductivity tensor by setting the conductivities in all directions equal to $\sigma = 0.001 \text{ } \Omega^{-1} \text{ cm}^{-1}$. For the space discretization, we consider square elements of size $h = 1.56 \cdot 10^{-2} \text{ cm}$. We remark that this choice is conditioned by the insight that we gained on the numerical solution of the equations with the experiment on the rectangular domain of Section 4.2.1: we choose an h small enough to ensure the behavior of the polynomials that we would expect – i.e. linear polynomials performing worse than quadratic and cubic polynomials with the same element size.

Fig. 4.5 shows that the solution obtained using P2/C1 basis functions exhibits indeed a circular wavefront that maintains its shape throughout the whole simulation. This is also true when different polynomials are used, as depicted in Fig. 4.6. We remark that the solution approximated using P1/C0 basis functions travels faster than the ones computed using higher order polynomials, which is consistent with what has been observed on the rectangle using elements of similar size. The computed solutions are compared to circles having radius equal to the average distance of the wavefronts to the origin of the axes r_{av} . It appears that the wavefront tends to achieve the maximum speed along the x and y axis, and minimum speed along the bisectors. This is a consequence of the type of mesh adopted, which consisted of squares with edges parallel to the domain boundaries. The dependence of the radius on the angle is also confirmed by Fig. 4.7, which shows the difference between the angular position of the wavefront and the average radius for different values of the normalized angle $\theta^* = 2\theta/\pi$. It is evident that for values of $\theta^* = 0$ and $\theta^* = 1$ the velocities reach maximum values for all the considered polynomials, while the minimum is always reached at $\theta^* = 1/2$. We notice that, in order to keep the number of degrees of freedom almost constant, the curves corresponding to discontinuous polynomials were obtained on meshes with larger element size, and this explains the larger oscillations obtained using P2/C0 and P3/C0 basis functions. As expected, higher order polynomials and higher continuity lead to smaller variations from the average radius. We also conducted experiments with larger element sizes confirming the observation we

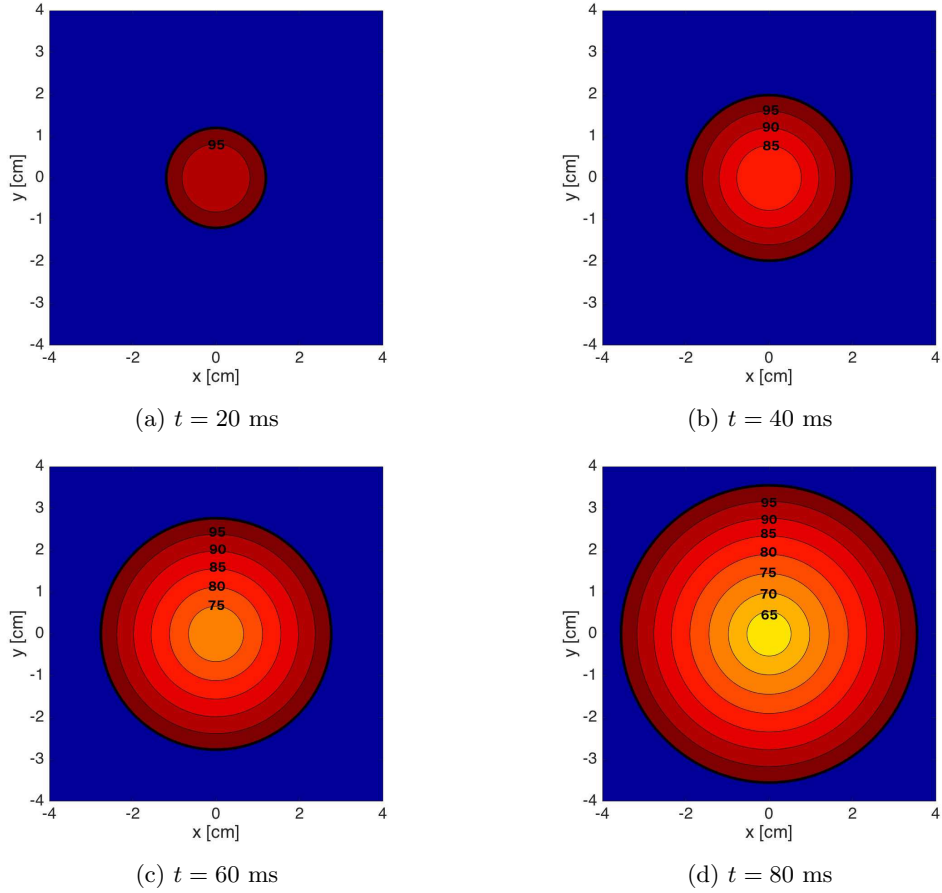


Figure 4.5: Contour map of the transmembrane potential at different time instances for the experiment on the square slab, obtained using P2/C1 basis functions. The actual simulation has been conducted on the upper right quarter; here the results are displayed by exploiting the symmetry of the solution. The tick black line separating the blue region from the red region corresponds to the excitation front.

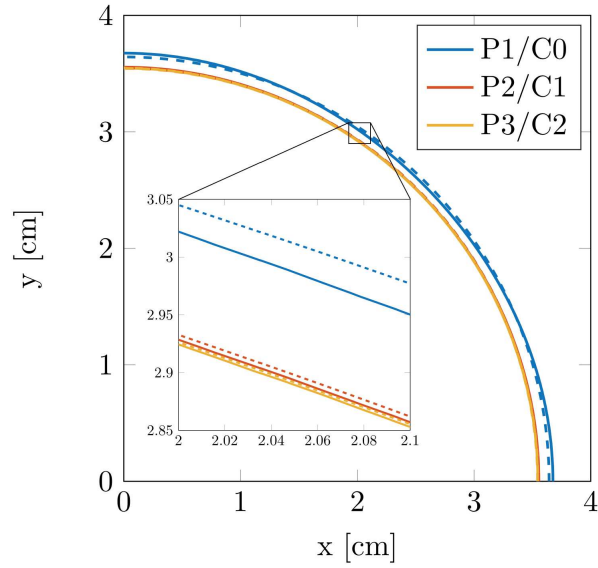


Figure 4.6: Wavefront position at time $t = 80$ ms with P1/C0, P2/C1 and P3/C2 basis functions. The dashed line corresponds to the exact circles with radius given by the average distance of the wavefront from the point (0,0), i.e. the center of the perturbation.

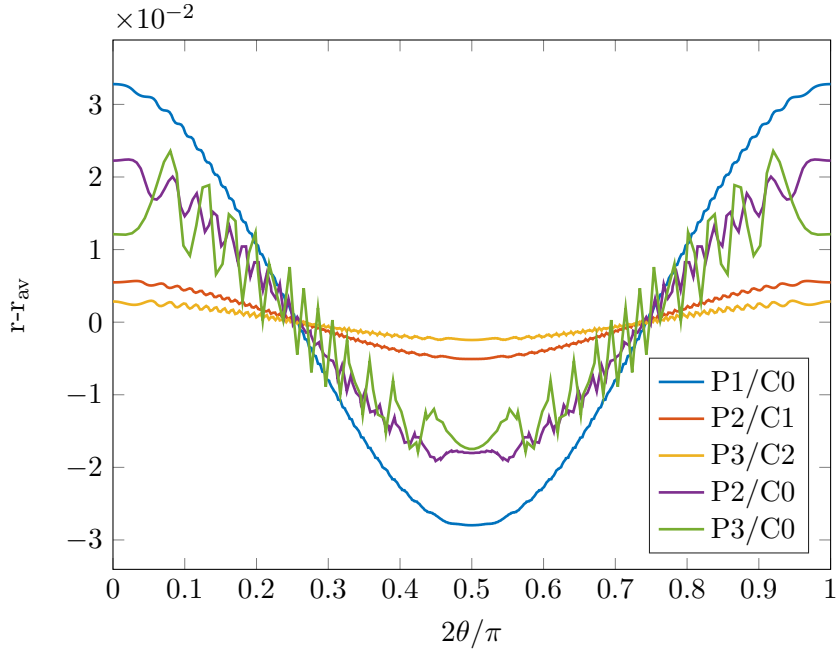


Figure 4.7: Deviation of the angular wave position from the average radius for different values of the normalized angle.

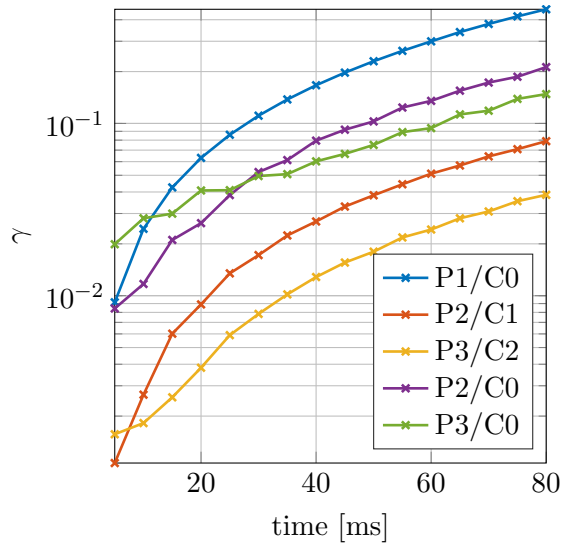


Figure 4.8: Deformation vs time for different polynomial bases.

made in Section 4.2.1: for larger element sizes linear polynomials behaved better, as they provided smaller dispersion of the wavefront.

Finally, we analyze *how fast* the shape of the wavefront changes. In order to do this, we introduce the function

$$\gamma(t) = \sqrt{\sum_{i=1}^{N_{\text{wf}}} (\mathbf{x}_{\text{wf},i}(t) - r_{\text{av}}(t))^2},$$

where $\mathbf{x}_{\text{wf},i}(t)$ for $i = 1, \dots, N_{\text{wf}}$ are points localized in correspondence of the wavefront position at time t . The function $\gamma(t)$ provides a numerical estimate of the deformation of the wavefront shape at each time. Fig. 4.8 shows the evolution of $\gamma(t)$ for different bases: we observe that high order polynomial bases ensure more circular wavefronts, but that the rate of change of the deformation – i.e. the slope of the curves – is generally independent of the regularity of the basis for large times.

Chapter 5

Numerical results on the atria

We move now to more significant applications of the Bidomain equations and we consider numerical simulations on atrial geometries using the CRN model (see Section 2.2.3). We use surface representations of the atria: this is a simplification that is motivated by the small thickness of the cardiac tissue in the upper chambers of the heart. This simplification was also used in [32] to simulate the whole electrical behavior of the heart in physiological and pathological conditions, by coupling surface representations of the atria with tridimensional meshes of the ventricles. The deformation of the atria due to the muscular contraction is not considered in this work.

As we saw in Chapter 2, the electrical stimulation of the heart starts from the sinoatrial node (SAN), that is often called the natural pacemaker of the heart because of the ability of its cells to excite themselves autonomously. The excitation generates a wavefront whose propagation in the myocardium is anisotropic because of the fibers orientation. In particular, the conduction velocity in the longitudinal direction is higher because of the high density of gap junctions. Therefore, the first step to perform realistic simulations is to create a vector field defined on the atrial geometries representing the fiber orientation. As we will see in Section 5.1, this is done by solving a Laplace problem on the atria and then identifying the fiber direction to the normalized gradient of the solution as in [29].

The electrical excitation is propagated to the LA in four specific locations of the two atria connected by muscular tissue: the Bachmann's bundle, the anterior septum, the posterior septum, and the coronary sinus musculature. We model the interaction of the two atria so that, when the excitation front reaches the location of a particular connection on the RA, a current is triggered at the corresponding connection point on the LA. For this reason, we consider the simulation of the potential on the LA as completely dependent on the potential of the RA. This assumption allows us to first consider in depth what happens on the RA when the signal is started from the SAN, and then evaluate how the signal is propagated to the LA.

In the last part of this chapter we will briefly discuss about the application of this model to the simulation of atrial fibrillation.

5.1 Fibers direction

The Bidomain equations require the definition of the fiber direction at each point of the domain $\Omega = \Omega_{RA} \cup \Omega_{LA}$. Here, we are going to arbitrarily assign a vector field to the atria by solving two separate Laplace problems, which will provide us with scalar fields defined on the surfaces, and taking the gradient of them; this approach was also followed in [29]. More precisely, let us consider the following Laplace problem on, for example, the RA:

$$\begin{cases} -\Delta u(\mathbf{x}) = f(\mathbf{x}) & \text{in } \Omega_{RA}, \\ \nabla u(\mathbf{x}) \cdot \mathbf{n} = h(\mathbf{x}) & \text{on } \partial\Omega_{RA}, \end{cases} \quad (5.1)$$

with $h(\mathbf{x}) = 0$ on $\partial\Omega_{RA}$. For start, we remark that, as noted in [31], the well-posedness of this problem is subject to the compatibility condition

$$\int_{\Omega_{RA}} f ds = - \int_{\partial\Omega_{RA}} h d\mathbf{l}.$$

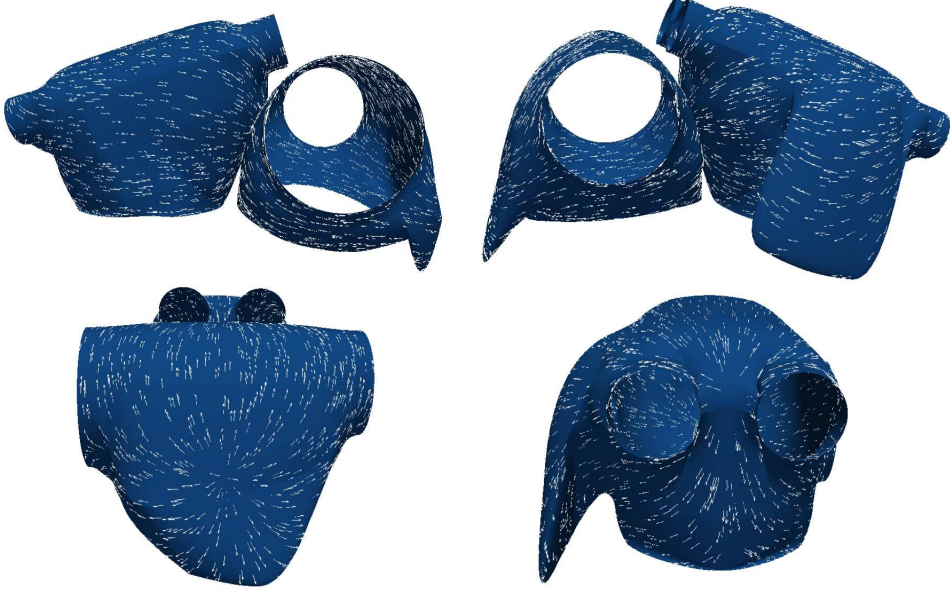


Figure 5.1: Fibers direction on the two atria.

We have to choose $f(\mathbf{x})$ so that this relation is satisfied. We choose to consider $f(\mathbf{x}) = 0$ everywhere on the domain of the RA, except in two circles of equal radius, where $f(\mathbf{x})$ is constant and takes opposite values. We remark that problem (5.1) admits actually an infinite number of solutions, because if $\tilde{u}(\mathbf{x})$ satisfies the equation, then $u_C(\mathbf{x}) = \tilde{u}(\mathbf{x}) + C$ for all $C \in \mathbb{R}$ also satisfies the equation. To ensure the uniqueness of the solution to the problem, we add the constraint of null average on the domain, i.e.

$$\frac{1}{|\Omega_{RA}|} \int_{\Omega_{RA}} u ds = 0.$$

Solving the Laplace problem on the RA and on the LA and considering the normalized gradient of the solution leads in the vector field depicted in Fig. 5.1. We point out that, because of the Neumann condition in the Laplace problem, the gradient of the solution and consequently the fibers are tangent to the boundary.

For our simulations, we consider a simplified definition of the conductivity tensor that is easily implementable given the vector field of fibers direction. We choose $\sigma_l^i = 0.0023 \Omega^{-1} \text{cm}^{-1}$, $\sigma_l^e = 0.0015 \Omega^{-1} \text{cm}^{-1}$, $\sigma_t^i = 0.00024 \Omega^{-1} \text{cm}^{-1}$ and $\sigma_t^e = 0.001 \Omega^{-1} \text{cm}^{-1}$. Then, we take

$$D_{i,e}(\mathbf{x}) = \begin{bmatrix} \sigma_t^{i,e} & 0 & 0 \\ 0 & \sigma_t^{i,e} & 0 \\ 0 & 0 & \sigma_t^{i,e} \end{bmatrix} + \begin{bmatrix} (\sigma_l^{i,e} - \sigma_t^{i,e})a_1(\mathbf{x}) & 0 & 0 \\ 0 & (\sigma_l^{i,e} - \sigma_t^{i,e})a_2(\mathbf{x}) & 0 \\ 0 & 0 & (\sigma_l^{i,e} - \sigma_t^{i,e})a_3(\mathbf{x}) \end{bmatrix},$$

where $\mathbf{a}(\mathbf{x}) = [a_1(\mathbf{x}) \ a_2(\mathbf{x}) \ a_3(\mathbf{x})]^T$ is the fiber direction in the point \mathbf{x} .

5.2 Electrophysiology on the right atrium

All the simulations presented in this chapter are performed with timestep $\Delta t = 0.01$ ms. We recall that such small timestep is needed to ensure a good approximation of the CRN solution, in particular in correspondence of the action potential upstroke. We use BDF schemes of order $q = 1$ and $q = 2$ for the integration of \mathbf{w} and v respectively. The order of the method for the recovery and concentration variables is chosen to increase its stability. Moreover, we consider $c_m = 1 \text{ mF cm}^{-3}$, $\chi = 10^3 \text{ cm}^{-1}$ the initial condition on v , gating variables and concentrations prescribed by the CRN model and reported in Table A.2.

We consider the RA geometry with 78975 elements. The atrium is stimulated in correspondence of the SAN for 1 ms with currents $I_i^s = 100 \text{ mA}$ and $I_e^s = -I_i^s$, in order to satisfy the compatibility condition (4.5); the simulation is run for 500 ms.

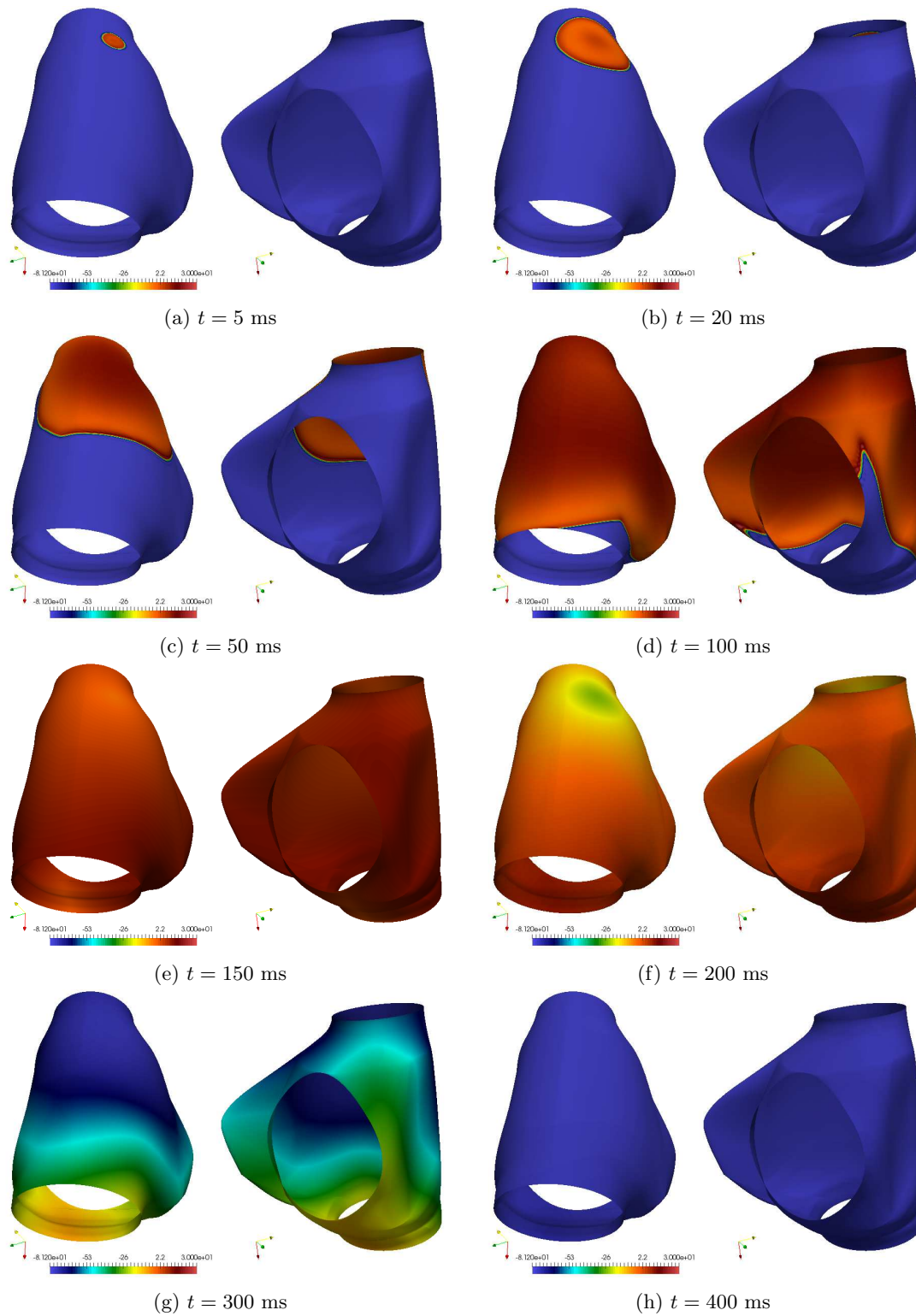


Figure 5.2: Transmembrane potential v evolution on the RA.

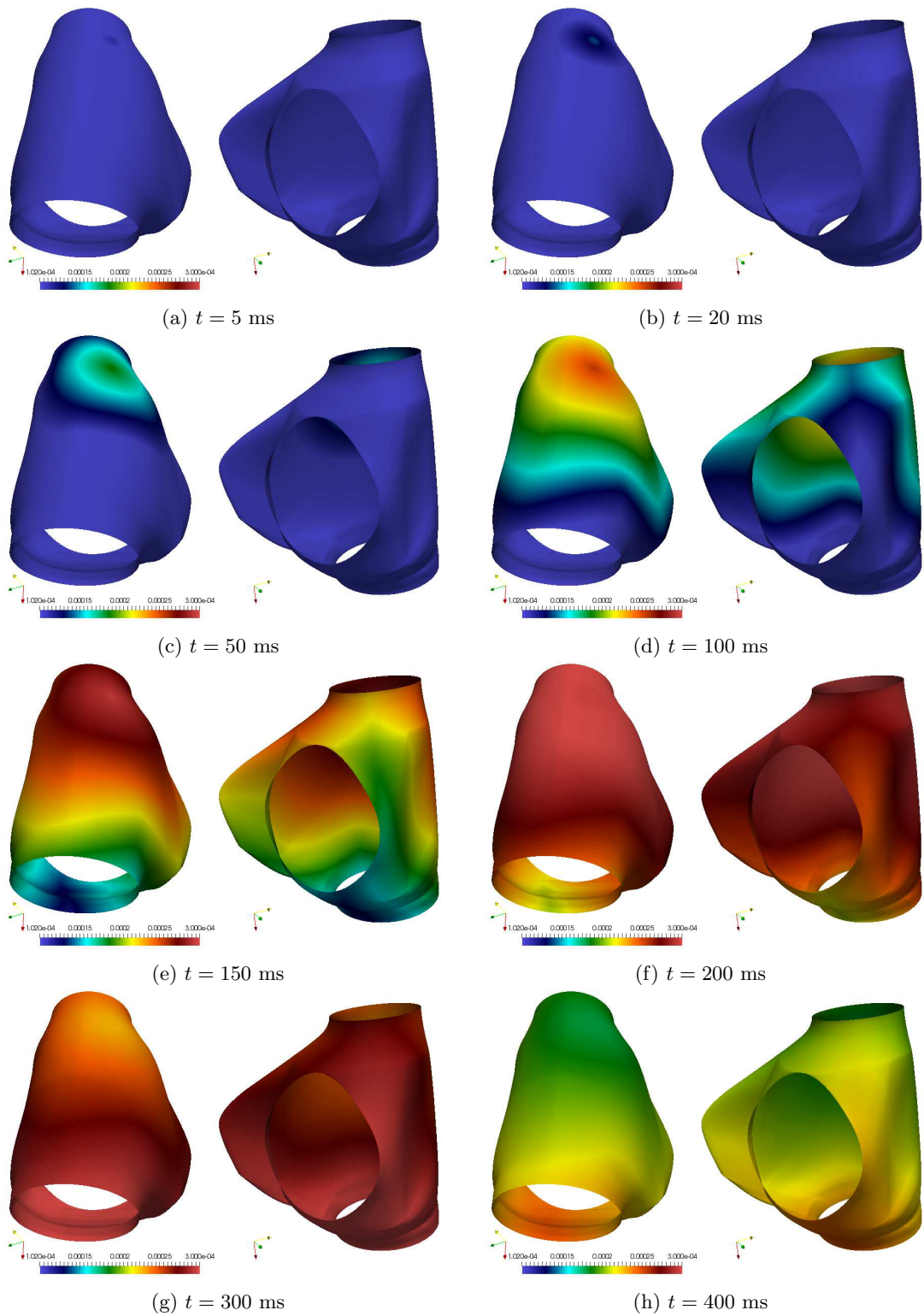


Figure 5.3: Intracellular concentration of Ca^{2+} evolution on the RA .

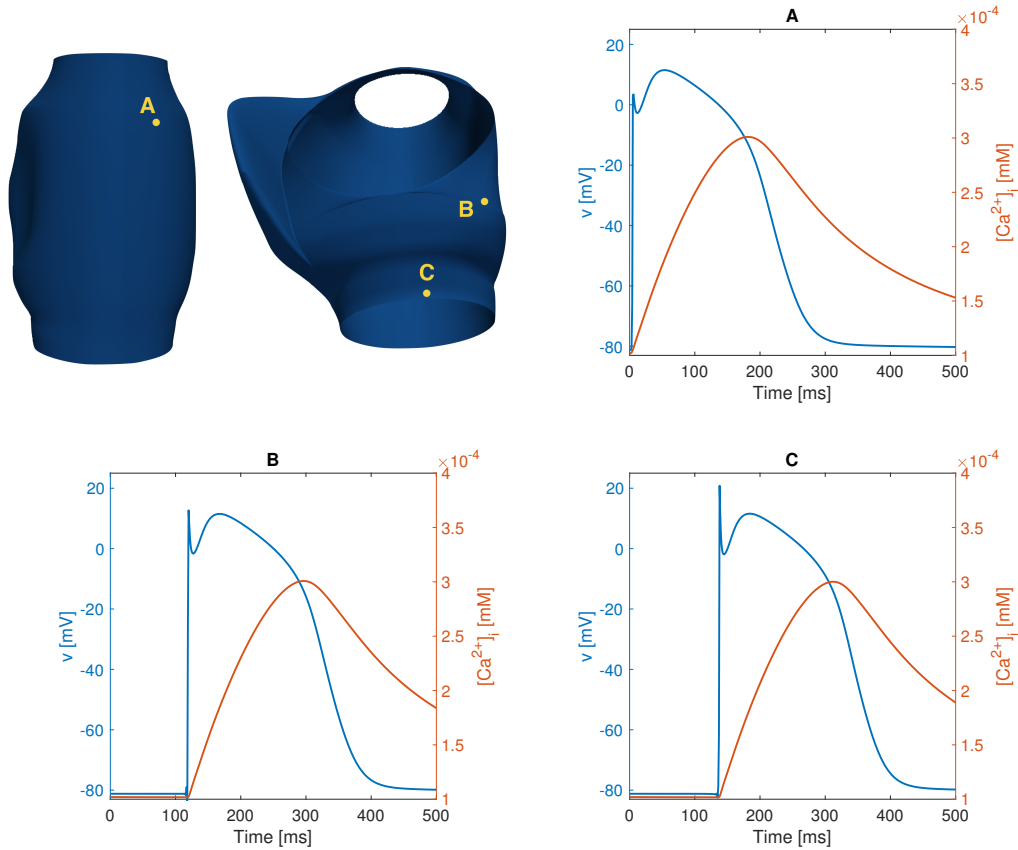


Figure 5.4: Action potential and variation of calcium concentration at a location close to the initial stimulation (A), at the AV node (B) and at the inferior vena cava (C).

Figs. 5.2 and 5.3 show the evolution of v and $[Ca^{2+}]_i$ on the RA. Fig. 5.4 shows the action potential and calcium variation registered at three specific points of the chamber. The first point is chosen to be close to the SAN, but at a distance sufficient to make the effects of the initial stimulation negligible. The second point is placed at the location of the atrioventricular (AV) node. The last point is close to the joint of the inferior vena cava, where the wavefront arrives at last. We remark that in the physiology of the heart the AV node is not stimulated by the propagating front of the myocardium but by some specific conduction channels. However, the interest in this analysis is to verify how the wave shape changes during the propagation of the front. It appears that the shape of the AP is generally preserved in the three locations; the CRN model, moreover, guarantees a considerably more realistic result if considered with the ones obtained in Chapter 4 using the Roger-McCulloch method.

We know that the element size has dramatic consequences on the wavefront velocity, thanks to the insight we got from the preliminary results on the rectangular slab in Section 4.2.1. Since the activation of the LA is subject to the timing with which the front reaches the four connection points, we aim at having a good resolution of the initial moments of the propagation. For this reason, the mesh is thinner at the top of the RA. The non homogeneous size of the mesh elements has consequences on the quality of the wavefront in certain regions of the atrium. As an example, Fig. 5.5 shows the solution at $t = 80$ ms on the auricle, which is a region with particularly coarse elements because of the way the parametrization of the surface was designed. The solution clearly exhibits oscillations similar to the ones depicted in Fig. 4.4 for the coarse meshes. However, because of the high computational cost of the simulation, it has not been possible to use sufficiently finer meshes to completely eliminate them. The effects of the spatial discretization are also visible in Fig. 5.4: we observe some oscillations immediately before the rapid depolarization of the cells in correspondence of points B and C, which are in locations where the mesh is coarser than in the top part of the atrium. Moreover, we remark that also the peak value of the transmembrane potential is subject to variations which are still due to the non homogeneous size of elements of the geometry.

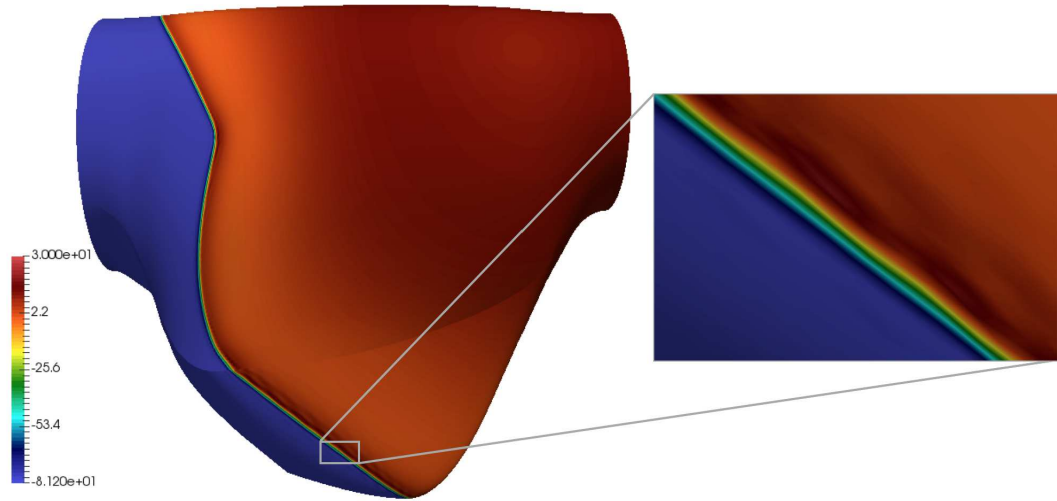


Figure 5.5: Resolution of the wavefront of the transmembrane potential on the auricle at $t = 80$ ms.

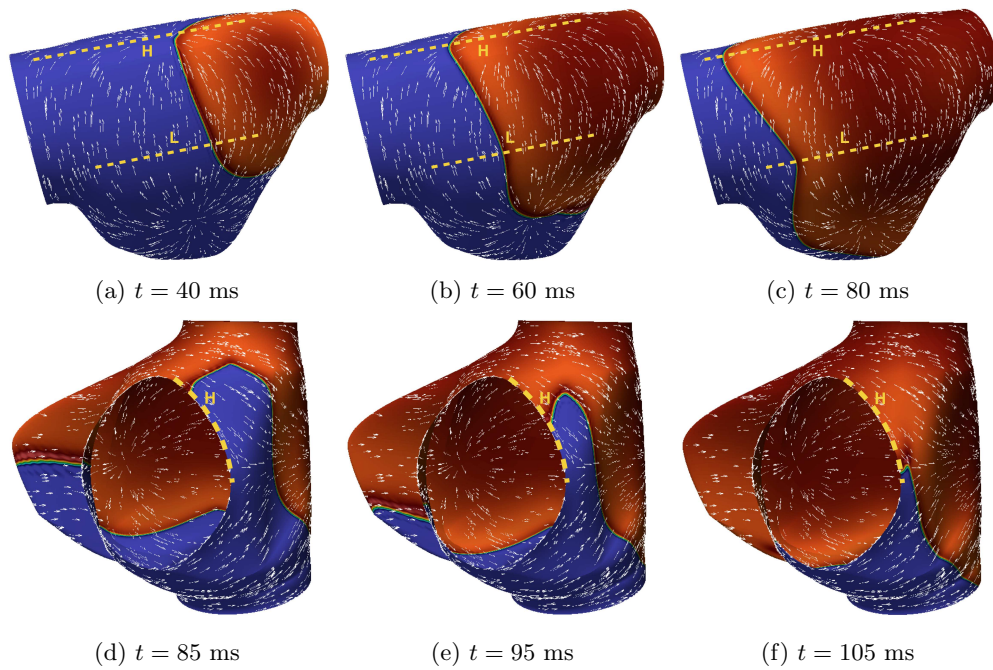


Figure 5.6: Effect of the fibers orientation on the wavefront propagation. Dashed lines refer to high velocity lines (H) and low velocity lines (L).

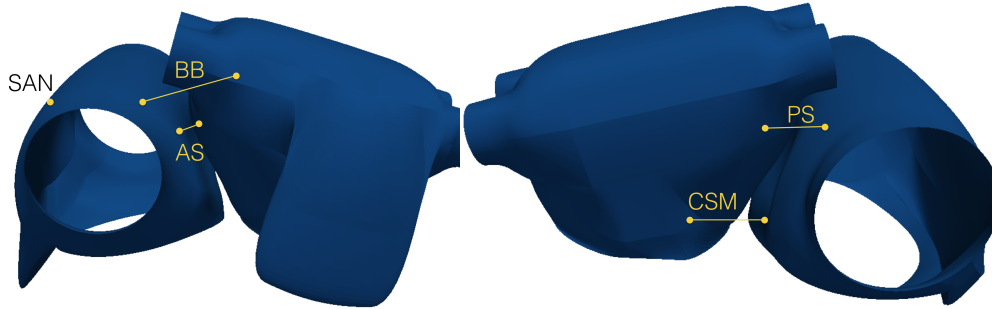


Figure 5.7: Location of the sinoatrial node (SAN) and the interatrial connections: the Bachmann's bundle (BB), the anterior septum (AS), the posterior septum (PS), and the coronary sinus musculature (CSM).

Since the calcium curve does not present sharp features, it can be appreciated how both the general shape and the peak value remain constant at the three considered points. In all of the three cases, the calcium concentration reaches the peak value of around 3×10^{-4} mM at the end of the plateau phase of the action potential.

Because of the conductivity tensor, the wavefront propagation is indeed anisotropic and the velocity of the wave depends obviously on the local orientation of the fibers and the direction of propagation. Fig. 5.6 shows examples of high velocity lines, where the wavefront propagates in the same direction of the fibers orientation, and low velocity lines, where the direction of propagation is instead transversal. We remark that, since the fibers direction is always tangential to the boundaries because of the homogeneous Neumann condition used in the Laplace problem, the excitation travels fast in correspondence of the borders of the domain, see Fig. 5.6 (bottom).

5.3 Electrophysiology on both atria

The simulation on the RA, presented in the previous section, has been used to trigger the excitation of the LA in the positions of the connection points depicted in Fig. 5.7. We referred to [30] for the approximate position of the interatrial connection on the geometries. The results of the simulation for v and $[Ca^{2+}]_i$ on both atria is shown in Fig. 5.8 and 5.9 respectively.

The geometry of the LA consists of 60742 elements. The significantly different number of elements forming the two atria is motivated by the need to have a good approximation of the wavefront in the RA region where it activates the LA. In our model the LA is segregated from the RA and the information transfer between the two is modeled via the generation of external currents. In particular, the interaction between the two atria is such that, as soon as the transmembrane potential reaches some threshold value ($v_{th} = 0$ mV in our case) in a neighborhood of the four connection points on the RA depicted in Fig. 5.7, a current of 100 mA for 1 ms is triggered in the corresponding point on the LA.

Fig. 5.10 shows the activation pattern of the LA with the time at which each contact point is activated by the RA. As in the case of the RA, we measure the action potential and variation of calcium concentration at three points (see Fig. 5.11): near the Bachmann's Bundle attachment, in correspondence of a point between the anterior septum and the posterior septum where two wavefronts meet – i.e. the wavefronts coming from the two interatrial connections, and at one of the pulmonary veins, where the excitation front arrives at last. The wavefront maintains also in this case its shape while traveling throughout the domain.

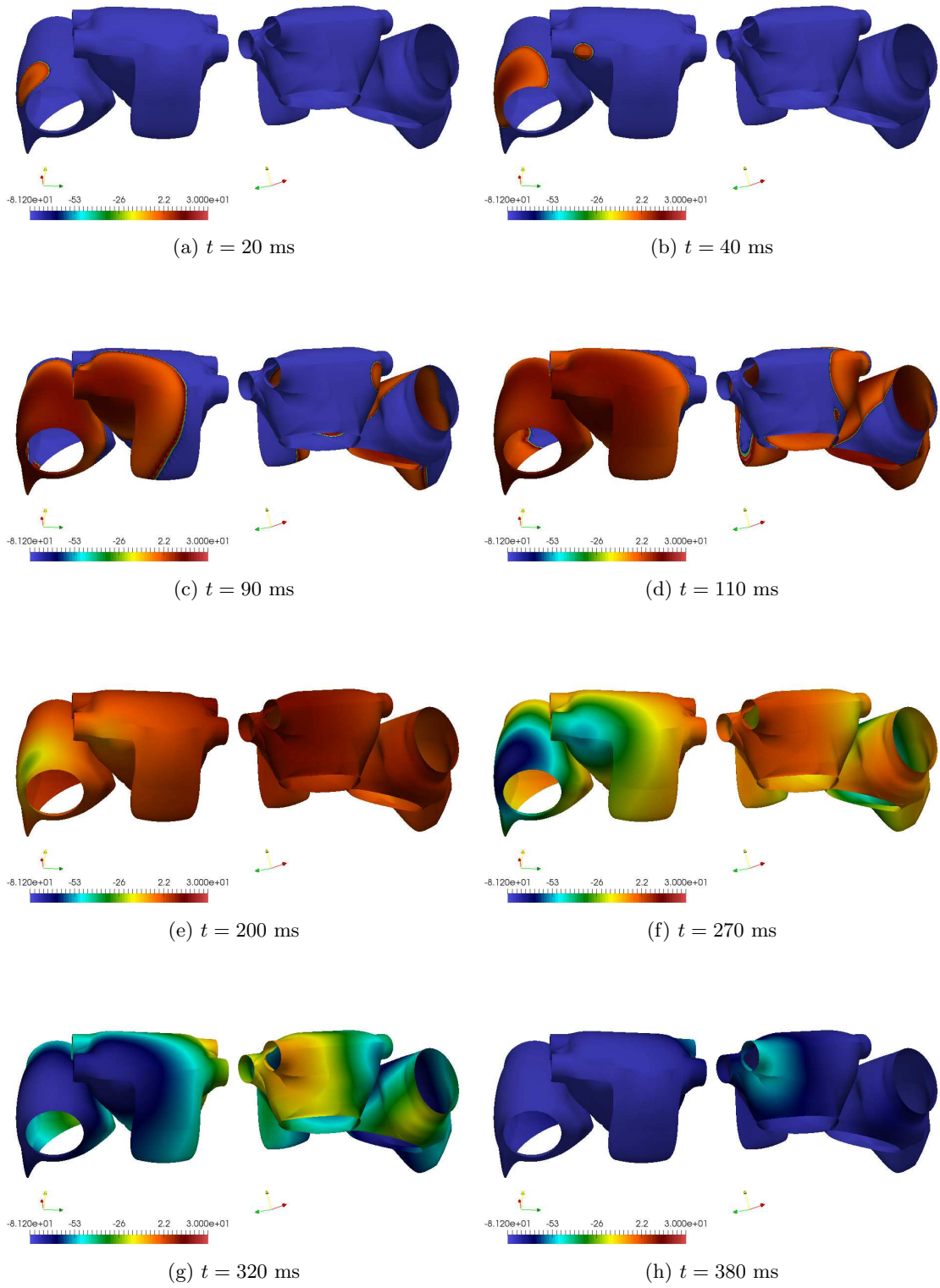


Figure 5.8: Transmembrane potential v evolution on both atria from different viewpoints.

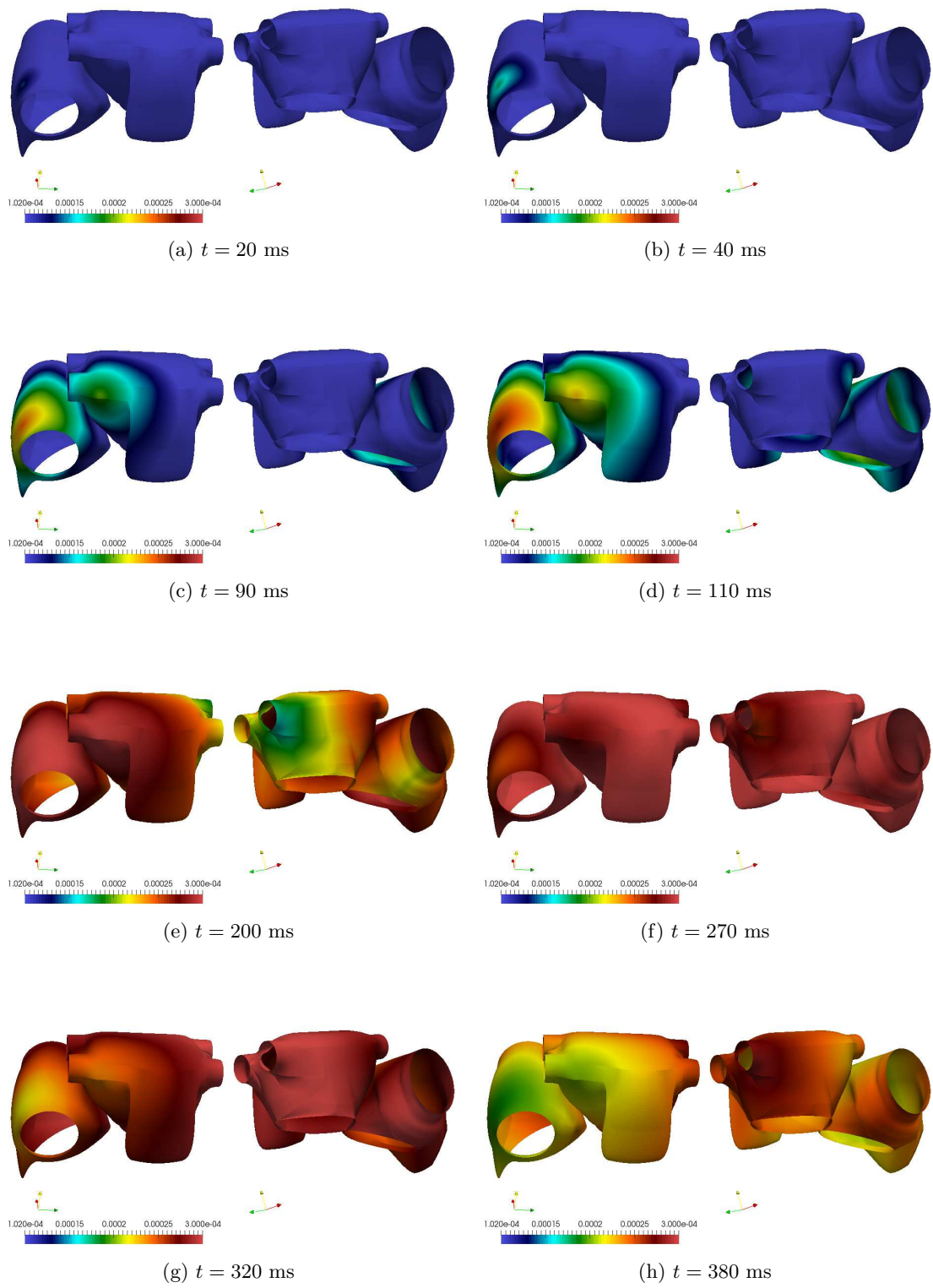


Figure 5.9: Intracellular concentration of Ca^{2+} evolution on both atria from different viewpoints.

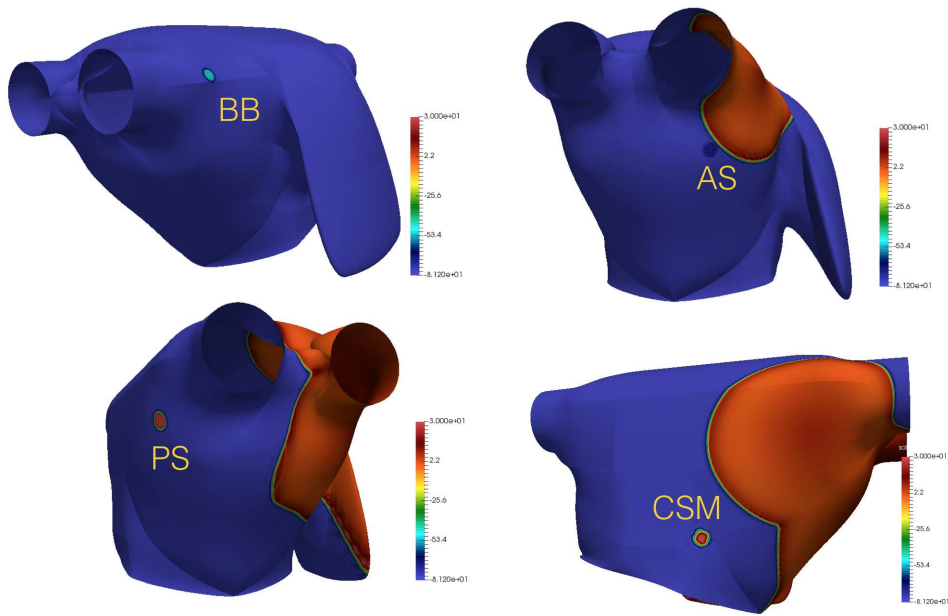


Figure 5.10: Activation pattern of the LA. The stimulation starts at $t = 34$ ms at the Bachmann's Bundle, at $t = 59$ ms at the anterior septum, at $t = 80$ ms at the posterior septum and at $t = 107$ ms at the coronary sinus musculature.

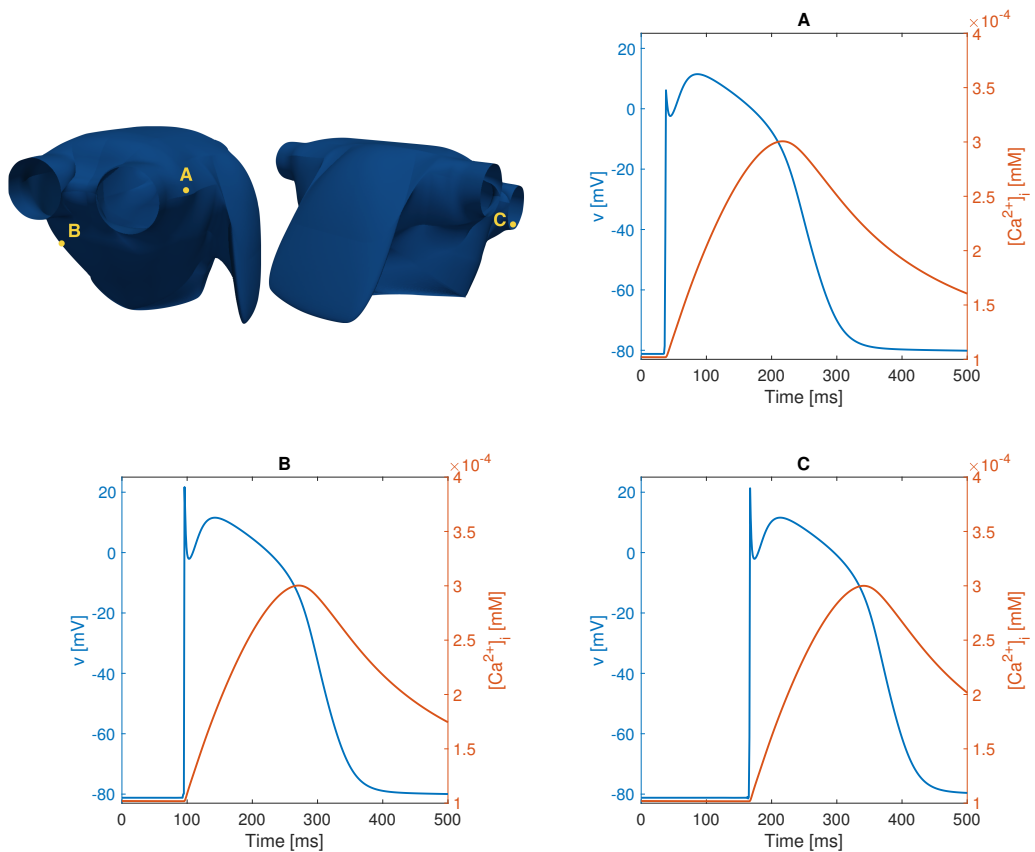


Figure 5.11: Action potential and variation of calcium concentration at a location close to the Bachmann's Bundle (A), in a point halfway between the anterior septum and the posterior septum (B) and at one of the pulmonary veins (C).

5.4 Simulating atrial fibrillation

We address the problem of simulating a pathological condition, called atrial fibrillation (AF), consisting in an irregular excitation and contraction of the two atria. During AF episodes the atrial rate of contractions reaches values of 400-600 heart beats per minute; fortunately, the AV node manages to filter the electrical signals it receives [18] leading to a rate of 100-175 beats per minute [14] in the ventricles, which is still critical but does not necessarily imply heart failures. The factors leading to AF are not completely understood. It is believed that the disorganized electrical excitation is due to signals originated not in the SAN, but probably close to the pulmonary veins on the LA [18]. This uncertainty over the physiological causes of the AF makes the reproduction of the phenomenon difficult. We identify two possible modifications to the physiological model presented earlier in this chapter:

- *Tissue parameters changes:* as noted in [17, 36], chronic AF induces changes in the physical characteristics of the tissue. These result in shorter APs and different values of the ionic currents passing through the cellular membrane.
- *Changes to the stimulation:* since the main cause of the AF seems to be the incorrect stimulation of the atria, the most intuitive way to obtain a pathological condition is to change the way the excitation is initiated. As explained in [17], there are three main strategies (initiation protocols) to trigger the AF. In the S1-S2-S3 protocol the stimulus is applied at three different locations at different times. In the burst-pacing protocol high frequency stimulations are applied to a single point. Lastly, in the ramp protocol a train of stimuli is applied to a single point, with variable cycle length – i.e. temporal distance between two consecutive stimuli.

We here present the numerical results obtained by implementing some of the changes listed above. In order to lower the computational time, we will always consider the LA geometry with 60742 elements.

5.4.1 Simulation with modified ionic model

The main idea of this simulation is the following: in the simulation on both atria, the left atrium is stimulated at four different points – the interatrial connections – at four different times, determined by the wavefront propagation on the RA. Therefore, the LA is already stimulated according to the S1-S2-S3 protocol presented above, with the only difference being the number of stimulation points (four instead of three). A possible way to induce AF is to stimulate the LA by using the information provided by the coupled simulation to synchronize the activation time of each of the connection points, and modify the ionic model such that the properties of the AP match the pathological ones. We follow [36] for the modification of the CRN model: the currents I_{to} , I_{Kur} and $I_{Ca,L}$ are decreased by 65%, 49% and 65% respectively, while I_{K1} is increased by 110%. Modifying this currents leads to an AP duration of around 200 ms.

A current of 100 mA for 1 ms is generated at $t = 0$ at the Bachmann's Bundle, at $t = 25$ ms at the anterior septum, at $t = 46$ ms at the posterior septum and at $t = 73$ ms at the coronary sinus musculature. We try to understand if some disordered behavior, like the formation of rotors [19], is exhibited when two wavefronts collide. Fig. 5.12 shows the moment of the collision of the wavefronts coming from the anterior and posterior septa together with the gradient of the transmembrane potential. It appears that the merging of the two wavefronts happens smoothly. Moreover, the gradient shows that vortexes do not form in the first times after the collision. This holds true also for the collision of the other wavefronts and for the duration of the whole simulation, which is run until $T = 500$ ms. Hence, this experiment did not lead to the insurgence of AF.

There are several possible reasons for which we did not manage to induce AF with this approach. The S1-S2-S3 protocol is highly dependent on the timing and positioning of the three stimulations: in the experiments presented in [17] the currents are located on the RA and with temporal lapse between one another of the order of hundreds of milliseconds. Moreover, the simulation are ran for several seconds; therefore, the total length of our simulation may have been too short to observe the insurgence of the arrhythmia.

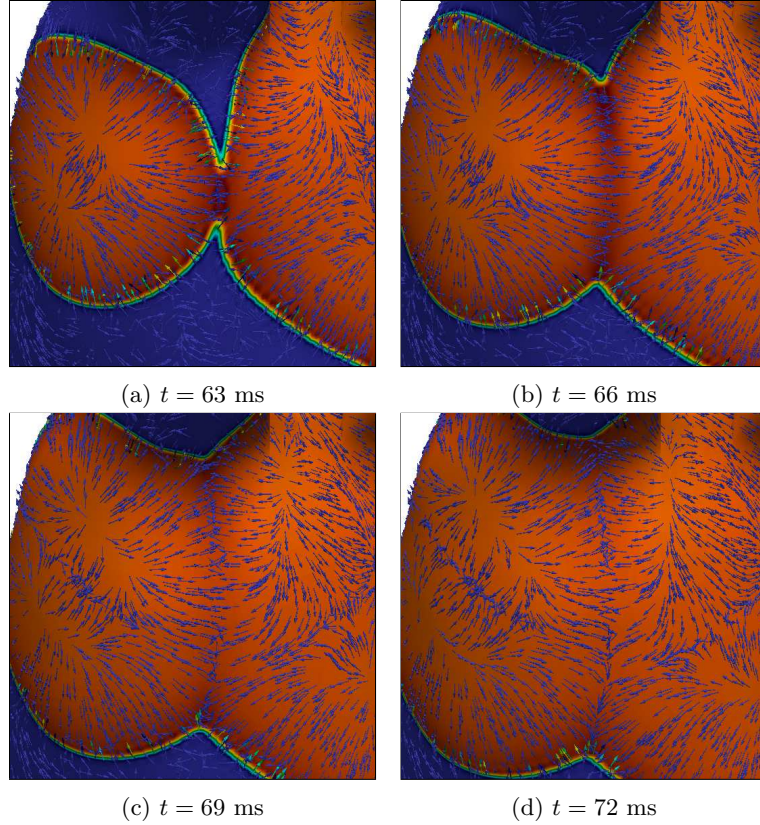


Figure 5.12: Collision of wavefronts coming from the anterior and the posterior septa. The arrows show the direction of the gradient of v .

5.4.2 Simulation with the burst-pacing protocol

For this simulation we follow the burst-pace protocol and pace the LA in correspondence of the Bachmann's Bundle at 20 Hz (the frequency of the pacing was chosen following [17]). In other words, we stimulate every 50 ms the atrium with currents of 100 mA lasting for 1 ms; the total duration of the experiment is $T = 500$ ms. We maintain the modified ionic model adopted in Section 5.4.1.

We observe that our model manages to reproduce the cellular refractory period, i.e. the period of time subsequent to the excitation of cardiac cells in which no other excitation is possible. In fact, the stimulations immediately following the first one do not reflect in the generation of new wavefronts but only in the local increase of the transmembrane potential, that reaches non-physiological values of 75 mV; see Fig. 5.13. We find that the second stimulation that generates a wavefront occurs at $t = 250$ ms, when the transmembrane potential in correspondence of the Bachmann's Bundle has reached the resting value. Interestingly enough, the third stimulation producing a wavefront occurs at $t = 400$ ms, i.e. 150 ms after the generation of the previous wavefront. This is due to the fact that, as shown in Fig. 5.14, the duration of the second AP and, consequently, the corresponding refractory period are considerably lower than the first ones.

Unfortunately, for the whole simulation we did not observe the insurgence of AF. We found evidence, however, of the shortening of the refractory period under continuous stimulation of the tissue, meaning that the properties of the wavefront change heart beat by heart beat. This could suggest that, as we supposed in Section 5.4.1, the temporal scales we are considering are not sufficient to simulate this type of arrhythmia and that it would be beneficial to extend the total duration of the experiment for several seconds.

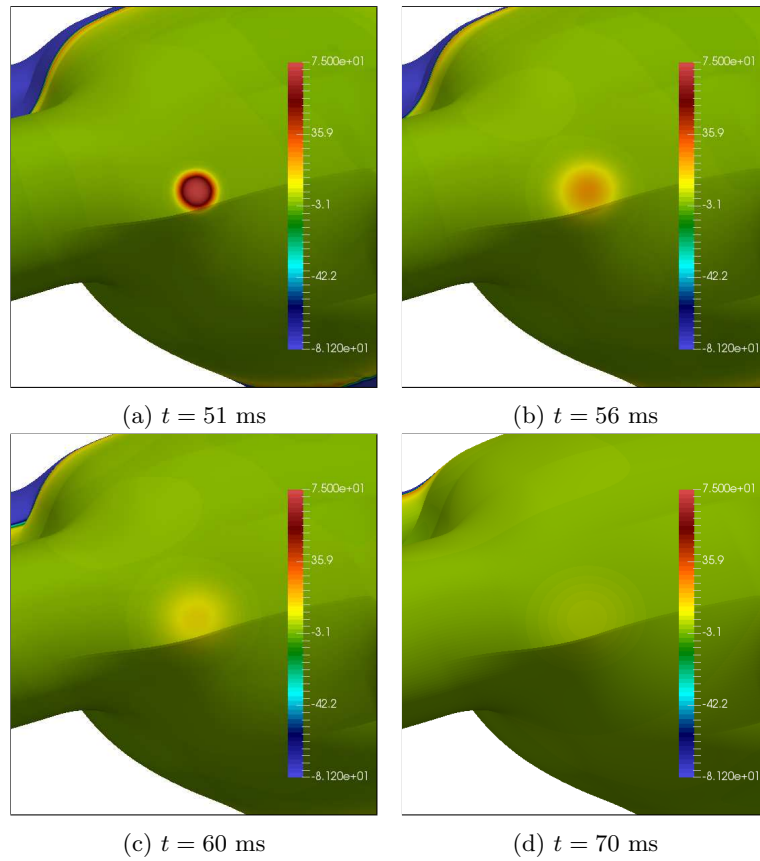


Figure 5.13: Stimulation of the Bachmann's Bundle at $t = 50$ ms in the burst-pacing experiment. The colors refer to the value of the transmembrane potential v . Since the tissue region surrounding the site is still excited and in the refractory period, such stimulus does not generate a new wavefront. We remark v reaches non physiological values of around 75 mV immediately after the stimulation.

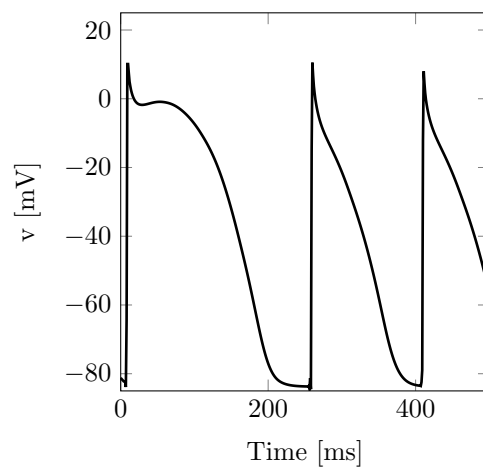


Figure 5.14: Action potential measured in the experiment regarding the burst-pacing protocol at a point close to the Bachmann's Bundle but not paced by the external stimulus.

Chapter 6

Conclusions

In this project, we aimed at the realistic simulation of the excitation front in cardiac tissue in the two atria using Isogeometric Analysis. The first step has been to setup experiments using the Bidomain model coupled with the Roger-McCulloch model – which accounts for only one gating variable – on simple domains. The purpose of these simulations has been twofold. First, they gave insights on the expected behavior of the solution of the Bidomain equations and the properties of the wavefront that is generated by electrically stimulating the tissue. Secondly, they were used to verify the convergence of IGA under the aspect of velocity of propagation and dispersion of the wavefront. In particular, we observed that coarse meshes lead to an overestimation of the velocity and the duration of the action potential. We moved then to the simulation of the equations on idealized atrial geometries generated by means of NURBS basis functions. In order to obtain a more thorough description of the cellular phenomena, we considered a complex ionic model introduced by Courtemanche, Ramirez and Nattel (CRN model) consisting of 15 gating variables and concentrations of 5 ionic species. We coupled the excitation of the right atrium with the stimulation of the left atrium yielding to realistic simulations of the propagation of the electric signal over the atria. In our model, the left atrium is electrically stimulated when the wavefront on the right counterpart reaches the location of four different points called interatrial connections. We analyzed the simulations in terms of physiological relevance and quality of the solution. We noticed that, as expected, the excitation spreads in an anisotropic fashion, which is a consequence of the different longitudinal and transversal conduction velocities in cardiac fibers. Lastly, we tried to use the Bidomain model to simulate atrial fibrillation on the left atrium. We performed two simulations in which we varied some parameters in the ionic model and the stimulation. We could not recreate the pathological conditions leading to the chaotic excitation of the atrium. However, these experiments gave us a better understanding of the properties of the Bidomain equations coupled with the CRN model, such as the shortening of the action potential and refractory period due to continuous excitation of the cardiac tissue.

Future developments

In this Master Project we obtained meaningful simulations of the electrophysiological behavior of the heart. We hereby propose some possible improvements and application of our work:

1. *Smaller elements on the atria:* the results we presented on the two atria exhibit oscillations similar to the ones we found in the experiment on the rectangle using coarse meshes. As we verified in Section 4.2.1, the main problem when solving the Bidomain equations with coarse meshes is an overestimation of the conduction velocity. Therefore, reducing the element size could significantly improve the accuracy of the solution especially under the aspect of the activation time of the two atria.
2. *Multiple heartbeats:* the CRN ionic model with standard initial conditions does not start with a stable condition, meaning that multiple excitations of the cells lead to a change in the resting values of the single variables, as shown in Fig. 2.7. Therefore, we should consider as “typical heart beat” a heart beat taking place after multiple excitations of the tissue. Moreover, as we remarked in Section 5.4, extending the overall duration of the simulation could be beneficial in simulating the atrial fibrillation.

3. *Improving the coupling the two atria:* a possible improvement could consist of using physiological data – such as typical delay in the activation times of the two atria – to get a better coupling of the two chambers.
4. *Coupling of the electrical and structural models:* the evolution of the calcium concentration provided by the ionic model could be used to determine the contraction of the heart and its deformation.
5. *Simulation of ablations:* one of the possible therapies for dealing with atrial fibrillation is the ablation of the cardiac tissue, i.e. the change of tissue properties due to burning wounds accurately caused by the surgeon. The effects of ablations could be simulated by locally setting the value of the conductivity tensor to zero [14].
6. *Simulation of the propagation of the action potential in the whole heart:* the strategy for handling the interatrial connection could be used (with little modifications) also for simulating the role of the atrioventricular node in the conduction of the signal from the right atrium to the ventricles.

Appendix A

The CRN equations

We hereby present the CRN model [10] as it is used for modeling the atrial electrophysiology in this work. We remark that, differently from what has been done in the rest of this thesis, we here denote the transmembrane potential with the capital letter V , in order to avoid ambiguities with the gating variable v . These equations differ from the ones that were first proposed in [10] for the term A_{cap} , a geometric factor taking into account the size of the cell. The term is needed to adjust the units of some of the concentration variables, and we took inspiration from the article by Luo-Rudy [21] for its computation. A_{cap} is twice the area of membrane cell that takes part to the passing of ions from the intra to the extracellular space and vice versa. In particular, it is computed as

$$A_{\text{cap}} = 2A_{\text{geo}}, \quad (\text{A.1})$$

where A_{geo} is the surface of the cell. Since the cardiac cell is assumed to be shaped as a cylinder of length $l = 100 \mu\text{m}$ and radius $r = 8 \mu\text{m}$, we have

$$A_{\text{geo}} = 2\pi r^2 + 2\pi rL = 5.428 \times 10^{-5} \text{cm}^2.$$

In the following, we present the equations of the model, consisting of the expression of each ionic current, the equilibrium potential of the species involved, and the evolution law of each of the concentrations. The evolution law of the general recovery variable is computed as follows. Let $\mathbf{y} = [y_1, \dots, y_{N_y}]^T \in \mathbb{R}^{N_y}$ be the vector of recovery variables, with $N_y = 15$. For the component y_i , the evolution equation may be written in the form

$$\begin{aligned} \frac{dy_i}{dt} &= \frac{y_{i,\infty} - y_i}{\tau_{y_i}}, \\ y_i(t=0) &= y_{i,0}, \end{aligned} \quad (\text{A.2})$$

where y_{∞} and τ_{y_i} are in general functions of V , \mathbf{y} , and the ionic currents, and $y_{i,0}$ is the initial condition. The equations are organized in groups (bullet points). Each ionic current and the coefficients for the computation of the recovery variables taking part to its computation are grouped together. The constants of the model are reported in Table A.1 and the initial conditions of each concentration and recovery variable are reported in Table A.2.

Symbol	Definition	Value
R	Gas Constant	8314.3 kJ K ⁻¹ mol ⁻¹
T	Temperature	310 K
F	Faraday constant	96486.7 C mol ⁻¹
C_m	Membrane capacitance	100 pF
V_{cell}	Cell volume	2.01×10^{-5} μL
V_i	Intracellular volume	1.3668×10^{-5} μL
A_{cap}	Capacitative membrane area	1.0856×10^{-4} cm ²
V_{up}	SR uptake compartment volume	1109.52 μm^3
V_{rel}	SR release compartment volume	96.48 μm^3
$[\text{K}^+]_o$	Extracellular K ⁺ concentration	5.4 mM
$[\text{Na}^+]_o$	Extracellular Na ⁺ concentration	140 mM
$[\text{Ca}^{2+}]_o$	Extracellular Ca ²⁺ concentration	1.8 mM
g_{Na}	Maximal I_{Na} conductance	7.8 nS pF ⁻¹
g_{K1}	Maximal I_{K1} conductance	0.09 nS pF ⁻¹
g_{to}	Maximal I_{to} conductance	0.1652 nS pF ⁻¹
g_{Kr}	Maximal I_{Kr} conductance	0.0294 nS pF ⁻¹
g_{Ks}	Maximal I_{Ks} conductance	0.129 nS pF ⁻¹
$g_{\text{Ca,L}}$	Maximal $I_{\text{Ca,L}}$ conductance	0.1238 nS pF ⁻¹
$g_{\text{b,Ca}}$	Maximal $I_{\text{b,Ca}}$ conductance	0.00113 nS pF ⁻¹
$g_{\text{b,Na}}$	Maximal $I_{\text{b,Na}}$ conductance	0.000674 nS pF ⁻¹
$I_{\text{NaK(max)}}$	Maximal I_{NaK}	0.60 pA pF ⁻¹
$I_{\text{NaCa(max)}}$	Maximal I_{NaCa}	1600 pA pF ⁻¹
$I_{\text{p,Ca(max)}}$	Maximal $I_{\text{p,Ca}}$	0.275 pA pF ⁻¹
$I_{\text{up(max)}}$	Maximal I_{up}	0.005 mM ms ⁻¹
K_{Q10}	Temperature scaling factor for I_{Kur} and I_{to} kinetics	3
γ	Voltage dependence parameter for $I_{\text{Na,Ca}}$	0.35
$K_{\text{m,Na(i)}}$	$[\text{Na}^+]_i$ half-saturation constant for I_{NaK}	10 mM
$K_{\text{m,K(o)}}$	$[\text{K}^+]_o$ half-saturation constant for I_{NaK}	1.5 mM
$K_{\text{m,Na}}$	$[\text{Na}^+]_o$ half-saturation constant for I_{NaCa}	87.5 mM
k_{sat}	Saturation factor for I_{NaCa}	0.1
k_{rel}	Maximal release rate for I_{rel}	30 ms ⁻¹
k_{up}	$[\text{Ca}^{2+}]_i$ half-saturation constant for I_{up}	0.00092 mM
$[\text{Ca}^{2+}]_{\text{up(max)}}$	Maximal Ca ²⁺ concentration in uptake compartment	15 mM
$[\text{Cmdn}]_{\text{max}}$	Total calmodulin concentration in myoplasm	0.05 mM
$[\text{Trpn}]_{\text{max}}$	Total troponin concentration in myoplasm	0.07 mM
$[\text{Csqn}]_{\text{max}}$	Total calsequestrin concentraion in SR release compartment	10 mM
$K_{\text{m,Cmdn}}$	$[\text{Ca}^{2+}]_i$ half-saturation constant for calmodulin	0.00238 mM
$K_{\text{m,Trpn}}$	$[\text{Ca}^{2+}]_i$ half saturation constant for troponin	0.0005 mM
$K_{\text{m,Csqn}}$	$[\text{Ca}^{2+}]_{\text{rel}}$ half-saturation constant for I_{up}	0.8 mM

Table A.1: Parameters for the CRN model. All of them are taken from [10], except for A_{cap} , which was computed using (A.1).

Variable	Initial value
V	-81.2 mV
h	0.965
d	1.37×10^{-4}
x_r	3.29×10^{-5}
$[\text{Na}^+]_i$	11.2 mM
$[\text{K}^+]_i$	139 mM
$[\text{Ca}^{2+}]_{\text{rel}}$	1.49 mM
o_i	0.999
u_i	0.999
v	1.00
m	2.91×10^{-3}
j	0.978
f	0.999
x_s	1.87×10^{-2}
$[\text{Ca}^{2+}]_i$	1.02×10^{-4} mM
$[\text{Ca}^{2+}]_{\text{up}}$	1.49 mM
o_a	3.04×10^{-2}
u_a	4.96×10^{-3}
f_{Ca}	7.75×10^{-1}
u	0
w	0.999

Table A.2: Initial values for the CRN model, taken from [10].

- *Ionic current:*

$$I_{ion} = I_{\text{Na}} + I_{\text{K1}} + I_{\text{to}} + I_{\text{Kur}} + I_{\text{Kr}} + I_{\text{Ks}} + I_{\text{Ca,L}} + I_{\text{p,Ca}} + I_{\text{NaK}} + I_{\text{NaCa}} + I_{\text{b,Na}} + I_{\text{b,Ca}}.$$

- *Equilibrium potential:*

$$E_X = \frac{RT}{zF} \log \frac{[X]_o}{[X]_i},$$

where X is either Na^+ , K^+ , Ca^{2+} and z is the corresponding valence ($z = 1$ for Na^+ and K^+ , $z = 2$ for Ca^{2+}).

- *Transmembrane potential:*

$$\frac{dV}{dt} = -\frac{I_{ion} + I_{app}}{C_m},$$

where I_{app} is the external applied current.

- *Concentrations:*

$$\begin{aligned}
\frac{d[\text{Na}^+]_i}{dt} &= A_{\text{cap}} \frac{-3I_{\text{NaK}} - 3I_{\text{NaCa}} - I_{\text{b,Na}} - I_{\text{Na}}}{FV_i}, \\
\frac{d[\text{K}^+]_i}{dt} &= A_{\text{cap}} \frac{2I_{\text{NaK}} - I_{\text{K1}} - I_{\text{to}} - I_{\text{Kur}} - I_{\text{Kr}} - I_{\text{Ks}} - I_{\text{b,K}}}{FV_i}, \\
B_1 &= A_{\text{cap}} \frac{2I_{\text{NaCa}} - I_{\text{p,Ca}} - I_{\text{Ca,L}} - I_{\text{b,Ca}}}{2FV_i} + \frac{V_{\text{up}}(I_{\text{up,leak}} - I_{\text{up}}) + I_{\text{rel}}V_{\text{rel}}}{V_i}, \\
B_2 &= 1 + \frac{[\text{Trpn}]_{\text{max}}K_{\text{m,Trpn}}}{([\text{Ca}^{2+}]_i + K_{\text{m,Trpn}})^2} + \frac{[\text{Cmdn}]_{\text{max}}K_{\text{m,Cmdn}}}{([\text{Ca}^{2+}]_i + K_{\text{m,Cmdn}})^2}, \\
\frac{d[\text{Ca}^{2+}]_i}{dt} &= \frac{B_1}{B_2}, \\
\frac{d[\text{Ca}^{2+}]_{\text{up}}}{dt} &= I_{\text{up}} - I_{\text{up,leak}} - I_{\text{tr}} \frac{V_{\text{rel}}}{V_{\text{up}}}, \\
\frac{d[\text{Ca}^{2+}]_{\text{rel}}}{dt} &= \frac{(I_{\text{tr}} - I_{\text{rel}})}{1 + \frac{[\text{Csqn}]_{\text{max}}K_{\text{m,Csqn}}}{([\text{Ca}^{2+}]_{\text{rel}} + K_{\text{m,Csqn}})^2}}.
\end{aligned}$$

- *Fast Na^+ current:*

$$I_{\text{Na}} = g_{\text{Na}}m^3hj(V - E_{\text{Na}}),$$

where m , h and j are recovery variables following (A.2) with

$$\begin{aligned}
&\left. \begin{aligned} \tau_x &= (\alpha_x + \beta_x)^{-1} \\ x_\infty &= \alpha_x \tau_x \end{aligned} \right\} \text{for } x = m, h, j, \\
\alpha_m &= \begin{cases} 0.32 \frac{V + 47.13}{1 - \exp(-0.1(V + 47.13))} & \text{if } V \neq -47.13 \\ 3.2 & \text{if } V = -47.13 \end{cases}, \\
\beta_m &= 0.08 \exp(-V/11), \\
\alpha_h &= \begin{cases} 0.135 \exp\left(-\frac{V + 80}{6.8}\right) & \text{if } V < -40 \\ 0 & \text{if } V \geq -40. \end{cases} \\
\beta_h &= \begin{cases} \frac{3.56 \exp(0.079V) + 3.1 \times 10^5 \exp(0.35V)}{1} & \text{if } V < -40 \\ 0.13 \left(1 + \exp\left(-\frac{V + 10.66}{11.1}\right)\right) & \text{if } V \geq -40 \end{cases} \\
\alpha_j &= \begin{cases} \frac{(-127140 \exp(0.2444V) - 3.474 \times 10^{-5} \exp(-0.04391V))(V + 37.78)}{1 + \exp(0.311(V + 79.23))} & \text{if } V < -40 \\ 0 & \text{if } V \geq -40 \end{cases} \\
\beta_j &= \begin{cases} 0.1212 \frac{\exp(-0.01052V)}{1 + \exp(-0.1378(V + 40.14))} & \text{if } V < -40 \\ 0.3 \frac{\exp(-2.535 \times 10^{-7}V)}{1 + \exp(-0.1(V + 32))} & \text{if } V \geq -40 \end{cases}.
\end{aligned}$$

- *Time-Independent K^+ current:*

$$I_{\text{K1}} = \frac{g_{\text{K1}}(V - E_{\text{K}})}{1 + \exp(0.07(V + 80))}.$$

- *Transient Outward K^+ current:*

$$I_{\text{to}} = g_{\text{to}}o_a^3o_i(V - E_{\text{K}}),$$

where o_a and o_i are recovery variables following (A.2) with

$$\begin{aligned}\tau_x &= (\alpha_x + \beta_x)^{-1}/K_{Q10} \quad \text{for } x = o_a, o_i, \\ \alpha_{o_a} &= \frac{0.65}{\exp\left(-\frac{V+10}{8.5}\right) + \exp\left(-\frac{V-30}{59.0}\right)}, \quad \beta_{o_a} = \frac{0.65}{2.5 + \exp\left(\frac{V+82}{17.0}\right)}, \\ \alpha_{o_i} &= \frac{1}{18.53 + \exp\left(\frac{V+113.7}{10.95}\right)}, \quad \beta_{o_i} = \frac{1}{35.56 + \exp\left(-\frac{V+1.26}{7.44}\right)}, \\ o_{a,\infty} &= \frac{1}{1 + \exp\left(-\frac{V+20.47}{17.54}\right)}, \quad o_{i,\infty} = \frac{1}{\exp\left(\frac{V+43.1}{5.3}\right)}.\end{aligned}$$

- *Ultrarapid Delayed Rectifier K^+ current:*

$$I_{Kur} = g_{Kur} u_a^3 u_i (V - E_K),$$

where u_a and u_i are recovery variables following (A.2) with

$$\begin{aligned}\tau_x &= (\alpha_x + \beta_x)^{-1}/K_{Q10} \quad \text{for } x = u_a, u_i, \\ \alpha_{u_a} &= \frac{0.65}{\exp\left(-\frac{v+10}{8.5}\right) + \exp\left(-\frac{V-30}{59.0}\right)}, \quad \beta_{u_a} = \frac{0.65}{2.5 + \exp\left(\frac{V+82}{17.0}\right)}, \\ \alpha_{u_i} &= \frac{1}{21 + \exp\left(-\frac{V-185}{28}\right)}, \quad \beta_{u_i} = \exp\left(\frac{V-158}{16}\right), \\ u_{a,\infty} &= \frac{1}{1 + \exp\left(-\frac{V+30.3}{9.6}\right)}, \quad u_{i,\infty} = \frac{1}{1 + \exp\left(\frac{V-99.45}{27.48}\right)},\end{aligned}$$

and

$$g_{Kur} = 0.005 + \frac{0.05}{1 + \exp\left(-\frac{V-15}{13}\right)}.$$

- *Rapid Delayed Outward Rectifier K^+ current:*

$$I_{Kr} = \frac{g_{Kr} x_r (V - E_K)}{1 + \exp\left(\frac{V+15}{22.4}\right)},$$

where x_r is a recovery variable following (A.2) with

$$\begin{aligned}\tau_{x_r} &= (\alpha_{x_r} + \beta_{x_r})^{-1}, \quad x_{r,\infty} = \frac{1}{1 + \exp\left(-\frac{V+14.1}{6.5}\right)}, \\ \alpha_{x_r} &= 0.0003 \frac{V+14.1}{1 - \exp\left(-\frac{V+14.1}{5}\right)}, \quad \beta_{x_r} = 7.3898 \times 10^{-5} \frac{V-3.3328}{\exp\left(\frac{V-3.3328}{5.1237}\right) - 1}.\end{aligned}$$

- *Slow Delayed Outward Rectifier K^+ current:*

$$I_{Ks} = g_{Ks} x_s^2 (V - E_K),$$

where x_s is a recovery variable following (A.2) with

$$\begin{aligned}\tau_{x_s} &= 0.5(\alpha_{x_s} + \beta_{x_s})^{-1}, \quad x_{s,\infty} = \frac{1}{\sqrt{1 + \exp\left(-\frac{V-19.9}{12.7}\right)}}, \\ \alpha_{x_s} &= 4 \times 10^{-5} \frac{V-19.9}{1 - \exp\left(-\frac{V-19.9}{17}\right)}, \quad \beta_{x_s} = 3.5 \times 10^{-5} \frac{V-19.9}{\exp\left(\frac{V-19.9}{9}\right) - 1}.\end{aligned}$$

- *L-Type Ca^{2+} current:*

$$I_{Ca,L} = g_{Ca,L} d f f_{Ca} (V - 65),$$

where d , f and f_{Ca} are recovery variables following (A.2) with

$$\begin{aligned} \tau_d &= \frac{1 - \exp\left(-\frac{V+10}{6.24}\right)}{0.035(V+10)\left(1 + \exp\left(-\frac{V+10}{6.24}\right)\right)}, & d_\infty &= \frac{1}{1 + \exp\left(-\frac{V+10}{8}\right)}, \\ \tau_f &= \frac{9}{0.0197 \exp(-0.0337^2(V+10)^2) + 0.02}, & f_\infty &= \frac{1}{1 + \exp\left(\frac{V+28}{6.9}\right)}, \\ \tau_{f_{Ca}} &= 2, & f_{Ca,\infty} &= \frac{1}{1 + \frac{[Ca^{2+}]_i}{0.00035}}. \end{aligned}$$

- *$Na^+ - K^+$ Pump current:*

$$I_{NaK} = I_{NaK(\max)} f_{NaK} \frac{1}{1 + \sqrt{\left(\frac{K_{m,Na(i)}}{[Na^+]_i}\right)^3 [K^+]_o + K_{m,K(o)}}} \frac{[K^+]_o}{[K^+]_o + K_{m,K(o)}},$$

where

$$f_{NaK} = \frac{1}{1 + 0.1245 \exp\left(-0.1 \frac{FV}{RT}\right) + \sigma 0.0365 \exp\left(-\frac{FV}{RT}\right)}, \quad \sigma = \left(\exp\left(\frac{[Na^+]_o}{67.3} - 1\right)\right) / 7.$$

- *$Na^+ - Ca^{2+}$ Exchanger current:*

$$I_{Na,Ca} = \frac{C_1}{C_2},$$

where

$$\begin{aligned} C_1 &= I_{NaCa(\max)} \left(\exp\left(\frac{\gamma FV}{RT}\right) [Na^+]_i^3 [Ca^{2+}]_o - \exp\left(\frac{(\gamma-1)FV}{RT}\right) [Na^+]_o^3 [Ca^{2+}]_i \right), \\ C_2 &= (K_{m,Na}^3 + [Na^+]_o^3)(K_{m,Ca} + [Ca^{2+}]_o) \left(1 + k_{sat} \exp\left(\frac{(\gamma-1)FV}{RT}\right) \right). \end{aligned}$$

- *Background currents:*

$$\begin{aligned} I_{b,Ca} &= g_{b,Ca}(V - E_{Ca}), \\ I_{b,Na} &= g_{b,Na}(V - E_{Na}). \end{aligned}$$

- *Ca^{2+} Pump current:*

$$I_{p,Ca} = I_{p,Ca(\max)} \frac{[Ca^{2+}]_i}{0.0005 + [Ca^{2+}]_i}.$$

- *Ca^{2+} Release current from JSR:*

$$I_{rel} = k_{rel} u^2 v w ([Ca^{2+}]_{rel} - [Ca^{2+}]_i),$$

where u , v and w are recovery variables following (A.2) with

$$\tau_u = 8.0, \quad u_\infty = \frac{1}{1 + \exp\left(-\frac{F_n - 3.4175 \times 10^{-13}}{13.67 \times 10^{-16}}\right)},$$

$$\tau_v = 1.91 + \frac{2.09}{1 + \exp\left(-\frac{F_n - 3.4175 \times 10^{-13}}{13.67 \times 10^{-16}}\right)}, \quad v_\infty = 1 - \frac{1}{1 + \exp\left(-\frac{F_n - 6.835 \times 10^{-14}}{13.67 \times 10^{-16}}\right)},$$

$$\tau_w = 6.0 \frac{1 - \exp\left(-\frac{V - 7.9}{5}\right)}{\left(1 + 0.3 \exp\left(-\frac{V - 7.9}{5}\right)\right)(V - 7.9)}, \quad w_\infty = 1 - \frac{1}{1 + \exp\left(-\frac{V - 40}{17}\right)},$$

$$F_n = 10^{-12} V_{\text{rel}} I_{\text{rel}} - \frac{5 \times 10^{-13}}{F} (I_{\text{Ca,L}}/2 - I_{\text{NaCa}}/5).$$

- *Transfer current from NSR to JSR:*

$$I_{\text{tr}} = \frac{[\text{Ca}^{2+}]_{\text{up}} - [\text{Ca}^{2+}]_{\text{rel}}}{180}.$$

- *Ca^{2+} Uptake current by the NSR:*

$$I_{\text{up}} = \frac{I_{\text{up(max)}}}{1 + \frac{K_{\text{up}}}{[\text{Ca}^{2+}]_i}}.$$

- *Ca^{2+} Leak current by the NSR:*

$$I_{\text{up,leak}} = \frac{[\text{Ca}^{2+}]_{\text{up}}}{[\text{Ca}^{2+}]_{\text{up(max)}}} I_{\text{up(max)}}.$$

Bibliography

- [1] Rubin R. Aliev and Alexander V. Panfilov. A simple two-variable model of cardiac excitation. *Chaos, Solitons & Fractals*, 7(3):293–301, 1996.
- [2] Yuri Bazilevs, L. Beirao da Veiga, J. Austin Cottrell, Thomas J.R. Hughes, and Giancarlo Sangalli. Isogeometric analysis: approximation, stability and error estimates for h-refined meshes. *Mathematical Models and Methods in Applied Sciences*, 16(07):1031–1090, 2006.
- [3] Yves Bourgault, Yves Coudiere, and Charles Pierre. Existence and uniqueness of the solution for the bidomain model used in cardiac electrophysiology. *Nonlinear Analysis: Real World Applications*, 10(1):458–482, 2009.
- [4] Alfonso Bueno-Orovio, Elizabeth M Cherry, and Flavio H Fenton. Minimal model for human ventricular action potentials in tissue. *Journal of Theoretical Biology*, 253(3):544–560, 2008.
- [5] Lara A. Charawi. *Isogeometric overlapping additive Schwarz preconditioners in computational electrocardiology*. PhD thesis, Università degli Studi di Milano, 2012.
- [6] Lara A. Charawi. Isogeometric overlapping additive schwarz solvers for the bidomain system. In *Domain Decomposition Methods in Science and Engineering XXII*, pages 127–135. Springer, 2016.
- [7] Piero Colli Franzone, Luca F. Pavarino, and Simone Scacchi. *Mathematical Cardiac Electrophysiology*, volume 13. Springer Switzerland, 2014.
- [8] Annabelle Collin, Jean-Frédéric Gerbeau, Méleze Hocini, Michel Haïssaguerre, and Dominique Chapelle. Surface-based electrophysiology modeling and assessment of physiological simulations in atria. In *International Conference on Functional Imaging and Modeling of the Heart*, pages 352–359. Springer, 2013.
- [9] J. Austin Cottrell, Thomas J.R. Hughes, and Yuri Bazilevs. *Isogeometric Analysis: Toward Integration of CAD and FEA*. John Wiley & Sons, 2009.
- [10] Marc Courtemanche, Rafael J. Ramirez, and Stanley Nattel. Ionic mechanisms underlying human atrial action potential properties: insights from a mathematical model. *American Journal of Physiology - Heart and Circulatory Physiology*, 275(1):H301–H321, 1998.
- [11] Carl De Boor. On calculating with b-splines. *Journal of Approximation theory*, 6(1):50–62, 1972.
- [12] C. De Falco, A. Reali, and R. Vázquez. Geopdes: A research tool for isogeometric analysis of pdes. *Adv. Eng. Softw.*, 42(12):1020–1034, 2011.
- [13] Luca Dedè, Christoph Jäggli, and Alfio Quarteroni. Isogeometric numerical dispersion analysis for two-dimensional elastic wave propagation. *Computer Methods in Applied Mechanics and Engineering*, 284:320–348, 2015.
- [14] Samineh R. Esfahani. Two-dimensional computer model of human atrial ablation. Master’s thesis, 2011.
- [15] Luca G. Giorda. Modeling and numerical simulation of action potential patterns in human atrial tissues. From HAL archives-ouvertes: hal-00132706v2, 2008.

- [16] Alan L. Hodgkin and Andrew F. Huxley. A quantitative description of membrane current and its application to conduction and excitation in nerve. *Journal of Physiology*, pages 500–544, 1952.
- [17] Vincent Jacquemet. *A Biophysical Model of Atrial Fibrillation and Electrograms: Formulation, Validation and Applications*. PhD thesis, EPFL, 2004.
- [18] Richard Klabunde. *Cardiovascular Physiology Concepts*. Lippincott Williams & Wilkins, 2011.
- [19] David E. Krummen, Vijay Swarup, and Sanjiv M. Narayan. The role of rotors in atrial fibrillation. *Journal of Thoracic Disease*, 7(2):142, 2015.
- [20] Ching-Hsing Luo and Yoram Rudy. A model of the ventricular cardiac action potential. Depolarization, repolarization, and their interaction. *Circulation Research*, 68(6):1501–1526, 1991.
- [21] Ching-Hsing Luo and Yoram Rudy. A dynamic model of the cardiac ventricular action potential. I. Simulations of ionic currents and concentration changes. *Circulation Research*, 74(6):1071–1096, 1994.
- [22] Numerical Mathematics. *Quarteroni, Alfio and Sacco, Riccardo and Saleri, Fausto*, volume 37. Springer Science & Business Media, 2010.
- [23] Colleen C. Mitchell and David G. Schaeffer. A two-current model for the dynamics of cardiac membrane. *Bulletin of Mathematical Biology*, 65(5):767–793, 2003.
- [24] Alessandro Patelli. Isogeometric analysis of electrophysiological models on surfaces. Master’s thesis, EPFL, 2014.
- [25] Alessandro S. Patelli, Luca Dedè, Toni Lassila, Andrea Bartezzaghi, and Alfio Quarteroni. Isogeometric approximation of cardiac electrophysiology models on surfaces: an accuracy study with application to the human left atrium. *Computer Methods in Applied Mechanics and Engineering*, 2016:248–273, 2016.
- [26] Les Piegl and Wayne Tiller. *The NURBS Book*. Springer Science & Business Media, 2012.
- [27] Alfio Quarteroni. *Numerical Models for Differential Problems*, volume 2. Springer-Verlag, 2014.
- [28] Alfio Quarteroni, Toni Lassila, Simone Rossi, and Ricardo Ruiz-Baier. Integrated heart–coupling multiscale and multiphysics models for the simulation of the cardiac function. *Computer Methods in Applied Mechanics and Engineering*, 2016.
- [29] Simone Rossi. Anisotropic modeling of cardiac mechanical activation. 2014.
- [30] Shun-Ichiro Sakamoto, Takashi Nitta, Yosuke Ishii, Yasuo Miyagi, Hiroya Ohmori, and Kazuo Shimizu. Interatrial electrical connections: the precise location and preferential conduction. *Journal of Cardiovascular Electrophysiology*, 16(10):1077–1086, 2005.
- [31] Sandro Salsa. *Partial Differential Equations in Action. From Modelling to Theory*. Springer, 2009.
- [32] Elisa Schenone, Annabelle Collin, and Jean-Frédéric Gerbeau. Numerical simulation of electrocardiograms for full cardiac cycles in healthy and pathological conditions. *International Journal for Numerical Methods in Biomedical Engineering*, 2015.
- [33] Radostin D. Simitev and Vadim N. Biktashev. Conditions for propagation and block of excitation in an asymptotic model of atrial tissue. *Biophysical Journal*, 90(7):2258–2269, 2006.
- [34] Joakim Sundnes, Glenn T. Lines, Xing Cai, Børn F. Nielsen, Kente-Andre Mardal, and Aslak Tveito. *Computing the Electrical Activity in the Heart*, volume 1. Springer, 2007.

- [35] Leslie Tung. *A Bi-domain Model for Describing Ischemic Myocardial D-C Potentials*. PhD thesis, Massachusetts Institute of Technology, 1978.
- [36] Mathias Wilhelms. *Multiscale Modeling of Cardiac Electrophysiology: Adaptation to Atrial and Ventricular Rhythm Disorders and Pharmacological Treatment*, volume 20. KIT Scientific Publishing, 2013.